Sites NGHP-01-15

By T. Collett, M. Riedel, J. Cochran, R. Boswell, J. Presley, P. Kumar, A. Sathe,
A. Sethi, M. Lall, and the National Gas Hydrate Program Expedition 01 Scientists

Scientific Investigations Report 2012–5054

U.S. Department of the Interior
U.S. Geological Survey

Contents

Background and Objectives....753
Operations....753
  Hole NGHP-01-15A....753
Lithostratigraphy....757
  Lithostratigraphic Units....759
    Lithostratigraphic Unit I....759
  Gas-Hydrate Occurrence....769
Inorganic Geochemistry....769
  Interstitial Water Chloride—Gas-Hydrate Distribution....769
  Sulfate Concentrations: Characterization of the SMI....778
  Alkalinity and Bromide....779
Organic Geochemistry....779
Microbiology....783
  Hole NGHP-01-15A....783
Physical Properties....783
  Infrared Imaging....786
    Environmental Conditions....786
    Infrared Images....786
    Core-End Temperature Readings....790
  Index Properties....790
  Strength....790
  Electrical Resistivity....795
  P-Wave Velocity....814
  Magnetic Susceptibility....814
  Thermal Conductivity....814
  Downhole Temperature Measurements....814
Pressure Coring....814
    Pressure Core Operations and Measurements....815
    Gas-Hydrate Concentration, Nature, and Distribution from Pressure Coring....827
Downhole Logging....827
  Operations....827
  Logging Data Quality....829
  Logging Units....829
  Gas-Hydrate and Free Gas Occurrence....829
References Cited....833

Figures

1. Location of Site NGHP-01-15 (Prospectus Site GDGH11) in the Krishna-Godavari Basin 754
2. Seismic line AD-94-45 crossing drill Sites NGHP-01-15 (Prospectus Site GDGH11) and Prospectus Site GDGH13 755
3. Close up of seismic line AD-94-45 in the vicinity of Site NGHP-01-15 (Prospectus Site GDGH11) 756
4. Map showing the hole occupied at Site NGHP-01-15 (GDGH11) 757
5. Lithostratigraphic summary of Hole NGHP-01-15A 758
6. Silt and sand beds and laminae recovered throughout Lithostratigraphic Unit I 762
7. Terrestrial organic matter recovered at Hole NGHP-01-15A in Section NGHP-01-11Y-1. 768
8. Authigenic carbonate nodules (>1 cm), micronodules (<1 cm), and bands. A, Section NGHP-01-15A-12H-1, 85–108 cm, micronodules; B, Section NGHP-01-15A-14X-2, 3-24 cm, nodules; C, Section NGHP-01-15A-16Y-1, 19–39 cm, bands 772
9. Iron monosulfides. A, Section NGHP-01-15A-02H-2, 60–88 cm. B, Section NGHP-01-15A-19X-4, 59–80 cm 773
10. Interstitial water composition depth profiles of A, chloride determined via titration (shore-based at Scripps Institution of Oceanography; error is ±0.2 percent) containing sample NGHP-01-15A-09X-3, 40–70 cm; B, chloride determined via titration without NGHP-01-15A-09X-3, 40–70 cm; C, concentration depth profile of Cl^- determined via both titration and ion chromatography; D, sulfate in the upper 37 m of Site NGHP-01-15A showing the present day SMI, the inferred paleo-seafloor, and the inferred depth of the future SMI; F, alkalinity; G, bromide 775
11. A, Infrared image of the gas hydrate bearing sand surrounded by clay before sample NGHP-01-15A-09X-3, 40–70 cm was cut in half in the chemistry laboratory. B, Visible spectrum photograph of sample NGHP-01-15A-09X-3, 40–70 cm after it was cut in half showing both the sand and clay layers 777
12. Plot of headspace methane gas concentration (mM) with depth for Hole NGHP-01-15A 782
13. Plot of headspace carbon dioxide gas concentration (mM) with depth for Hole NGHP-01-15A 784
14. Plot of methane to carbon dioxide gas ratio with depth for headspace, free/void gas, and PCS gas for Hole NGHP-01-15A 785
15. Plot of free/void gas and PCS methane to ethane gas ratio with depth for Hole NGHP-01-15A 787
16. Catwalk temperature and humidity measurements as a function of time during drilling operations at Site NGHP-01-15 789
17. Infrared imaging and the derived downhole temperature profile for Hole NGHP-01-15A 792
18. Selected downhole temperature from infrared imaging compared to same-depth center probe temperature measurements for Hole NGHP-01-15A 793
19. Core-end infrared image of Section NGHP-01-15A-09X-2, with the corresponding reference temperature scale 794

20. Core-end temperature measurements for Hole NGHP-01-15A 795
21. Profiles of core recovery, index, and strength properties for Hole NGHP-01-15A 796
22. Profiles of infrared images, core recovery, electrical resistivity, acoustic *P*-wave velocity, magnetic susceptibility, and thermal conductivity for Hole NGHP-01-15A...797
23. Shear strengths normalized to the effective vertical stress versus subbottom depth for Hole NGHP-01-15A 802
24. Peak and remolded vane shear strengths and sensitivity for Hole NGHP-01-15A............802
25. Apparent formation factor versus subbottom depth for Hole NGHP-01-15A 814
26. Geothermal gradient and estimated depth to the BSR from in situ temperature measurements for Hole NGHP-01-15A..816
27. Temperature and pressure versus elapsed time for each pressure corer deployment as recorded by the corer's internal data logger..817
28. Temperature versus pressure for each successful pressure corer deployment, showing trajectories relative to gas hydrate stability at 30 ppt and 35 ppt salinity...........818
29. Data collected at near in situ pressure and 7 °C for Cores NGHP-01-15A-11Y and -16Y, including X-ray images, gamma density, and P-wave velocity 819
30. Summary of data taken on Cores NGHP-01-15A-11Y and -16Y before, during, and after depressurization, including gamma density profiles collected before and after depressurization, X-ray images collected before and after depressurization, and line scan images collected after depressurization.....................821
31. Summary of data taken on Cores NGHP-01-15A-11Y and -16Y at pressures higher than *in situ* pressure, including P-wave velocity profiles collected before and after pressurization and X-ray images collected before and after pressurization 823
32. Pressure versus volume for successful pressure cores at Site NGHP-01-15, also showing placement of intermediate X-ray or gamma density scans and gas samples...825
33. Pressure versus time for the depressurization of Core NGHP-01-15A-16Y....................826
34. Methane phase diagram for Site NGHP-01-15, with total methane concentration measured from the three successful pressure cores at Site NGHP-01-15........................828
35. Summary of the wireline logs recorded in Hole NGHP-01-15A 830
36. Sonic waveform amplitude and coherence data, and velocity logs measured by the DSI in Hole NGHP-01-15A...831
37. Water saturations from Archie's equation and wireline porosity and resistivity logs in Hole NGHP-01-15A...832

Tables

1. Smear slide data for Hole NGHP-01-15A 760
2. Sand/silt laminae and beds and silty clay occurrences at Hole NGHP-01-15A.....................763
3. Coarse fraction (>63 µm) sieve data for Hole NGHP-01-15A...770
4. Interstitial-water data for Hole NGHP-01-15A..774
5. Headspace gas composition for Site NGHP-01-15 780
6. Void gas composition for Site NGHP-01-15..786

7. Pressure Core Sampler gas composition for Site NGHP-01-15 787
8. List of microbiological samples taken for Site NGHP-01-15 788
9. List of infrared image files collected from Hole NGHP-01-15A 790
10. List of infrared image files collected on section ends from Hole NGHP-01-15A 791
11. List of temperature probe data collected at bottom of cores from Hole NGHP-01-15A 794
12. Moisture and density (MAD) physical properties for Hole NGHP-01-15A 798
13. Vane shear strength results for Hole NGHP-01-15A 800
14. Pocket Penetrometer strength results for Hole NGHP-01-15A 800
15. Wenner array electrical resistivity and formation factor results for Hole NGHP-01-15A 803
16. Contact *P*-wave velocity results determined on split cores sections from Hole NGHP-01-15A 815
17. Thermal conductivity results for Hole NGHP-01-15A 815
18. *In situ* temperature estimates for Site NGHP-01-15 816
19. Summary of pressure-coring operations at Site NGHP-01-15 816
20. Methane hydrate volume and concentration in pore space for successful pressure cores at Site NGHP-01-15 826

Site NGHP-01-15

By T. Collett, M. Riedel, J. Cochran, R. Boswell, J. Presley, P. Kumar, A. Sathe, A. Sethi, M. Lall, and the National Gas Hydrate Program Expedition 01 Scientists

Background and Objectives

Site NGHP-01-15 (Prospectus Site GDGH11) is located at 16° 05.6983'N, 082° 09.7467'E in the Krishna-Godavari (KG) Basin (fig. 1). The water depth is ~926 m. Site NGHP-01-15 is the easternmost site in the KG Basin to be drilled during this expedition.

The objectives of the work carried out at this site follow the general objectives of NGHP Expedition 01:

- Study the occurrence of gas hydrate and establish the background geochemical, geological, geophysical, and microbiological baselines for gas-hydrate proxy studies;
- Define the relationship between the sedimentology and structure of the sediments and the occurrence and concentration of gas hydrate;
- Calibrate remote sensing data such as seismic data by acquiring LWD/MWD and wire-line log data as well as VSP data for time-depth modeling.

The provided seismic data are limited to one seismic line (AD-94-45) and are shown in figures 2 and 3. A BSR is relatively well established along the entire seismic line particularly between shot points 60 and 90 around Site NGHP-01-15. The position of the BSR at the proposed drill site is at 0.16 s TWT, which corresponds to ~126 mbsf using a seismic velocity of 1,580 m/s. The depth of the BSR gradually increases along the seismic line towards the SE as water depth increases and reaches ~201 mbsf at shot point 213 near proposed Site GDGH13 (which was not occupied during this expedition).

Similar to Site NGHP-01-14 (Prospectus Site GDGH14-A), the seismic line shows a typical sequence of ridges and basins (fig. 2). Site NGHP-01-15 is located at the eastern edge of such a basin. The underlying fault (that reaches the seafloor ~500 m to the east) may be intersected at this site at a depth of ~160 mbsf (fig. 3), but the fault trace is uncertain from the seismic data and may even be as deep as 275 mbsf.

This site does not show the steeply-dipping, high-reflectivity layers below the BSR that characterize other sites, such reflectors typically indicate the presence of free gas. However, the BSR reflection is the highest amplitude at this location compared to the rest of the seismic line.

Drilling and coring operations were restricted to a depth above 200 mbsf at this site. This depth is ~80 m below the BSR, depth allowing enough space to accommodate the ~40 m long wire-line logging tools and to image well below the BSR.

Operations

This operations summary covers the Leg 3B transit from Site NGHP-01-14 (GDGH14-A) to Site NGHP-01-15 (GDGH11) and drilling/coring operations for Hole NGHP-01-15A (fig. 4). Schedule details and statistics for this site can be found as Appendixes:

- Appendix 1: NGHP Expedition 01 Operations Schedules
- Appendix 2: NGHP Expedition 01 Operations Statistics

Included in the “Methods” chapter and the glossary is a list of standard or commonly used operations terms and acronyms.

Hole NGHP-01-15A

Hole NGHP-01-15A was first occupied on Leg 3B of NGHP Expedition 01. This hole was drilled at alternate Site NGHP-01-15 (GDGH11). The 4.5 NMI move from Site NGHP-01-14 (GDGH14-A) was made in DP mode however, the hydrophones had been retracted and the drill string recovered prior to the move. The trip was completed in 1.25 hr at an average speed of 3.6 knots. Upon arrival, a positioning beacon was deployed at the prospectus coordinates at 2200 hr on July 12, 2006. The same BHA as was used on the previous Site NGHP-01-14 was deployed from its racked position in the derrick.

Hole NGHP-01-15A was planned as a continuous APC/XCB cored hole to 200.0 mbsf with several pressure cores to be taken within the gas-hydrate stability zone. Temperature measurements were also to be taken using the APCT-3, APCT, and DVTP systems to define a thermal gradient from sea floor to total depth. Like Hole NGHP-01-14A, this hole was designed to combine continuous coring and pressure cores. The hole was to culminate with a complete suite of wire-line logs.

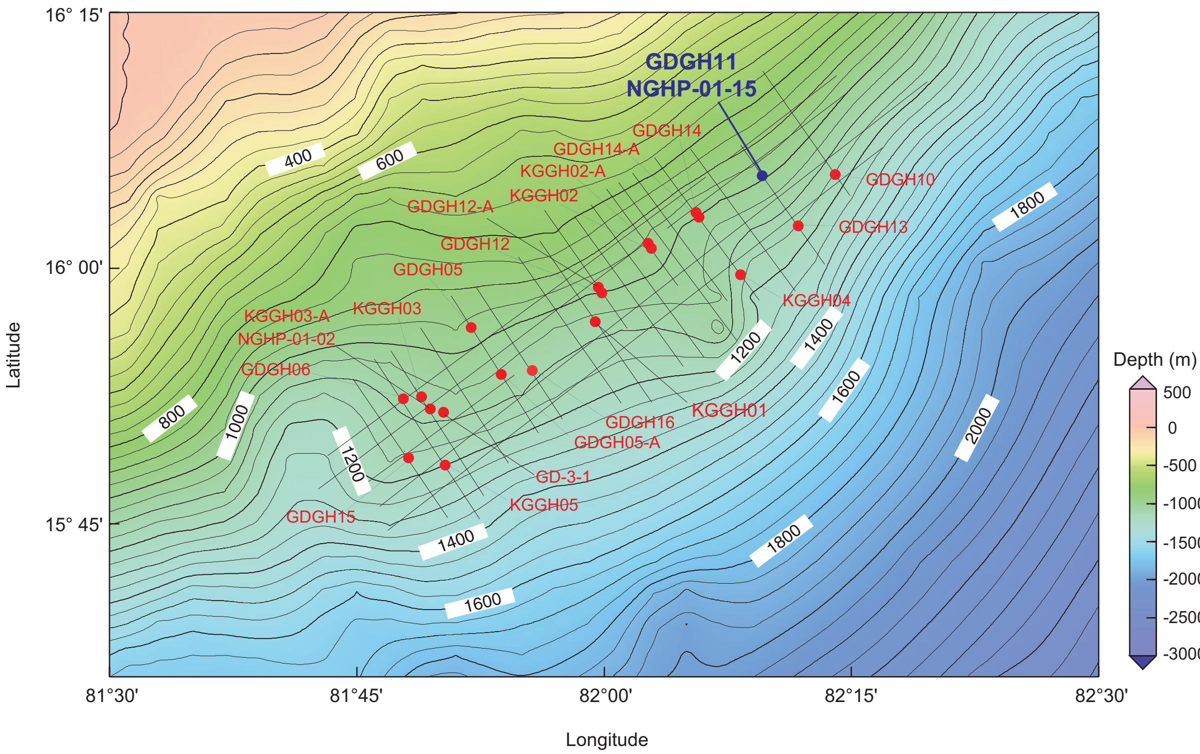

Figure 1. Location of Site NGHP-01-15 (Prospectus Site GDGH11) in the Krishna-Godavari Basin.

The drill string was tripped to bottom. The bit was positioned at a depth of 937.0 mbrf and Hole NGHP-01-15A was spudded at 0125 hr on July 13, 2006, establishing a seafloor depth of 937.9 mbrf. The PDR depth for this site, corrected to the rig floor DES, was 942.4 mbrf. APC Core NGHP-01-15A-01H was on-deck at 0130 hr and APC coring continued through Core NGHP-01-15A-08H to a depth of 76.1 mbsf.

Temperature measurements were taken using the APC-3 shoe on Cores NGHP-01-15A-03H, -05H, and -07H (28.6 mbsf, 47.6 mbsf, and 66.6 mbsf respectively).

A full XCB Core NGHP-01-15A-09X was recovered to 85.7 mbsf setting up the first combination of pressure cores. PCS Core NGHP-01-15A-10P was recovered from 86.7 mbsf. This was followed by an FPC Core NGHP-01-15A-11Y from 87.7 mbsf. Three XCB Cores NGHP-01-15A-12X through NGHP-01-15A-14X to 115.0 mbsf were then recovered setting up the second combination of pressure cores. The second PCS Core NGHP-01-15A-15P, cored to 116.0 mbsf, was followed immediately by a second FPC Core NGHP-01-15A-16Y to a depth of 117.0 mbsf. Two XCB cores (NGHP-01-15A-17X and NGHP-01-15A-18X) were cut to 136.2 mbsf where the first DVTP temperature measurement was successfully taken. Six more XCB Cores NGHP-01-15A-19X through NGHP-01-15A-24X to 193.8 mbsf were recovered and a second DVTP temperature measurement was taken. The last XCB Core NGHP-01-15A-25X deepened the hole to a total depth of 200.0 mbsf.

Both PCS deployments included successful recovery of data with the PCS Methane tool. Penetration rates with the XCB ranged from 8.3 m/h to 32.4 m/h. Core recovery with the XCB system ranged from 48 percent to 102 percent with an average for the hole of 78.2 percent.

Whirlpaks (microbeads) commonly used to assess microbiological contamination were not used at this site. Accelerated core barrel handling protocols were used for all core barrels (APC, XCB, and PCS) deployed in this hole. All APC/XCB core barrels were laid down immediately upon arrival at the rig floor before making another drill pipe connection or deploying the next core barrel.

For all HYACINTH pressure coring systems (FPC and HRC) a 15–20 min wait period was employed at the mudline on the way in the hole and again during retrieval. This was to cool the core barrels down thus aiding in keeping any entrained gas hydrate within the stability field. At the rig floor, all pressure core barrels (PCS, FPC, and HRC) showing signs of proper actuation were placed in the moon pool ice bath prior to processing.

After reaching TD at 200.0 mbsf, 2 hr were spent sweeping the hole and conducting a wiper trip to logging depth and back. The last 16.9 m (last two singles) of the wiper trip required reaming with the top drive. An expendable go-devil was deployed to lock the LFV in the open position and the hole was displaced with 60 barrels of 10.5 ppg weighted mud. The drill string was then tripped setting the EOP at 64.6 mbsf.

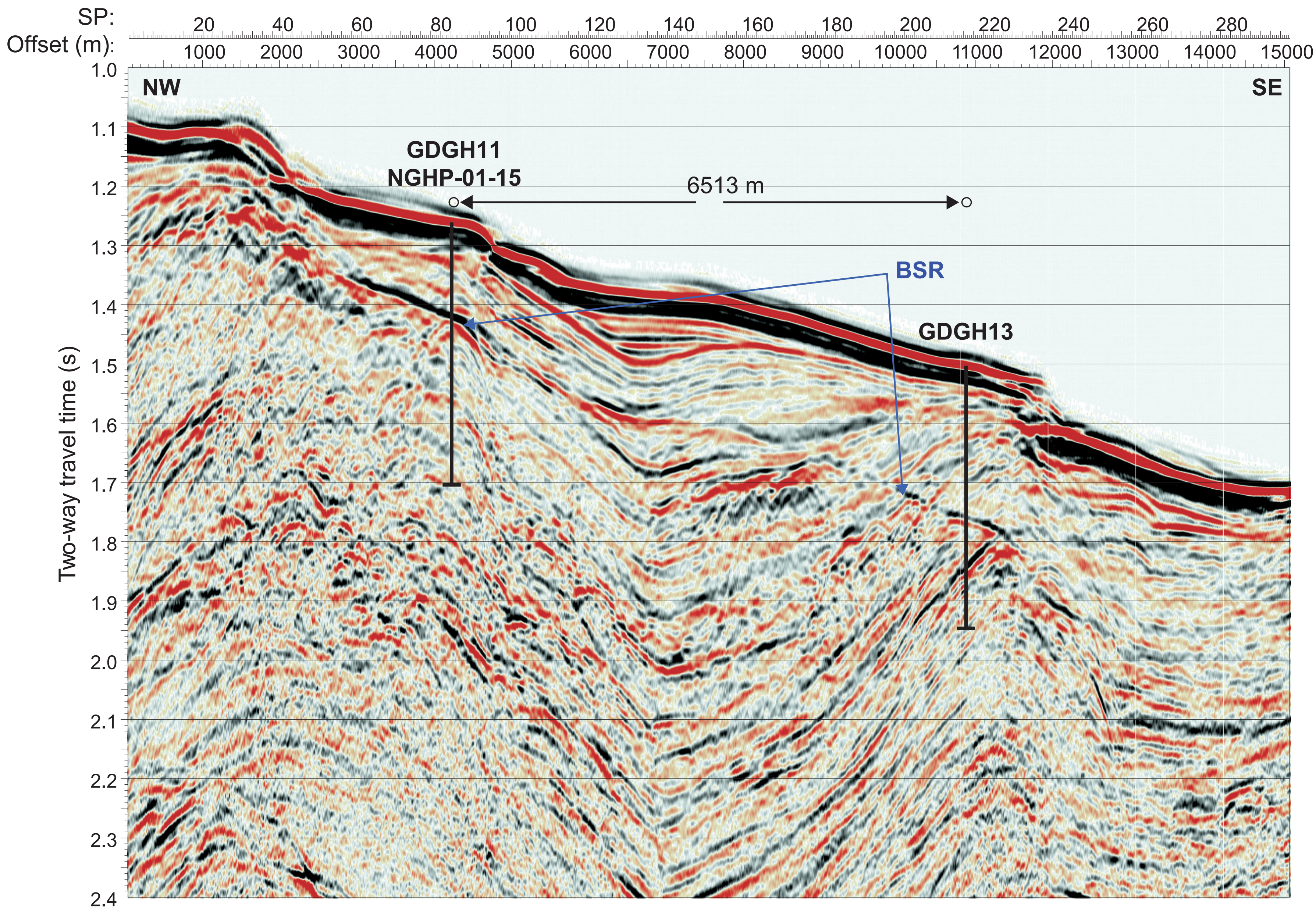

Figure 2. Seismic line AD-94-45 crossing drill Sites NGHP-01-15 (Prospectus Site GDGH11) and Prospectus Site GDGH13.

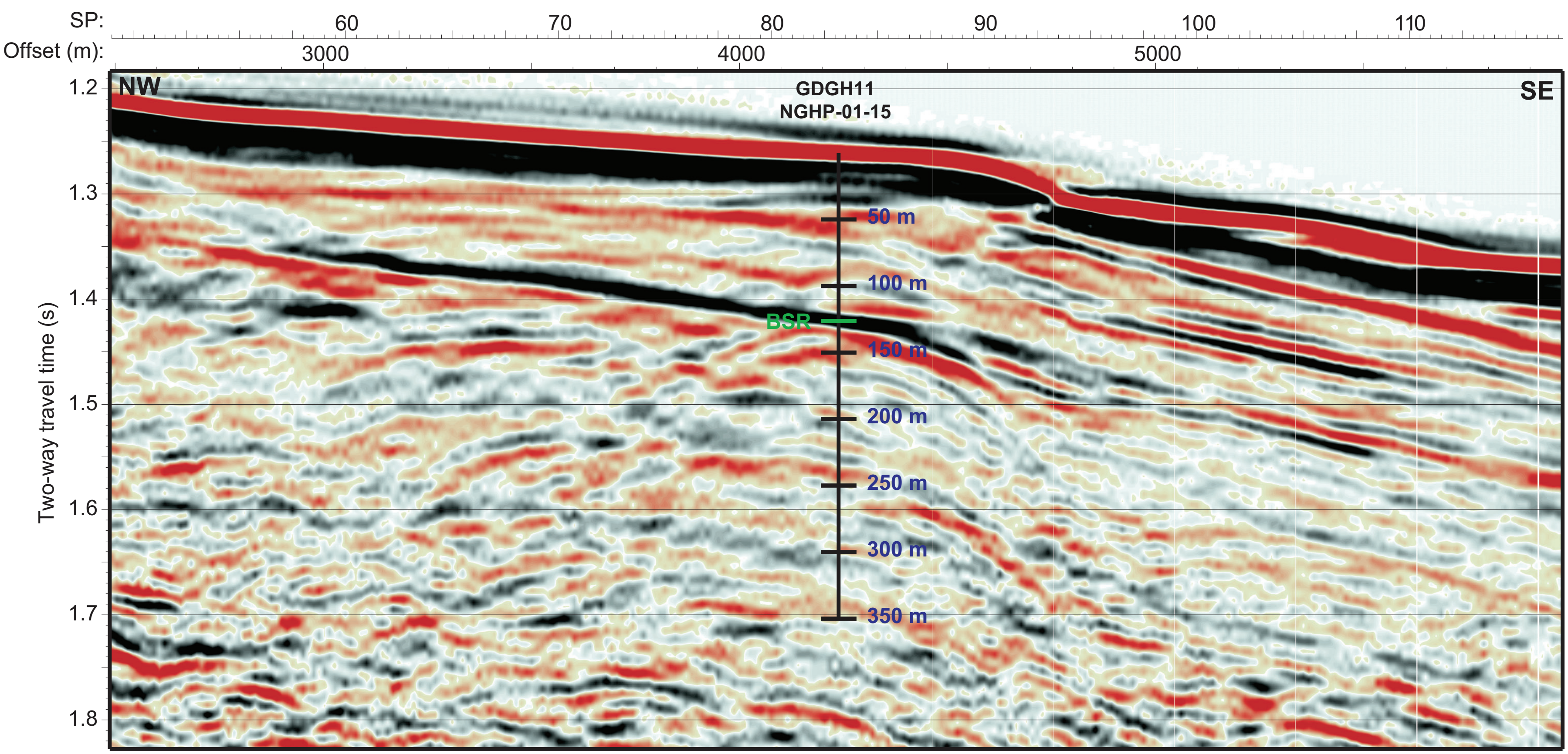

Figure 3. Close up of seismic line AD-94-45 in the vicinity of Site NGHP-01-15 (Prospectus Site GDGH11). Formation and BSR depths were estimated using a constant velocity of 1,580 m/s for the entire sediment column. [BSR, bottom seismic reflector; m/s, meters per second]

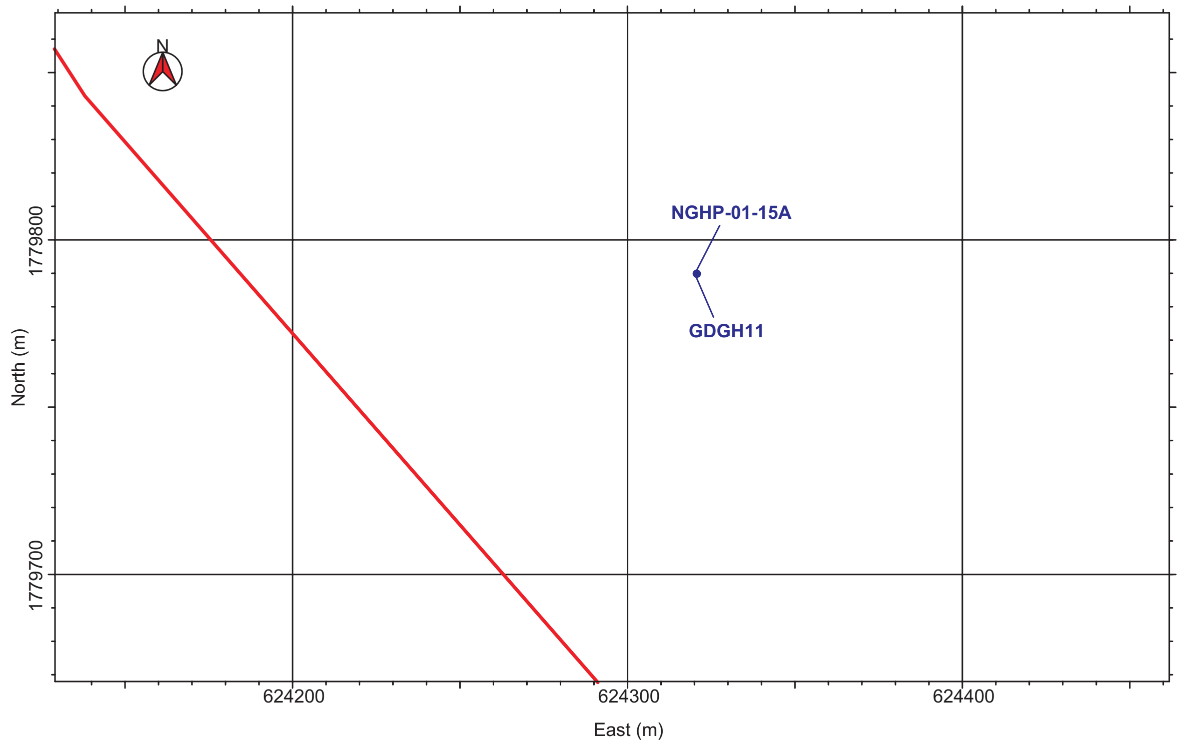

Figure 4. Map showing the hole occupied at Site NGHP-01-15 (GDGH11).

At 1045 hr on July 14, 2006, rig-up for logging began. The first logging run was made with the Triple Combo tool suite. The tools reached the total hole depth of 200.0 mbsf and were out and laid down by 1530 hr. The second tool suite consisted of the FMS-Sonic. This tool string also reached TD and the tools were out and laid down by 2000 hr. It was decided, that VSP logging was not required at this site; also the daylight timing requirement for seismic shooting would have resulted in a significant loss of time. The Schlumberger logging sheaves were rigged down and the drill string was pulled clear of the sea floor at 2115 hr. The positioning beacon was recovered during the pipe trip back to the surface. Thrusters were raised and the rig was secured for transit; officially getting underway for Site NGHP-01-16A at 0006 hr on July 15, 2006.

Lithostratigraphy

Site NGHP-01-15 is located in the KG Basin, along the eastern continental margin of India. At Site NGHP-01-15, one hole (NGHP-01-15A) was drilled, cored, and wire-line logged to a total depth of 200 mbsf (see "Operations"). The lithostratigraphy recovered at Site NGHP-01-15 is similar to the lithostratigraphy previously drilled at other sites throughout the KG Basin. Site NGHP-01-15 is located along strike, to the NE of Sites NGHP-01-05 and NGHP-01-14. All three sites are located in a NE-SW line along the 900-950 m water depth contour. The lithostratigraphy at all three sites (from SW to NE, Holes NGHP-01-05, NGHP-01-14, and NGHP-01-15) is generally similar, (nannofossil-bearing-to-rich clay and clays), as well as the occurrence of sand beds at all three sites. Individual sand beds are generally thicker at Sites NGHP-01-15 and NGHP-01-14 than at Site NGHP-01-05; however, all three sites are similar in the occurrence of sand and silt lamina and beds (of various thickness) throughout the section, as well as authigenic carbonates, iron sulfides, and occasional woody debris. LWD density (Site NGHP-01-05 only), wire-line density (Sites NGHP-01-14 and NGHP-01-15), and magnetic susceptibility data show some correlative stratigraphic packages across the three sites (see fig. 6 in "Site NGHP-01-14").

LWD density (Site NGHP-01-05 only), wire-line density (Sites NGHP-01-14 and NGHP-01-15), and magnetic susceptibility data show some correlative stratigraphic packages across the three sites (see fig. F6 in "Site NGHP-01-14"). However, variations in slope sedimentation dynamics as well as variations in the degree and location of diagenesis (authigenic carbonates, iron monosulifide and pyrite precipitation, the degree of lithification, and gas-hydrate and free gas overprinting of the stratigraphy) from site to site make correlations based on physical property and logging data tenuous.

Similar to all the sites drilled in the KG Basin, Lithostratigraphic Unit I at Site NGHP-01-14 is likely Quaternary to recent in age (see "Lithostratigraphy" in "Site NGHP-01-05"). Because of the lithostratigraphic similarity between Site NGHP-01-14 with Sites NGHP-01-05 and NGHP-01-15 and the relative homogeneity of the stratigraphy throughout the cores at these sites, we also define one Lithostratigraphic Unit (I) at Site NGHP-01-15 (fig. 5 and Site NGHP-01-15 Visual Core Descriptions in the supplemental data files).

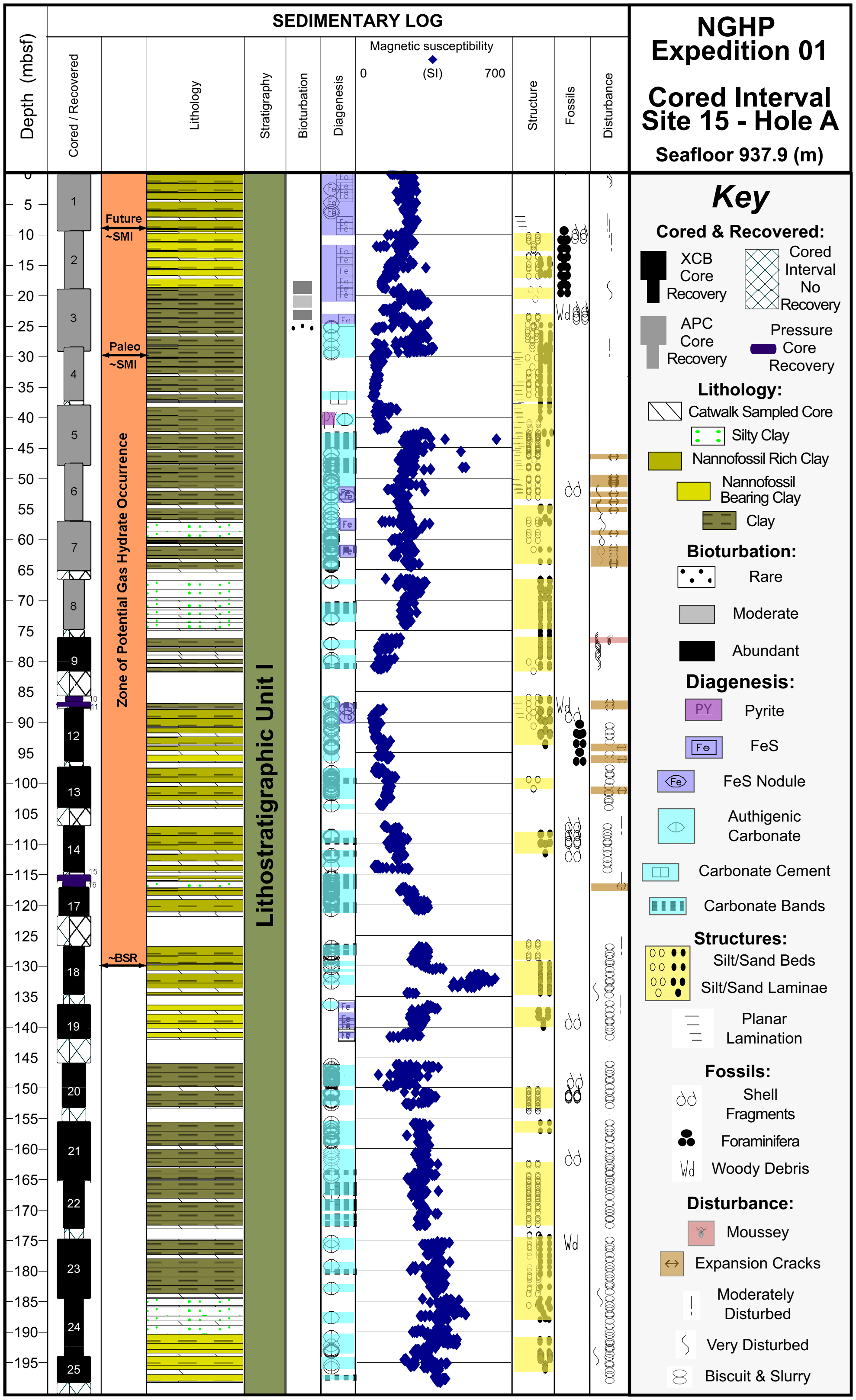

Figure 5. Lithostratigraphic summary of Hole NGHP-01-15A. [BSR, bottom-simulating reflector; RAB, resistivity-at-bit; SMI, sulfate-methane interface (see "Physical Properties" for discussion of paleo and future SMI)] Note: Colored intervals exceed symbol size when there is a range in the occurrence. Center point of each symbol represents depth of occurrence; therefore colored bars may slightly exceed core recovery; see Site NGHP-01-15 Visual Core Descriptions for the expanded scale and detailed core descriptions; see Site NGHP-01-15 Oversized Figure for the enlarged version of this summary.

Lithostratigraphic Units

Lithostratigraphic Unit I

Intervals: Hole NGHP-01-14A, Sections NGHP-01-14A-01H-1 to NGHP-01-14A-23X-CC

Depth: Hole NGHP-01-14A, 0–180 mbsf

Age: Quaternary

Core recovery was good at Hole NGHP-01-15A for the upper ~65 mbsf, through APC and some XCB cores. Between 65 mbsf and ~155 mbsf, the recovery was less, presumably because of gas-hydrate occurrence and(or) coarse grained lithologies (see “Gas-Hydrate Occurrence”). Core recovery was also lower in Cores NGHP-01-15A-18X through NGHP-01-15A-20X and Core NGHP-01-15A-22X, all of which are near or below the BSR (fig. 5).

Lithostratigraphic Unit I is composed of nannofossil-bearing to nannofossil-rich clay, clay, and silty clay that ranges in color from dark brown (2.5Y 3/2) and dark grey (2.5Y 4/1) near the top of the core to very dark gray (2.5Y 3/1) to greenish black (10Y 2.5/1) to black (5Y 2.5/1). Terrestrial organic matter is common (trace to 3 percent) in smear slides taken throughout Unit I (table 1). Thin (0.2–3 cm) silt/sand laminae and beds are abundant in discrete zones throughout the Unit (fig. 5, table T, and Site NGHP-01-15 Visual Core Descriptions); however, beds up to 7 cm thick are also seen (fig. 6 and table 2). These thicker sands are also similar to those observed at Site NGHP-01-14. Lithostratigraphic Unit I at Site NGHP-01-15 is likely Quaternary to recent in age.

Shell fragments and visible foraminifera tests occur sporadically throughout Unit I (fig. 5 and Site NGHP-01-15 Visual Core Descriptions). Rare occurrences of woody debris and terrestrial organic matter are also observed in three locations throughout the Unit (figs. 5 and 7, and Site NGHP-01-15 Visual Core Descriptions). The thickest woody debris occurrence was encountered in a woody debris rich sand bed that was recovered in Pressure Core NGHP-01-15-11Y (fig. 7). This deposit was characterized by a ~2 cm thick sand bed that was graded upward to silt and nearly pure woody material, followed by two additional graded silt to woody debris beds; all three graded beds form one large amalgamated deposit. The sedimentology of these events suggests deposition by three woody debris rich turbidity currents that either coalesced, all closely spaced in time, into one deposit at this site and(or) deposition of three events, widely spaced in time, that eroded into one another, thus forming an amalgamated deposit. Based on the close proximity of the Krishna River to this site, the narrow shelf width, the large amount of terrestrial organic matter in the deposit, and the unique occurrence of these woody debris rich events in all of the recovered KG Basin stratigraphy, we suspect that a massive flood or series of floods was responsible for this amalgamated deposit. In support of a unique period of time, when a series of large flood-induced turbidity currents passed over this site, we also notice a predominance of coarse sand beds closely spaced together in Cores NGHP-01-15-08H and NGHP-01-15-09X, and even in the sand immediately above the woody debris-rich deposit in Core NGHP-01-15-11Y (table 2). Although coarse sands occur occasionally through the Unit, this concentration of coarse beds is notable because they coincide with the largest and broadest IR temperature anomaly observed at this site (see “Physical Properties”) and the beginning of poor core recovery. These observations suggest that these sands offer substantial porosity and permeability for gas-hydrate formation and accumulation, unseen elsewhere in the stratigraphy of Unit I at Site NGHP-01-15.

Authigenic carbonate precipitates as nodules, bands, and cements are common throughout the Unit (figs. 5 and 8, and Site NGHP-01-15 Visual Core Descriptions). Bioturbated zones are most easily seen in lighter colored portions of the cores where highlighted by dark grey to black colored iron sulfide precipitates (fig. 9). The dark grey to black color pervasive throughout most of Unit I likely masks much of this contrast. There is only a narrow zone of bioturbation observed near the top of Unit I (fig. 5 and Site NGHP-01-15 Visual Core Descriptions). Identification of iron sulfides, from visual observation in cores, is consistent with the above and is most prevalent near the upper portion (0–25 mbsf) of Unit I and in smaller occurrences between 40 mbsf and 90 mbsf. In coarse fraction (>63 mm) samples, however, iron sulfides (mostly pyrite) are common (trace to 50 percent) throughout the entire Unit (table 3). Downcore magnetic susceptibility measurements (fig. 5) throughout the Unit show variability patterns similar to those at Sites NGHP-01-05 and NGHP-01-14 (see fig. 6 in “Site NGHP-01-14”); however, at Site NGHP-01-15 there are two large increases in susceptibility (from ~40 mbsf to ~50 mbsf and ~130 mbsf to 140 mbsf). Magnetic iron sulfides (likely gregite and(or) pyrrhotite) have been observed in gas-hydrate bearing sediments offshore western North America (Musgrave and others, 2006) and may be responsible for some of the magnetic susceptibility highs observed here. At Site NGHP-01-03 and Site NGHP-01-16, we observed magnetic iron sulfide nodules that are either gregite or pyrrhotite, confirming their presence throughout much of the stratigraphy in the Krishna-Godavari Basin. Magnetic susceptibility is also high in stratigraphic packages containing abundant sand and silt beds, which often contain magnetite grains (opaque minerals in smear slide; for example, Trehu and others, 2003). Thus, the variations observed in the magnetic susceptibility are likely recording a mixed signal resulting from primary deposition and secondary magnetic iron sulfide precipitation. At Site NGHP-01-15, the two highest susceptibility zones are coincident with abundant sand and silt beds and lamina, and significant pyrite recovered in the coarse fraction (table 3); however, trace magnetic iron sulfides present in these intervals cannot be ruled out as a potentially strong contributor to the overall magnetic susceptibility signal.

Table 1. Smear slide data for Hole NGHP-01-15A.

Sample reference		Texture			Mineral								
Core, section, depth (cm, in section)	Lithology	Sand	Silt	Clay	Quartz	Feldspar	Mica	Heavy minerals	Clay minerals	Volcanic glass	Glauco-nite	Iron sulfides	Authigenic carbonates
NGHP-01-15A													
1H-1,10	D		trace	100					75			trace	
1H-6,80	D		2	98	2		trace		78				5
2H-1,120	D		13	87	5	2	3	trace	78	trace		3	3
2H-4,101	M	99	1	trace	61	12	15	6	trace			2	4
2H-7,10	D		15	85	7	1	3	trace	82			trace	trace
3H-1,123	D		1	99	2				90			3	trace
3H-2,59	M		40	60	2				50				
3H-3,67	M		25	75	1				58				
3H-4,59	M		100		1							99	
4H-1,87	D		2	98	3	trace			92			2	trace
4H-3,47	D		1	99	3				92			3	
4H-4,131	M		100		82	2	2	trace				10	2
5H-2,76	D		1	99	2				92			3	1
5H-5,62	D		1	99	1				94			1	
5H-5,69.5	M	20	80		80	10	3					5	2
6H-2,54	D		3	97	5				89			2	2
6H-5,55	D		3	97	4				90			3	
7H-1,143	D	trace	25	75	13	2	5	3	74	trace			2
7H-3,13	D		2	98	2	trace	trace	trace	89			trace	4
7H-6,27	M		trace	100					99				1
8H-4,55	D	1	30	69	13	4	5	2	68			3	5
8H-4,61	M	98	2	trace	52	13	15	3				6	10
9X-4,15	D		15	85	5	1	2		51		trace	7	30
9X-4,31	M	90		10	75	5	7	2	3				8
11Y-1,36	D	20	5	75	12	2	3	trace	45				35
11Y-1,83	M	75	7	18	56	5	15	trace				4	12
12X-2,70	D	trace	26	74	12	3	5		34			10	8
12X-2,125	M	100		trace	65	11	15	2		trace		4	3
12X-6,70	D	3	32	65	25	2	5	trace	47			2	12
13X-4,60	D		30	70	15	5	7	1	47			2	10
13X-4,71	M	trace	12	88	9	1	2		25				20
14X-1,70	D	2	33	65	21	6	3	2	34	trace		2	17
14X-6,70	D	trace	12	88	6	1	2	trace	44			4	30
16Y-1,65	D		40	60	32	7	18	trace	21			4	15
17X-3,109	M	trace	trace	100	trace		trace	trace	20	trace			45
17X-3,108	D		23	77	13	2	4			30	trace	1	30
18X-2,90	D		trace	100	trace				65				10
18X-5,68	M	80	7	13	30	12	5	trace	10			18	25
18X-5,75	D	10	30	60	12	3	5	trace	34			13	18
19X-4,66	M	35	45	20	40	18	15	trace	10			2	15
19X-2,70	D	trace	23	77	15	3	4	trace	54			trace	15
20X-1,86.5	D		5	95	3	trace			86			3	
20X-4,50	D		10	90	5				93			1	
21X-1,66	D		4	96	6				88				4
21X-5,54	D		2	98	3	trace			93			1	trace
22X-1,74	D		1	99	1				94			2	
22X-5,78	D		1	99	1				91			1	
23X-2,46	M	10	80	10	3								
23X-2,78	D		1	99		trace			93				
23X-4,31	M	80	20		90	1						8	1
23X-5,68	D		1	99	3				93			1	
24X-2,111	M	70	18	12	55	8	15	6	12			1	3
24X-3,51	D	3	27	70	10	2	6		63			3	13
24X-5,130	D		2	98	2	trace	trace		54			trace	35
25X-1,57	M	68	10	22	41	8	14	2	20			7	5
25X-1,140	D	3	25	72	13	4	7	1	62	trace	trace	1	7
25X-2,100	D		7	93	6	trace	1	trace	69			trace	17

Table 1. Smear slide data for Hole NGHP-01-15A.—Continued

Sample reference		Biogenic							
Core, section, depth (cm, in section)	Lithology	Fora-minifera	Nanno-fossils	Carbonate shell fragments	Diatoms	Radio-larians	Sponge spicules	Plant debris	Comments
NGHP-01-15A—Continued									
1H-1,10	D	trace	25					trace	
1H-6,80	D		15						
2H-1,120	D	trace	6					trace	
2H-4,101	M	trace							From silt layer
2H-7,10	D	1	5					1	
3H-1,123	D	1	2					2	
3H-2,59	M	40						1	From silt layer
3H-3,67	M	40	1						From silty clay
3H-4,59	M	trace							Iron sulfide patch
4H-1,87	D	1	trace				trace	2	
4H-3,47	D	1						1	
4H-4,131	M	2							From silt layer
5H-2,76	D	trace	trace					2	
5H-5,62	D	1	2					1	
5H-5,69.5	M						trace	trace	From sand layer
6H-2,54	D							2	
6H-5,55	D	trace	trace					3	
7H-1,143	D							1	
7H-3,13	D		5						
7H-6,27	M								
8H-4,55	D	trace							
8H-4,61	M	1							From sand layer
9X-4,15	D		4						Trace gastropods
9X-4,31	M								From sand layer
11Y-1,36	D							3	Pyritized wood fragments
11Y-1,83	M							8	From sand
12X-2,70	D		28						
12X-2,125	M								From sand layer, hornblende present
12X-6,70	D		7					trace	
13X-4,60	D	1	12						
13X-4,71	M	trace	43						From carbonate sand
14X-1,70	D	trace	15						
14X-6,70	D	trace	13						
16Y-1,65	D	trace	3						
17X-3,109	M		35						From carbonate layer
17X-3,108	D		20						
18X-2,90	D		25						
18X-5,68	M	trace							From sand layer
18X-5,75	D		15						
19X-4,66	M	trace							From silty clay
19X-2,70	D	trace	9						
20X-1,86.5	D	4	3					1	
20X-4,50	D	1	trace					trace	
21X-1,66	D	1	trace					1	
21X-5,54	D	1	2					trace	
22X-1,74	D	1						2	
22X-5,78	D	2	2					3	
23X-2,46	M	1						96	From organic rich layer
23X-2,78	D	2	3				trace	2	
23X-4,31	M	trace							From sand
23X-5,68	D	trace						3	
24X-2,111	M								From loomy sand
24X-3,51	D		3					trace	Trace dolomite
24X-5,130	D		9						
25X-1,57	M		3						From sand
25X-1,140	D		5					trace	
25X-2,100	D		7						

Note: M = minor lithology, D = dominant lithology.

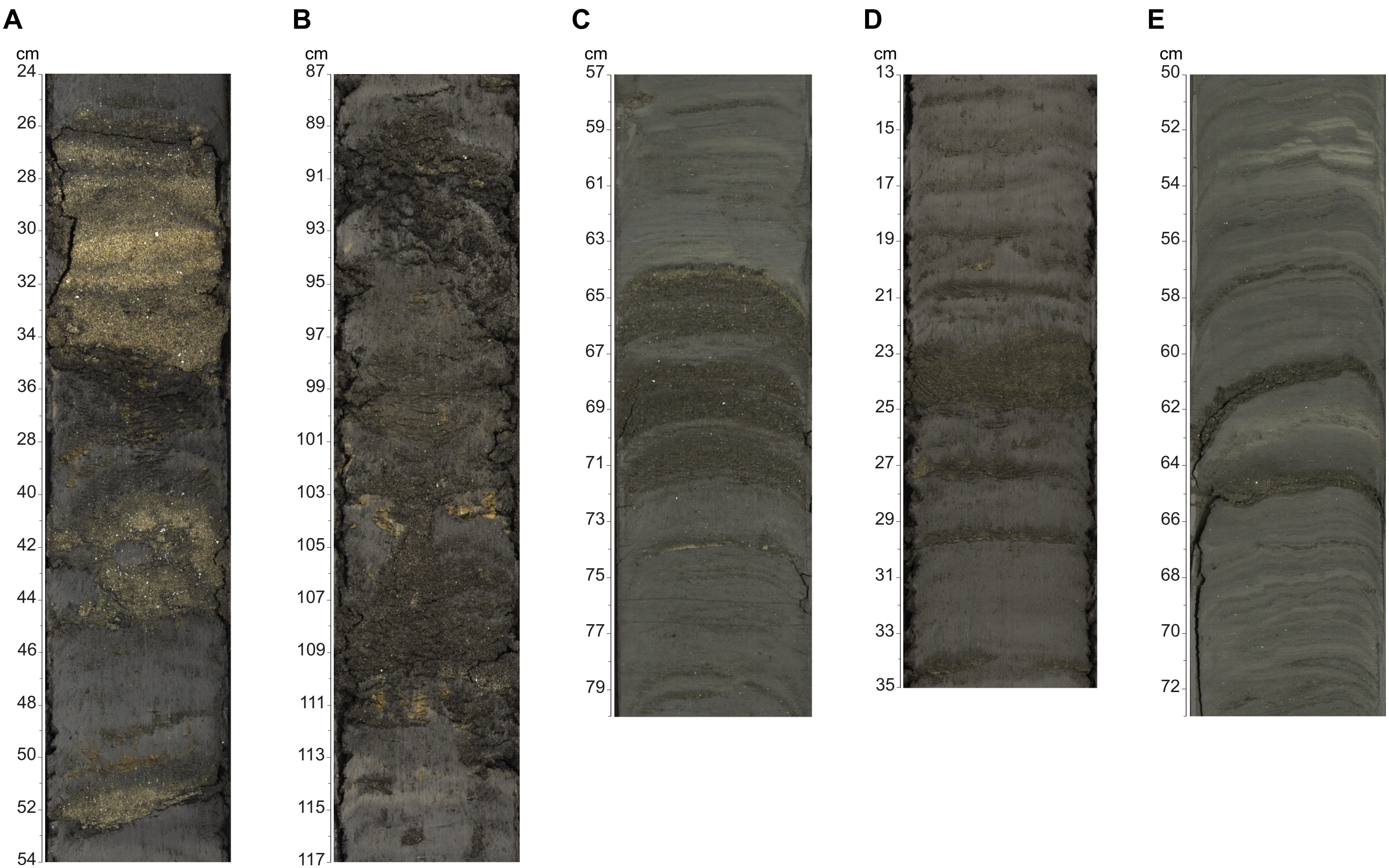

Figure 6. Silt and sand beds and laminae recovered throughout Lithostratigraphic Unit I. The thickest beds within Hole NGHP-01-15A were observed: A, Section NGHP-01-15A-09X-4, 24–54 cm, B, Section NGHP-01-15A-09X-1, 87–117 cm, and C, Section NGHP-01-15A-04H-5, 57–80 cm. Thin silt laminae and beds typical of Lithostratigraphic Unit I from D, Section NGHP-01-15A-18X-5, 13–35 cm and E, Section NGHP-01-15A-04H-2, 50–73 cm are shown. Also notice the thin authigenic carbonate bands and small nodules throughout these examples.

Table 2. Sand/silt laminae and beds and silty clay occurrences at Hole NGHP-01-15A.

Core, section	Position start	Position end	Depth top (mbsf)	Depth base (mbsf)	Type
			NGHP-01-15A		
2H-5	15	20	15.75	15.8	Silt laminae
2H-5	20	23	15.8	15.83	Sand bed
2H-2	47	48	11.57	11.58	Silt laminae
2H-4	50	51	14.6	14.61	Silt laminae
2H-4	72	73	14.82	14.83	Silt laminae
2H-5	24	24	15.84	15.84	Sand bed
2H-5	32	32	15.92	15.92	Silt bed
2H-5	36	36	15.96	15.96	Silt bed
2H-2	17	17	11.27	11.27	Silt laminae
2H-2	108	108	12.18	12.18	Silt laminae
2H-4	120	120	15.3	15.3	Silt laminae
2H-4	139	139	15.49	15.49	Silt laminae
3H-1	50	107	19.6	20.17	Silty clay
3H-2	31	70	20.91	21.3	Silty clay
3H-5	69	100	25.79	26.1	Multiple silt laminae
3H-3	48	76	22.58	22.86	Silty clay
3H-7	37	60	28.47	28.7	Silty clay
3H-6	18	40	26.78	27	Multiple silt laminae
3H-3	0	12	22.1	22.22	Silty clay
3H-3	24	36	22.34	22.46	Silty clay
3H-6	128	138	27.88	27.98	Multiple silt laminae
3H-2	0	10	20.6	20.7	Silty clay
3H-6	115	121	27.75	27.81	Multiple silt laminae
3H-7	20	26	28.3	28.36	Multiple silt laminae
3H-7	0	6	28.1	28.16	Silty clay
3H-6	63	66	27.23	27.26	Multiple silt laminae
3H-7	13	16	28.23	28.26	Multiple silt laminae
3H-2	100	102	21.6	21.62	Silty clay
3H-4	34	36	23.94	23.96	Silty clay
3H-5	85	85	25.95	25.95	Sand bed
3H-5	88	88	25.98	25.98	Sand bed
3H-6	67	67	27.27	27.27	Sand bed
3H-6	70	70	27.3	27.3	Sand bed
3H-6	121	121	27.81	27.81	Sand bed
3H-7	34	34	28.44	28.44	Sand bed
3H-1	110	110	20.2	20.2	Silt laminae
3H-4	88	88	24.48	24.48	Silt laminae
3H-4	112	112	24.72	24.72	Silt laminae
3H-4	113	113	24.73	24.73	Silt laminae
3H-4	120	120	24.8	24.8	Silt laminae
3H-6	108	108	27.68	27.68	Silt laminae
3H-7	33	33	28.43	28.43	Silt laminae
4H-1	17	140	28.77	30	Silty clay
4H-4	109	128	34.19	34.38	Silty sand bed
4H-4	30	46	33.4	33.56	Silty clay
4H-6	83	90	36.93	37	Multiple sand beds
4H-2	120	127	31.3	31.37	Multiple silt laminae
4H-5	64	71	35.24	35.31	Sand bed
4H-6	75	79	36.85	36.89	Multiple sand beds
4H-1	77	81	29.37	29.41	Multiple sand laminae
4H-1	130	134	29.9	29.94	Multiple sand laminae
4H-1	107	110	29.67	29.7	Multiple sand laminae
4H-3	0	3	31.6	31.63	Sand bed
4H-4	129.5	132	34.395	34.42	Sand bed
4H-1	134	136	29.94	29.96	Multiple sand beds
4H-2	117	119	31.27	31.29	Sand bed
4H-6	20	22	36.3	36.32	Sand bed

Table 2. Sand/silt laminae and beds and silty clay occurrences at Hole NGHP-01-15A.—Continued

Core, section	Position start	Position end	Depth top (mbsf)	Depth base (mbsf)	Type
			NGHP-01-15A—Continued		
4H-6	28	30	36.38	36.4	Sand bed
4H-4	138	140	34.48	34.5	Silt bed
4H-2	64	65	30.74	30.75	Sand bed
4H-2	86	87	30.96	30.97	Sand bed
4H-2	109	110	31.19	31.2	Sand bed
4H-2	112	113	31.22	31.23	Sand bed
4H-5	12	13	34.72	34.73	Sand bed
4H-6	24	25	36.34	36.35	Sand bed
4H-1	49	49	29.09	29.09	Sand bed
4H-1	63	63	29.23	29.23	Sand bed
4H-1	67	67	29.27	29.27	Sand bed
4H-1	120	120	29.8	29.8	Sand bed
4H-1	130	130	29.9	29.9	Sand bed
4H-2	4	4	30.14	30.14	Sand bed
4H-2	6	6	30.16	30.16	Sand bed
4H-2	9	9	30.19	30.19	Sand bed
4H-2	11	11	30.21	30.21	Sand bed
4H-2	13	13	30.23	30.23	Sand bed
4H-2	18	18	30.28	30.28	Sand bed
4H-2	55	55	30.65	30.65	Sand bed
4H-2	57	57	30.67	30.67	Sand bed
4H-2	61	61	30.71	30.71	Sand bed
4H-2	81	81	30.91	30.91	Sand bed
4H-2	106	106	31.16	31.16	Sand bed
4H-2	132	132	31.42	31.42	Sand bed
4H-5	74	74	35.34	35.34	Sand bed
4H-5	94	94	35.54	35.54	Sand bed
4H-6	17	17	36.27	36.27	Sand bed
4H-6	36	36	36.46	36.46	Sand bed
4H-6	38.5	38.5	36.485	36.485	Sand bed
4H-6	45.5	45.5	36.555	36.555	Sand bed
4H-6	70.5	70.5	36.805	36.805	Sand bed
4H-6	72	72	36.82	36.82	Sand bed
4H-4	60	60	33.7	33.7	Silt bed
4H-4	70	70	33.8	33.8	Silt bed
4H-5	82	82	35.42	35.42	Silt bed
4H-5	84	84	35.44	35.44	Silt bed
4H-5	87	87	35.47	35.47	Silt bed
5H-6	40	150	46	47.1	Silty clay
5H-3	73	79	41.83	41.89	Silt bed
5H-4	82	87	43.42	43.47	Sand filled burrows
5H-1	116	118	39.26	39.28	Sand bed
5H-4	6	8	42.66	42.68	Silt bed
5H-7	0	2	47.1	47.12	Silt bed
5H-7	29	31	47.39	47.41	Silt bed
5H-1	2	3	38.12	38.13	Sand bed
5H-1	97	98	39.07	39.08	Sand bed
5H-3	103	104	42.13	42.14	Silt bed
5H-4	96	97	43.56	43.57	Silt bed
5H-5	31	32	44.41	44.42	Silt bed
5H-4	2.5	2.5	42.625	42.625	Silt bed
5H-4	102	102	43.62	43.62	Silt bed
5H-4	104	104	43.64	43.64	Silt bed
5H-5	3	3	44.13	44.13	Silt bed
5H-5	13	13	44.23	44.23	Silt bed
5H-5	24	24	44.34	44.34	Silt bed
5H-5	26	26	44.36	44.36	Silt bed

Table 2. Sand/silt laminae and beds and silty clay occurrences at Hole NGHP-01-15A.—Continued

Core, section	Position start	Position end	Depth top (mbsf)	Depth base (mbsf)	Type
			NGHP-01-15A—Continued		
5H-5	35	35	44.45	44.45	Silt bed
5H-5	70	70	44.8	44.8	Silt bed
5H-5	72	72	44.82	44.82	Silt bed
5H-5	73	73	44.83	44.83	Silt bed
5H-7	8	8	47.18	47.18	Silt bed
5H-7	22	22	47.32	47.32	Silt bed
5H-7	26.5	26.5	47.365	47.365	Silt bed
5H-1	123	123	39.33	39.33	Silty clay
6H-7	20	33	56	56.13	Multiple silt laminae
6H-6	90	100	55.7	55.8	Multiple sand laminae
6H-3	36	44	50.75	50.83	Multiple silt beds
6H-7	30	34	56.1	56.14	Multiple sand beds
6H-3	60	63	50.99	51.02	Multiple silt beds
6H-7	40	41	56.2	56.21	Sand bed
6H-7	44	45	56.24	56.25	Sand bed
6H-7	49	50	56.29	56.3	Sand bed
6H-3	79	80	51.18	51.19	Silt bed
6H-3	83	84	51.22	51.23	Silt bed
6H-3	86	87	51.25	51.26	Silt bed
6H-3	90	91	51.29	51.3	Silt bed
6H-7	55	55	56.35	56.35	Sand bed
6H-4	31	31	52.2	52.2	Silt bed
7H-2	9	90	58.69	59.5	Silty clay
7H-4	20	28	61.17	61.25	Multiple silt laminae
7H-3	16	23	60.17	60.24	Silty clay
7H-1	82	83	57.92	57.93	Silt bed
7H-1	125	126	58.35	58.36	Silt bed
8H-2	0	136	68.03	69.39	Multiple silt/sand laminae
8H-1	72	143	67.32	68.03	Multiple silt/sand laminae
8H-6	59	63	73.41	73.45	Multiple sand beds
8H-1	100	101	67.6	67.61	Sand bed
8H-1	90	90	67.5	67.5	Sand bed
8H-4	51	51	70.57	70.57	Sand bed
8H-4	61	61	70.67	70.67	Sand bed
8H-4	78	78	70.84	70.84	Sand bed
8H-5	13	13	71.56	71.56	Sand bed
8H-5	66	66	72.09	72.09	Sand bed
8H-6	19	19	73.01	73.01	Sand bed
9X-1	0	130	76.1	77.4	Sandy clay
9X-5	0	63	80.82	81.45	Multiple sand laminae
9X-2	0	57	77.6	78.17	Multiple sand beds
9X-1	89	114	76.99	77.24	Multiple sand beds
9X-1	57	80	76.67	76.9	Multiple sand beds
9X-4	0	10	79.53	79.63	Multiple sand beds
9X-4	25	35	79.78	79.88	Multiple sand beds
9X-1	119	127	77.29	77.37	Multiple sand beds
9X-1	0	5	76.1	76.15	Multiple sand beds
9X-4	40	45	79.93	79.98	Multiple sand beds
9X-4	50	53	80.03	80.06	Multiple sand beds
9X-2	63	63	78.23	78.23	Sand bed
9X-2	70	70	78.3	78.3	Sand bed
11Y-1	67	74	87.37	87.44	Sand bed
11Y-1	80	85	87.5	87.55	Sand bed
11Y-1	40	44	87.1	87.14	Sand bed
11Y-1	20	24	86.9	86.94	Silt bed
12X-6	0	102	95.2	96.22	Silty clay
12X-1	7	29	86.77	86.99	Silty clay

Table 2. Sand/silt laminae and beds and silty clay occurrences at Hole NGHP-01-15A.—Continued

Core, section	Position start	Position end	Depth top (mbsf)	Depth base (mbsf)	Type
			NGHP-01-15A—Continued		
12X-2	97	107	90.17	90.27	Multiple silt laminae
12X-1	22	26	86.92	86.96	Sand bed
12X-1	16	18	86.86	86.88	Sand bed
12X-4	41	41	92.61	92.61	Sand laminae
12X-4	50	50	92.7	92.7	Sand laminae
12X-4	63	63	92.83	92.83	Sand laminae
12X-4	66	66	92.86	92.86	Sand laminae
12X-2	120	120	90.4	90.4	Sand pocket
12X-2	125	125	90.45	90.45	Sand pocket
12X-2	17	17	89.37	89.37	Silt laminae
13X-3	0	3	100.3	100.33	Sand bed
13X-3	7	10	100.37	100.4	Sand bed
14X-3	73	73	110.63	110.63	Sand burrow fill
14X-2	68	68	109.08	109.08	Sand laminae
18X-4	120	137	132.3	132.47	Multiple silt/sand laminae
18X-4	97	107	132.07	132.17	Multiple silt/sand laminae
18X-4	29	33	131.39	131.43	Multiple silt/sand laminae
18X-5	67	70	133.27	133.3	Silt/sand bed
18X-3	85	87	130.45	130.47	Sand bed
18X-5	77	79	133.37	133.39	Silt/sand bed
18X-4	142	144	132.52	132.54	Silt/sand laminae
18X-5	4	5	132.64	132.65	Silt/sand bed
18X-5	23	24	132.83	132.84	Silt/sand bed
18X-5	47	47	133.07	133.07	Silt/sand bed
18X-1	48	48	127.08	127.08	Silt/sand laminae
18X-1	71	71	127.31	127.31	Silt/sand laminae
18X-1	96	96	127.56	127.56	Silt/sand laminae
18X-4	8	8	131.18	131.18	Silt/sand laminae
19X-2	40	40	138.1	138.1	Silt/sand laminae
19X-2	122	122	138.92	138.92	Silt/sand laminae
20X-4	77	77	151.07	151.07	Silt bed
20X-4	91	91	151.21	151.21	Silt bed
20X-4	96	96	151.26	151.26	Silt bed
20X-4	114	114	151.44	151.44	Silt bed
20X-4	120	120	151.5	151.5	Silt bed
20X-4	139	139	151.69	151.69	Silt bed
20X-5	3	3	151.83	151.83	Silt bed
20X-5	35	35	152.15	152.15	Silt bed
20X-5	10	10	151.9	151.9	Silt bed
20X-5	91	91	152.71	152.71	Silt bed
21X-1	46	49	155.86	155.89	Silt bed
21X-6	29	30	163.39	163.4	Silt bed
21X-6	53	53	163.63	163.63	Silt bed
22X-5	48	50	170.58	170.6	Silt bed
22X-2	12	13	166.62	166.63	Silt bed
22X-2	36	37	166.86	166.87	Silt bed
22X-5	12	13	170.22	170.23	Silt bed
22X-5	122	123	171.32	171.33	Silt bed
22X-1	92	92	165.92	165.92	Silt bed
22X-1	107	107	166.07	166.07	Silt bed
22X-1	115	115	166.15	166.15	Silt bed
22X-2	24	24	166.74	166.74	Silt bed

Table 2. Sand/silt laminae and beds and silty clay occurrences at Hole NGHP-01-15A.—Continued

Core, section	Position start	Position end	Depth top (mbsf)	Depth base (mbsf)	Type
			NGHP-01-15A—Continued		
22X-2	27	27	166.77	166.77	Silt bed
22X-2	49	49	166.99	166.99	Silt bed
22X-2	58	58	167.08	167.08	Silt bed
22X-2	95	95	167.45	167.45	Silt bed
22X-5	22	22	170.32	170.32	Silt bed
23X-3	0	48	176.31	176.79	Silty clay
23X-4	30	31	178.11	178.12	Sand bed
23X-5	10	11	179.41	179.42	Sand bed
23X-6	88	89	181.69	181.7	Sand bed
23X-2	23	24	175.04	175.05	Silt bed
23X-4	37	37	178.18	178.18	Sand bed
23X-4	42	42	178.23	178.23	Sand bed
23X-4	50.5	50.5	178.315	178.315	Sand bed
23X-4	130	130	179.11	179.11	Sand bed
23X-7	112	112	183.36	183.36	Sand bed
23X-2	33	33	175.14	175.14	Silt bed
23X-2	40	40	175.21	175.21	Silt bed
23X-2	12	12	174.93	174.93	Silt bed
23X-2	87	87	175.68	175.68	Silt bed
23X-2	105	105	175.86	175.86	Silt bed
23X-2	124	124	176.05	176.05	Silt bed
23X-5	92	92	180.23	180.23	Silt bed
23X-5	112	112	180.43	180.43	Silt bed
23X-5	113	113	180.44	180.44	Silt bed
23X-6	12	12	180.93	180.93	Silt bed
23X-6	79	79	181.6	181.6	Silt bed
23X-6	80	80	181.61	181.61	Silt bed
23X-6	81	81	181.62	181.62	Silt bed
23X-6	84	84	181.65	181.65	Silt bed
23X-6	86	86	181.67	181.67	Silt bed
23X-6	104	104	181.85	181.85	Silt bed
23X-6	107	107	181.88	181.88	Silt bed
24X-1	15	50	184.35	184.7	Silty clay
24X-6	83	90	192.53	192.6	Multiple sand beds
24X-2	107	113	186.77	186.83	Sand bed
24X-2	24	28	185.94	185.98	Multiple silt/sand laminae
24X-6	25	25	191.95	191.95	Sand bed
24X-6	29	29	191.99	191.99	Sand bed
24X-6	42	42	192.12	192.12	Sand bed
24X-6	47	47	192.17	192.17	Sand bed
24X-6	53	53	192.23	192.23	Sand bed
24X-6	58	58	192.28	192.28	Sand bed
24X-6	75	75	192.45	192.45	Sand bed
24X-6	78	78	192.48	192.48	Sand bed
24X-2	100	100	186.7	186.7	Silt/sand laminae
25X-1	106	110	194.86	194.9	Multiple silt/sand laminae
25X-1	52	52	194.32	194.32	Silt/sand laminae
25X-1	57	57	194.37	194.37	Silt/sand laminae
25X-1	91	91	194.71	194.71	Silt/sand laminae
25X-1	102	102	194.82	194.82	Silt/sand laminae
25X-1	113	113	194.93	194.93	Silt/sand laminae
25X-1	133	133	195.13	195.13	Silt/sand laminae

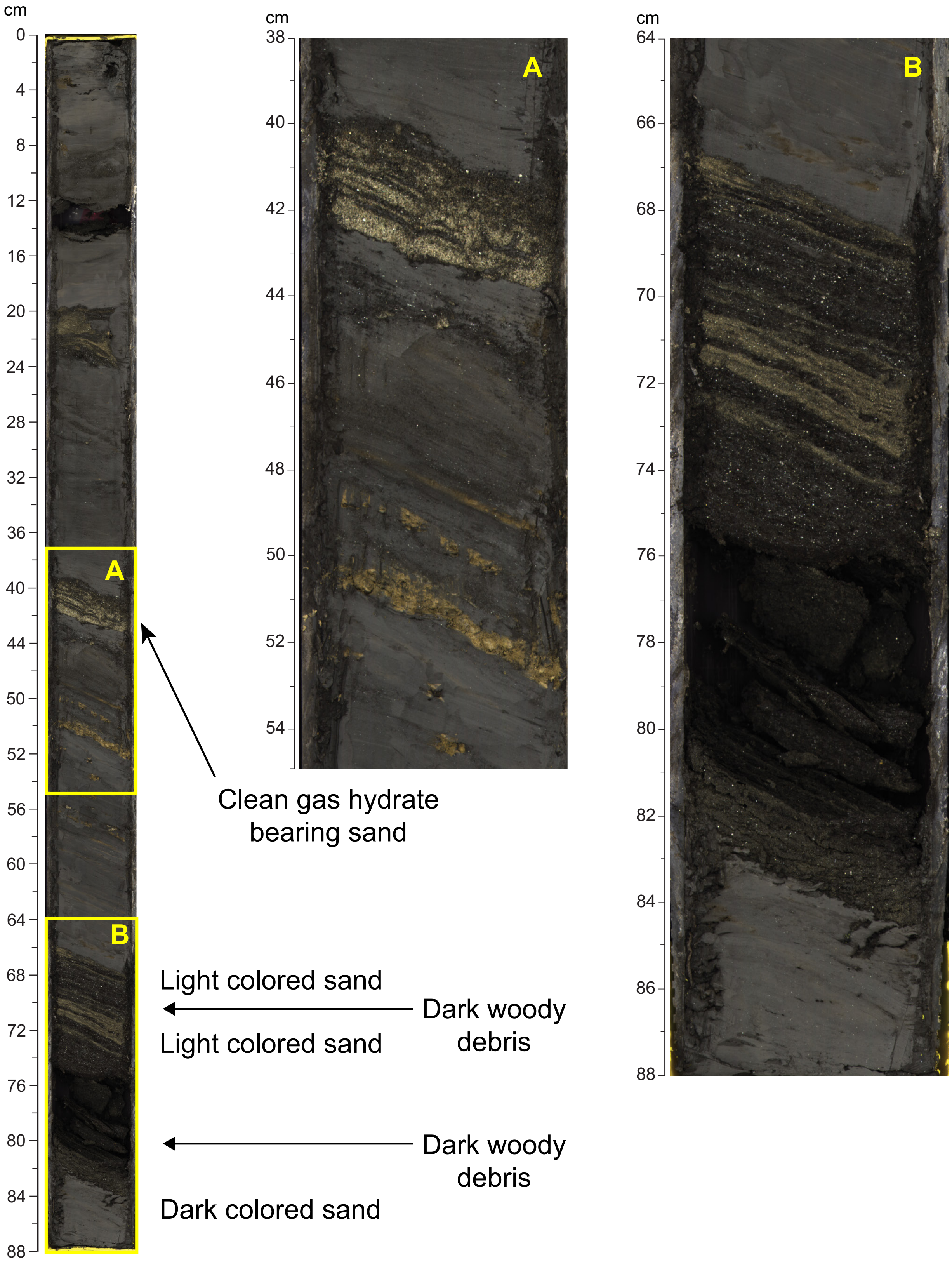

Figure 7. Terrestrial organic matter recovered at Hole NGHP-01-15A in Section NGHP-01-11Y-1. Notice the three coarse layers of sediment in B, interbedded with woody debris. Also notice the clean sand in A, where gas hydrate was observed when logged under pressure and subsequently degassed (see "Pressure Coring").

The major lithologies of Lithostratigraphic Unit I, as determined from smear slides, consist primarily of clay-sized (60–100 percent) grains with minor amounts of silt-sized grains (up to 40 percent) and some sand (up to 20 percent; table 1). Minor lithologies described in smear slide include silt/sand beds, authigenic carbonates, iron sulfide rich zones, and organic rich zones. The major nonbiogenic components of Lithostratigraphic Unit I are quartz, feldspar, mica, clay, and heavy minerals. Opaque grains, mostly sulfides in irregular and framboidal forms or heavy minerals, are common in all grain sizes, typically trace to 18 percent of the total sediment (table 1). The total biogenic component of the sediment is dominated by calcareous nannofossils, which comprise trace to 43 percent of the total (biogenic and non-biogenic) sediment grains (table 1). Foraminifera occur (trace to 4 percent) in smear slides; however, they are more abundant (trace to 80 percent) in the coarse fractions of the sediments (table 3) throughout the hole and are especially predominant in coarse fractions taken from the upper ~50 mbsf (table 3). These are often visible with the naked eye on the split core surfaces as well. Terrestrial organic matter was observed in smear slide throughout the sediments of Lithostratigraphic Unit I from trace amounts to 5 percent (table 1). Woody debris was also observed in two locations in Hole NGHP-01-14A (see fig. 8 in “Site NGHP-01-14”). Authigenic carbonate precipitates were observed in smear slides (trace to 45 percent) throughout Unit I (table 1).

Gas-Hydrate Occurrence

Gas hydrate was observed and recovered from one major zone at Site NGHP-01-15A (Core NGHP-01-15A-09X) that had several IR anomalies. Moussey texture (formed during gas-hydrate dissociation) was also observed in Core NGHP-01-15A-09X (fig. 5 and Site NGHP-01-15 Visual Core Descriptions) and resulted from the dissociation of gas hydrate that was not sampled on the catwalk. Gas hydrate was also recovered in pressure Core NGHP-01-15A-11Y (in the clean sand above the woody debris rich bed described above; see fig. 7). One additional IR anomaly was seen near the top of the core (~18 mbsf), and one chlorinity anomaly was observed at this site in the interstitial water (IW) data (see “Inorganic Geochemistry” and “Physical Properties”).

Inorganic Geochemistry

The main objectives of the inorganic geochemistry program at this site were to (1) constrain the fluid and gas source(s), subsurface hydrology (transport mechanisms and migration pathways), and biogeochemical reactions associated with subsurface gas hydrate; (2) quantify the content and distribution of gas hydrate based on dissolved chloride concentrations and (3) determine the relationship between the regional hydrogeochemistry and gas-hydrate distribution. The primary objective of the high-resolution sampling in the upper 37 m of the sediment column was to characterize the sulfate-methane interface (SMI) for future geochemical modeling studies and to provide supporting data and samples for studies on the microbial dynamics of the SMI. The IW geochemistry data are tabulated in table 4, and illustrated in figures 10 and 11.

A total of 59 whole-round samples were collected for interstitial water (IW) analyses at Site NGHP-01-15 in the KG Basin offshore the eastern margin of the Indian Peninsula. Whole-round core lengths ranged from 10 to 30 cm, with longer sections subsampled from cores recovered deeper within the hole. Samples were collected at a frequency of six samples per core in the upper 37 m, two whole-round samples per core to ~145 mbsf, and one sample per core to TD. The whole-round sampling program was coordinated with both the organic geochemistry and microbiology sampling programs. In addition to the general whole-round sampling scheme, core intervals with IR anomalies were sampled on the catwalk. The IR anomaly whole-round samples were immediately transferred to the chemistry laboratory, taken out of the core liner, split, and imaged with a hand-held IR camera. The interval with the anomaly was then separated from the whole-round sample and squeezed. If the anomaly was heterogeneous, lithologies were then separated (that is sand and clay) and squeezed separately to determine the percent pore space gas-hydrate occupancy in each sediment type. In addition to routine catwalk whole-round sampling, five pressure cores (four FPC=Y cores and one PCS pressure core) were sampled. Pressure cores were subsampled for interstitial water squeezing based on X-ray scans.

Interstitial Water Chloride—Gas-Hydrate Distribution

Chloride concentrations were measured by shipboard ion-chromatography (IC) at this site due to the paucity of indicator solution available for manual titrations after the first four sites of Leg 3 of NGHP Expedition 01. The accuracy and precision of the IC technique is not as robust as the $AgNO_3$ titration method with the percent precision of chloride values determined via the IC method averaging 0.7 percent compared to 0.2 percent by titration. Cl^- concentrations were determined shore-based via titration with $AgNO_3$ at Scripps Institute of Oceanography. The Cl^- concentration data obtained by both methods are presented in table 4 and the chloride by titration concentration-depth profile is illustrated in figure 10A. A plot comparing the Cl^- concentrations determined by both methods is shown in figure 10B. The interstitial water Cl concentrations at Site NGHP-01-15A range from 206 to 560 mM. The majority of the chloride values vary from 500 to 559 mM (modern seawater value), indicating that gas hydrate is finely dispersed at Site NGHP-01-15, with localized horizons containing more concentrated gas hydrate manifested by localized chloride anomalies ranging from 12 to 71 percent less than modern seawater chloride value. See “Pressure Coring” for examples of gas-hydrate habit in sediment. Note that Cl^- concentrations have not been corrected for seawater contamination.

Table 3. Coarse fraction (>63 µm) sieve data for Hole NGHP-01-15A.

Sample reference		Mineral										
Core, section, depth (cm, in section)	MBSF	Quartz	Feldspar	Mica	Heavy minerals	Volcanic glass	Pyrite	Iron sulfides	Framboidal pyrite	Rock fragments	Other minerals	Authigenic carbonates
NGHP-01-15A												
1H-1,80	0.8	80		trace	5		trace					
1H-6,10	7.51	85		2.5	5		5					
2H-1,120	10.8	70			5		5		5			
2H-7,10	18.2	30		2	5		5					
3H-2,67	21.27	5							10			
3H-3,122	23.32	5					5		5			
4H-1,87	29.47	10		5	5		70					
4H-3,47	32.07	80		5	5		5					
5H-2,76	40.36	85			5		5					
5H-5,62	44.72	65			5		5					
6H-2,54	49.43	80		3	5		5					
6H-5,55	53.85	80		2	5		5					
7H-1,143	58.53	85		7	5		0.5					
7H-3,13	60.14	85		5	5							
8H-4,55	70.61	85			5		5					
9H-4,15	79.68	70		10	10							
12H-2,70	89.9	85			5		5					
13H-4,60	102.4	10		trace	5		5		80			
14X-1,70	107.6	70		5	5		5		2		3	
14X-6,70	114.02	30		3	10		50	2	trace			
16Y-1,65	116.65	85		trace	5							
17X-3,109	119.98	80		5	5		5					
18X-2,70	128.8	80		5	10		5					
18X-5,75	133.35	85		5	5		5					
19X-2,70	138.4	90		trace	5		5					
20X-1,86	146.66	60		5	5		5		5			
20X-4,50	150.8	80		2.5	5		5					
21X-1,66	156.06	80		trace	5		5		5			
21X-5,54	161.94	60		5	5		20		5			
22X-1,74	165.74	85			5		5					
22X-5,78	170.88	85		5	2.5		2.5					
23X-2,78	175.59	80		5	5		5					
23X-5,68	179.99	85		5	5		5					
24X-3,51	187.71	90		5	5							
24X-5,130	191.5	95		trace	5							
25X-3,100	197.8	85		5	5		5					

Table 3. Coarse fraction (>63 μm) sieve data for Hole NGHP-01-15A.—Continued

Sample reference		Biogenic									
Core, section, depth (cm, in section)	MBSF	Fora-minifera	Carbonate shell fragments	Diatoms	Radio-larians	Silico-flagellates	Siliceous shell fragments	Sponge spicules	Other biogenic	Plant debris	Comments
NGHP-01-15A—Continued											
1H-1,80	0.8	10	5								
1H-6,10	7.51	trace	2.5								
2H-1,120	10.8	10	5								
2H-7,10	18.2	50	5							3	
3H-2,67	21.27	80	5								
3H-3,122	23.32	80	5								
4H-1,87	29.47	5	5								
4H-3,47	32.07		5								
5H-2,76	40.36	2.5	2.5								
5H-5,62	44.72	20	5								
6H-2,54	49.43		7								
6H-5,55	53.85	3	5								
7H-1,143	58.53		2.5								
7H-3,13	60.14		5								
8H-4,55	70.61		5								
9H-4,15	79.68		5							5	
12H-2,70	89.9		5								
13H-4,60	102.4										
14X-1,70	107.6	5						3	2		Other biogenic is fish remains
14X-6,70	114.02	4							1		
16Y-1,65	116.65		5							5	
17X-3,109	119.98	2								3	
18X-2,70	128.8		trace								
18X-5,75	133.35										
19X-2,70	138.4										
20X-1,86	146.66	20									
20X-4,50	150.8	5								2.5	
21X-1,66	156.06	5									
21X-5,54	161.94		5								
22X-1,74	165.74		5								
22X-5,78	170.88	5									
23X-2,78	175.59		5								
23X-5,68	179.99										
24X-3,51	187.71		trace								
24X-5,130	191.5										
25X-3,100	197.8										

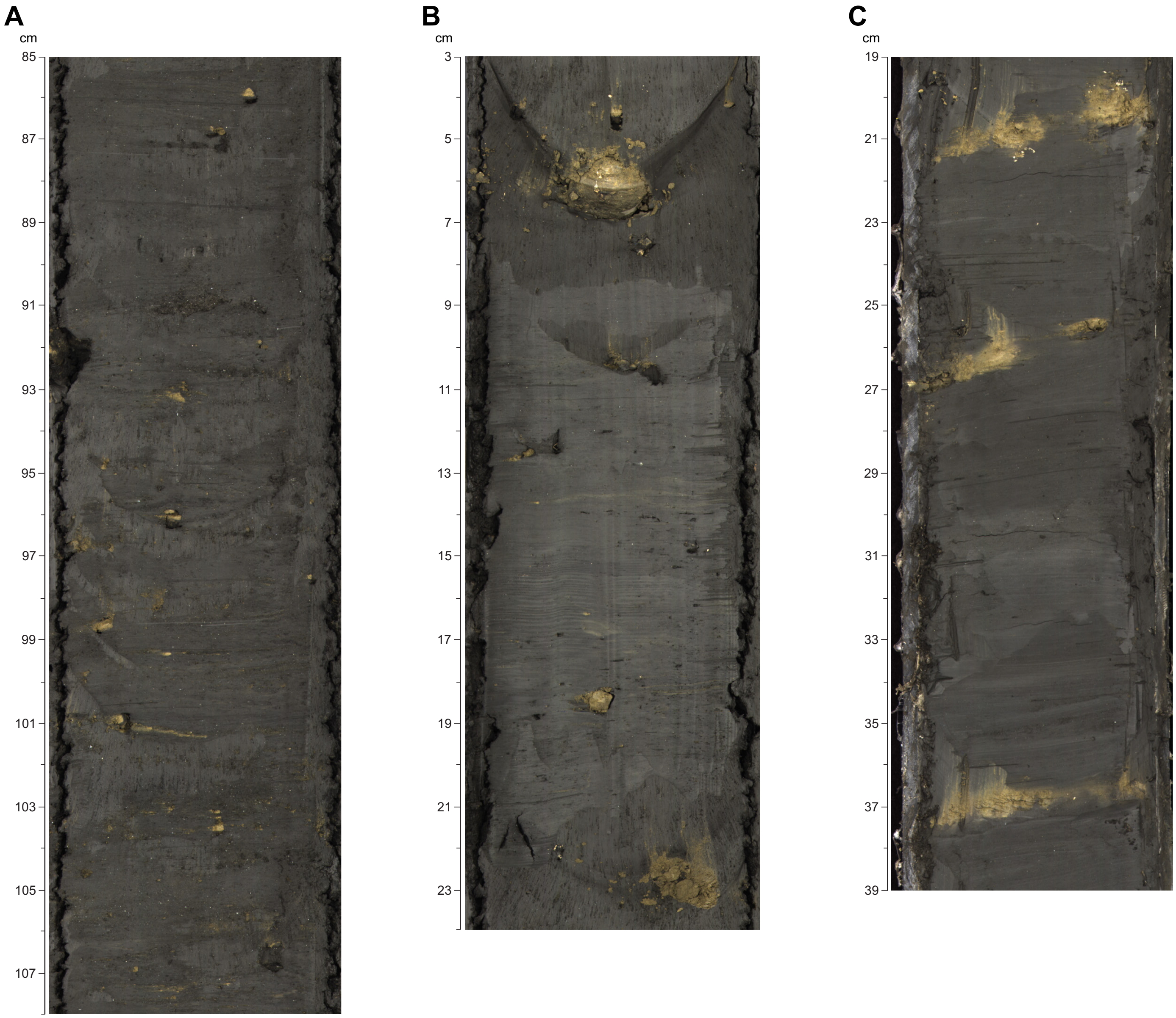

Figure 8. Authigenic carbonate nodules (>1 cm), micronodules (<1 cm), and bands. A, Section NGHP-01-15A-12H-1, 85–108 cm, micronodules; B, Section NGHP-01-15A-14X-2, 3-24 cm, nodules; C, Section NGHP-01-15A-16Y-1, 19–39 cm, bands.

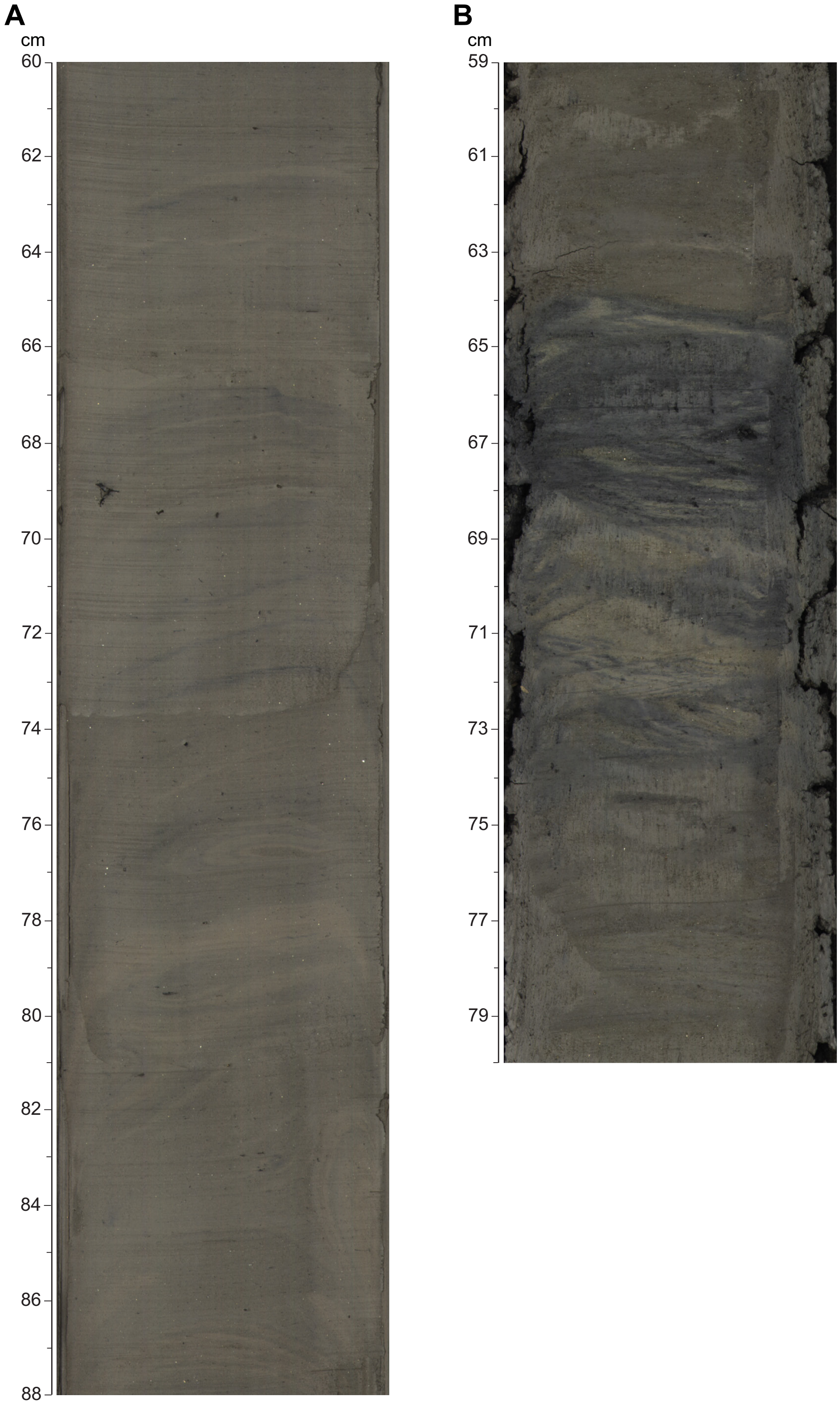

Figure 9. Iron monosulfides (dark black precipitates). A, Section NGHP-01-15A-02H-2, 60–88 cm. B, Section NGHP-01-15A-19X-4, 59–80 cm.

Table 4. Interstitial-water data for Hole NGHP-01-15A. Note that a dash indicates the value was not determined.

[BDL, below detection limit]

Core, section	Top (cm)	Bottom (cm)	Depth (mbsf)	Volume (ml)	pH	Alkalinity (mM)	Salinity	Cl^- by Titration	Cl^- by IC (mM)	Br^- (mM)	SO_4^{2-} (mM)	Comments
						NGHP-01-15A						
1H-1	140	150	1.4	29	7.5	13.83	34.0	-	538.7	0.85	8.27	
1H-2	140	150	2.9	27	7.4	13.83	33.8	-	552.8	0.89	7.53	
1H-3	140	150	4.4	27	7.2	13.83	33.3	-	552.7	0.90	6.78	
1H-4	140	150	5.9	24	7.5	13.51	33.0	556.3	550.2	0.89	6.05	
1H-5	140	150	7.4	22.5	7.4	12.72	33.0	560.0	549.8	0.89	2.68	
1H-6	140	150	8.9	24	7.5	12.03	32.5	559.4	550.5	0.90	0.20	
2H-1	140	150	11.0	21	7.6	-	33.0	554.0	548.7	0.90	1.30	
2H-2	140	150	12.5	21	7.6	25.18	33.3	552.0	547.1	0.88	3.25	
2H-3	140	150	14.0	21	7.7	24.45	34.0	553.9	547.5	0.89	5.52	
2H-4	140	150	15.5	22	7.8	22.64	34.5	557.0	545.4	0.89	7.81	
2H-6	140	150	18.5	25	7.9	17.08	34.5	556.8	552.6	0.88	11.43	
2H-7	65	75	19.3	25	7.8	14.74	34.0	556.8	551.3	0.88	12.07	
3H-1	140	150	20.5	25	7.9	13.32	34.5	559.8	544.9	0.87	13.28	
3H-2	140	150	22.0	25	7.9	13.10	34.5	558.1	545.4	0.85	13.22	
3H-3	140	150	23.5	20	8.0	12.75	34.3	559.3	548.1	0.86	12.79	
3H-4	140	150	25.0	23	8.0	13.25	34.5	557.7	551.2	0.85	11.71	
3H-5	140	150	26.5	25	8.0	15.26	34.8	559.7	531.3	0.86	9.18	
3H-6	140	150	28.0	20	7.9	17.22	34.8	546.3	524.3	0.84	6.29	
3H-7	60	70	28.7	24	7.9	18.83	34.0	564.1	554.8	0.89	5.00	
4H-1	140	150	30.0	25	8.1	20.95	33.0	560.4	547.9	0.89	1.23	
4H-2	140	150	31.5	23	8.1	21.13	-	560.8	552.9	0.91	BDL	
4H-3	140	150	33.0	25	8.1	22.54	32.5	551.7	550.5	0.92	BDL	
4H-4	140	150	34.5	24	8.1	24.68	33.3	552.9	555.8	0.91	BDL	
4H-5	140	150	36.0	23	8.1	24.56	33.0	553.1	551.3	0.91	BDL	
4H-6	90	100	37.0	26	8.2	24.82	-	555.7	547.6	0.94	BDL	
5H-3	140	150	42.5	25	8.1	27.31	33.8	557.6	552.9	1.01	BDL	
5H-5	140	150	45.5	22	8.1	26.72	33.0	559.7	549.4	1.03	BDL	
6H-3	130	150	51.7	26.5	8.0	27.75	33.5	-	545.8	1.09	0.16	
6H-5	130	150	54.6	27	8.0	28.00	34.5	-	545.6	1.12	BDL	
7H-3	76	96	60.8	23	8.0	28.11	32.3	539.0	490.7	1.04	BDL	
7H-5	95	115	63.4	16.5	7.9	33.05	33.0	546.1	525.3	1.16	BDL	
8H-4	117	137	71.2	30	8.0	28.44	30.0	-	500.4	1.18	BDL	
8H-5	119	139	72.6	28	8.0	-	34.5	552.1	540.2	1.28	BDL	
9X-1	130	150	77.4	27	7.9	26.12	29.0	476.6	463.2	1.06	3.94	
9X-3	40	70	79.2	27	8.7	11.11	9.5	205.8	175.7	0.40	BDL	Sand
9X-3	40	70	79.2	11	-	21.78	32.3	542.8	539.6	1.35	2.43	Clay
11Y-1	26	39	87.0	14	-	-	33.0	546.1	-	-	-	
11Y-1	39	44	87.1	3	-	-	25.0	407.7	436.4	1.04	3.49	
11Y-1	72	75	87.4	4.5	-	-	33.0	550.2	537.0	1.41	1.86	
12X-3	120	150	91.9	17.5	7.6	39.72	33.0	536.8	526.2	1.36	0.46	
12X-5	120	150	94.9	18	7.9	38.32	33.0	536.1	522.4	1.35	0.49	
13X-2	120	150	100.0	24	7.8	-	34.0	538.5	536.5	1.42	0.59	
13X-4	120	150	103.0	20	7.9	37.59	33.5	538.6	534.9	1.41	0.44	
14X-3	120	150	111.1	20	8.0	33.43	33.0	544.8	536.0	1.43	0.25	
14X-5	40	77	113.0	26	7.9	33.67	32.5	535.5	527.4	1.45	BDL	
15P-1	52	72	115.5	3	-	-	33.0	535.0		-	-	
16Y-1	29	38	116.3	10	-	-	32.5	541.7	543.2	1.46	0.68	
17X-2	120	150	118.6	21	8.0	-	32.0	536.6	530.3	1.45	0.21	
17X-4	36	66	120.8	20.5	8.0	29.27	32.5	540.1	613.4	1.68	BDL	
18X-3	120	150	130.8	18	8.0	23.76	32.5	539.8	522.9	1.46	0.17	
18X-5	120	150	133.8	21	8.1	20.40	32.0	542.8	532.0	1.47	0.37	
19X-1	120	150	137.4	26	8.1	20.16	32.0	539.2	535.0	1.50	0.30	
19X-3	120	150	140.4	24	8.0	21.78	32.3	537.9	528.9	1.52	BDL	
20X-3	120	150	150.0	24	8.2	26.62	32.3	533.8	541.9	1.53	BDL	
21X-3	120	150	159.6	14	8.2	24.96	31.5	527.7	542.8	1.60	BDL	
22X-3	40	70	168.3	19.5	7.9	26.52	32.0	531.1	518.5	1.51	0.33	
23X-3	120	150	177.5	17	8.0	24.13	31.3	524.6	511.5	1.52	BDL	
24X-3	120	150	188.4	16	8.0	20.43	-	521.5	-	-	-	
25X-2	120	150	196.5	16.5	8.0	17.32	30.0	515.7	526.5	1.59	BDL	

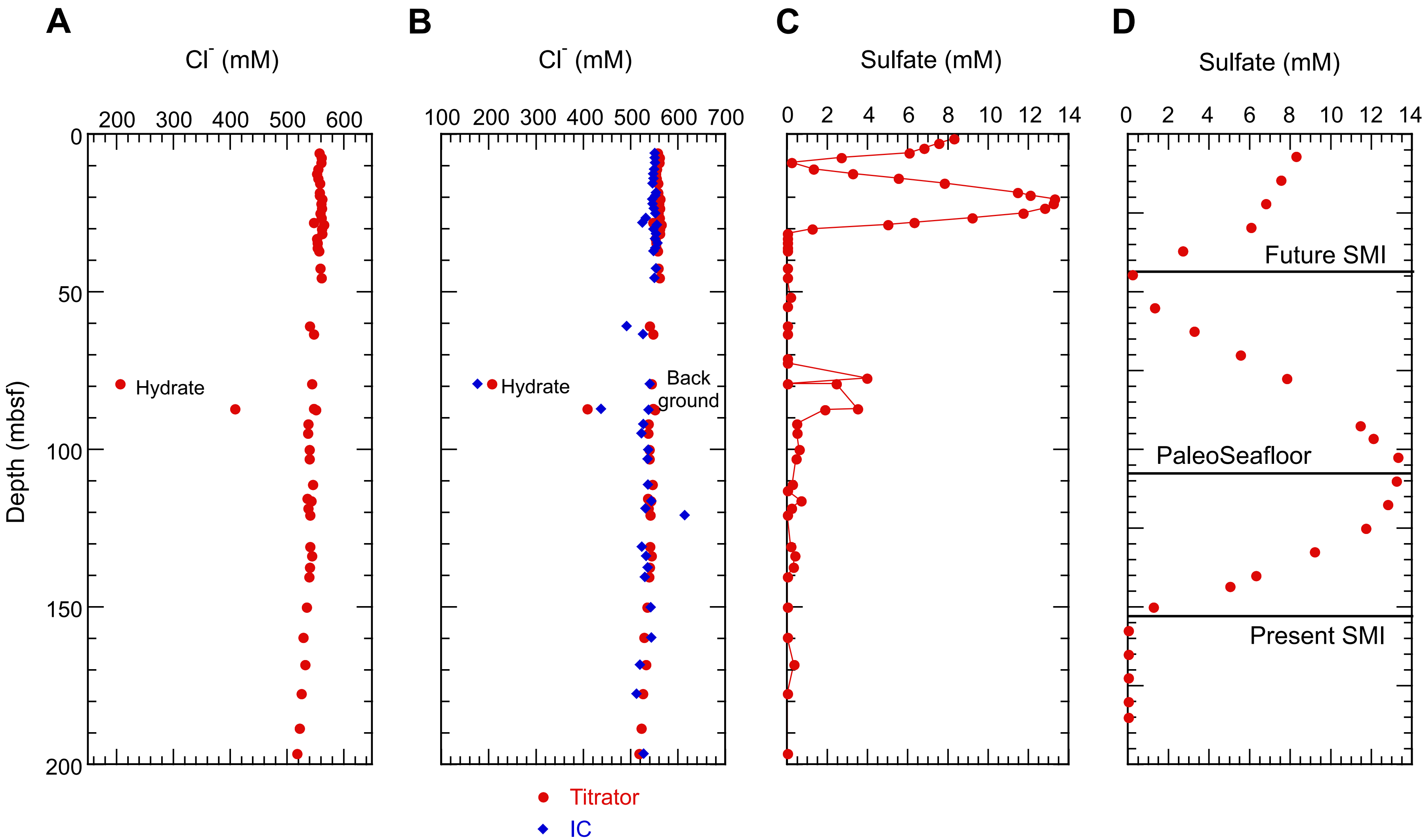

Figure 10. Interstitial water composition depth profiles of A, chloride determined via titration (shore-based at Scripps Institution of Oceanography; error is ±0.2 percent) containing sample NGHP-01-15A-09X-3, 40–70 cm; B, chloride determined via titration without NGHP-01-15A-09X-3, 40–70 cm; C, concentration depth profile of Cl^- determined via both titration and ion chromatography; D, sulfate in the upper 37 m of Site NGHP-01-15A showing the present day SMI, the inferred paleo-seafloor, and the inferred depth of the future SMI. Short solid lines indicate the bottoms of Cores NGHP-01-15A-01H, NGHP-01-15A-02H, and NGHP-01-15A-03H; E, sulfate to TD; F, alkalinity; G, bromide. [SMI, sulfate methane interface; TD, total depth]

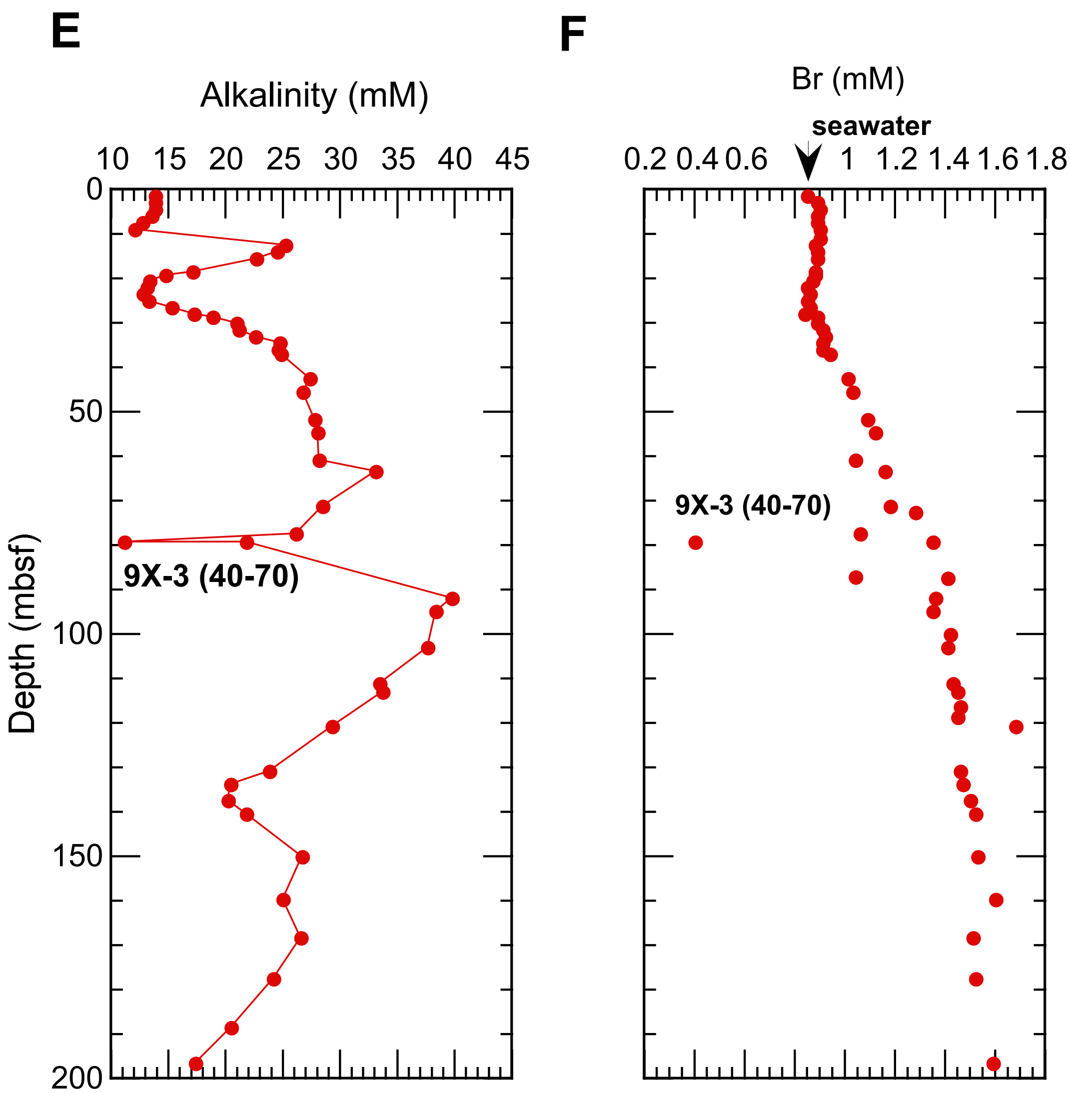

Figure 10. Interstitial water composition depth profiles of A, chloride determined via titration (shore-based at Scripps Institution of Oceanography; error is ±0.2 percent) containing sample NGHP-01-15A-09X-3, 40–70 cm; B, chloride determined via titration without NGHP-01-15A-09X-3, 40–70 cm; C, concentration depth profile of Cl^- determined via both titration and ion chromatography; D, sulfate in the upper 37 m of Site NGHP-01-15A showing the present day SMI, the inferred paleo-seafloor, and the inferred depth of the future SMI. Short solid lines indicate the bottoms of Cores NGHP-01-15A-01H, NGHP-01-15A-02H, and NGHP-01-15A-03H; E, sulfate to TD; F, alkalinity; G, bromide. [SMI, sulfate methane interface; TD, total depth]—Continued

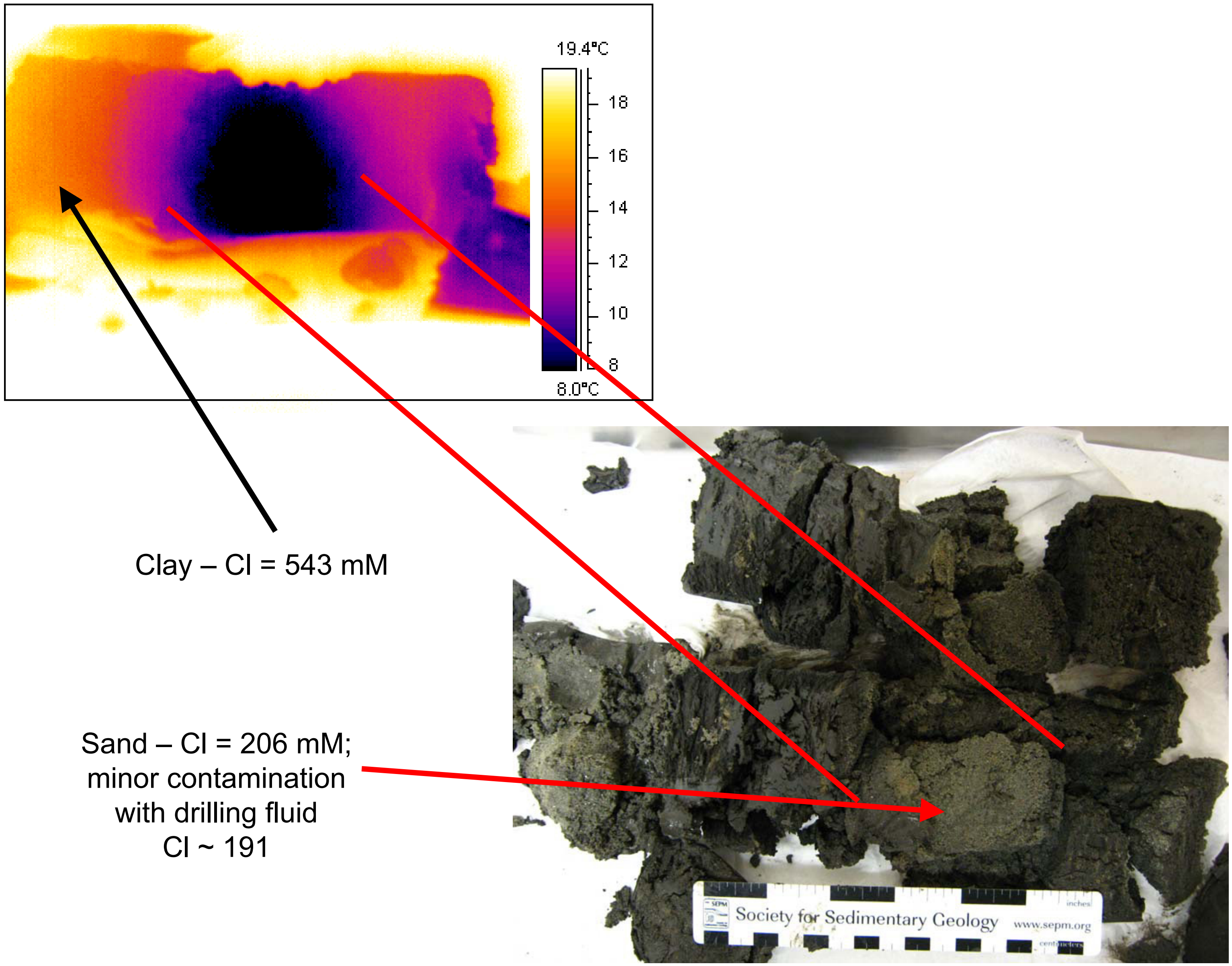

Figure 11. A, Infrared image of the gas hydrate bearing sand (blue) surrounded by clay (pink to red) before sample NGHP-01-15A-09X-3, 40–70 cm was cut in half in the chemistry laboratory. B, Visible spectrum photograph of sample NGHP-01-15A-09X-3, 40–70 cm after it was cut in half showing both the sand and clay layers. Note the scale bar at the bottom of the picture.

Chloride concentrations are variable from the seafloor to 25 mbsf and range from 3.6 percent less than modern seawater value to modern seawater concentration (559 mM). The 3.6 percent dilution at the top of the section is greater than the precision of the analytical technique, indicating that some of the variability reflects *in situ* changes in pore water chlorinity, likely glacial/interglacial. From 25 mbsf to the base of Hole NGHP-01-15A, most of the samples exhibit Cl concentrations only slightly depleted with respect to modern seawater value. Overprinted on this disseminated distribution of gas hydrate are four excursions characterized by depleted pore water chloride concentrations of up to 63 percent less than modern seawater value, indicating elevated concentrations of gas hydrate. The first excursion occurs at ~28 mbsf where chloride values sharply drop to 546 mM (6 percent less than modern seawater value) from a background concentration of ~560 mM. The second excursion occurs at ~60 mbsf where chloride concentrations decrease sharply from ~559 mM to ~539 mM (4 percent less than modern seawater value). The third depth with Cl^- minima occurs at ~79 mbsf, where values decrease from 552 mM to 476 mM in sample NGHP-01-15A-09X-3, 40-70 cm, reaching a minimum value of 206 mM (63 percent seawater value) corresponding to sample NGHP-01-15A-09X-3, 40-70 cm. This sample exhibited a strong IR anomaly on the catwalk, and upon visual inspection was determined to be a sand-bearing section. Gas hydrate was inferred to be up to 50 percent pore space at ~80 mbsf by downhole logging analysis (see “Downhole Logging”). The sample was immediately transferred to the chemistry laboratory, where it was carefully taken out of the core liner, imaged with a hand-held IR camera, and cut in half. Most of the section was a coarse-grained sand that was bound on both sides by clay-rich sediment (fig. 11). Only the sandy interval produced an IR anomaly, whereas the clay intervals exhibited temperatures close to that of the ambient laboratory temperature (fig. 11). Samples of these lithologies were then separated and squeezed for interstitial water. The chloride concentration minimum of 206 mM (191 mM after correction for drilling-induced contamination; 66 percent less than modern seawater) was associated with the sandy interval while the clay section exhibited a concentration of 543 mM, indicating the distribution of gas hydrate in this sample is strongly controlled by lithology. The fourth excursion in chloride concentrations occurs at ~87 mbsf where chloride concentrations drop from background values to 408 mM (~25 percent less than modern seawater value). At Site NGHP-01-15, the control of lithology on gas-hydrate distribution was only observed in sample NGHP-01-15A-09X-3, in the sand that contained concentrated gas hydrate, whereas the other three moderate Cl^- anomalies occurred in clay bearing sections.

Sulfate Concentrations: Characterization of the SMI

The primary objectives of the high-resolution sampling in the upper 37 m of sediments at this site were to characterize the sulfate-methane interface (SMI) for future geochemical modeling of methane fluxes and to provide supporting data and samples for studies on the microbial dynamics of the sulfate-methane interface. The top 30 m of the sulfate concentration depth profile at Site NGHP-01-15 exhibits an S-shaped pattern (fig. 10E). The sulfate value of the first whole-round sample (at 1.4 mbsf) is 8.3 mM (~¼ seawater value), indicating the mud-line was missed in the first APC core, thus the top meter of the core was lost. Sulfate concentrations decrease from 8.3 mM to near depletion at ~9 mbsf, then increase to 13.3 mM at 22 mbsf (fig. 10C). Below 22 mbsf, SO_4^{2-} concentrations decrease at a rate of ~2.5 mM per meter to depletion at 31.5 mbsf. At this depth there is a concomitant rise in head-space methane concentrations from levels below the detection limit (see “Organic Geochemistry”). The S-shaped concentration profile likely reflects a recent rapid sedimentation event. Prior to the putative rapid depositional event, the SO_4^{2-} concentration maximum of 13.3 mM, now positioned at 22 mbsf, was likely near the seafloor in direct communication with the overlying bottom water, and the present day SMI was located at approximately 8 mbsf. The rapid sedimentation event deposited new organic matter and entrained seawater resulting in pore waters enriched in SO_4^{2-}, thus burying the paleoseafloor and shifting the primary site of sulfate consumption to the upper 10 m of the sediment section (fig. 10C, there is no direct evidence of a change in lithology or physical properties to support this). The most active SO_4^{2-} consumption is presently occurring at 9 mbsf, and, as a result, sulfate is diffusing to this SO_4^{2-} minimum depth from the sediment sections above and below it. Because presently sulfate is not being supplied to the buried sediments (that is, the paleo-seafloor) by diffusion from seawater, sulfate will become progressively depleted from 9 to 30 mbsf, and the depth of the SMI will shift to 9 mbsf. The inferred shallow depth of the SMI at this site indicates that the methane flux is relatively high in comparison to other sites in the Krishna-Godavari Basin. Below the SMI, SO_4^{2-} values remain depleted with spikes in sulfate concentrations reflecting contamination of samples by drilling fluid (fig. 10D). Concentrations in the contaminated samples will be used to compute the amount of seawater that infiltrated the sample during drilling, because SO_4^{2-} is depleted within this interval. Using a simple two-member mixing model between seawater and SO_4^{2-}-depleted formation fluid, the percent contamination of the sample can be quantified.

Alkalinity and Bromide

The alkalinity concentration depth profile in the upper 30 m at Site NGHP-01-15 mirrors the sulfate profile and exhibits a Z-shaped pattern (fig. 10E). Alkalinity decreases slightly from 13.83 mM at 1.4 mbsf to 12.03 mM at 8.9 mbsf. The alkalinity between these depths is ~5.5 times modern seawater value reflecting sulfate reduction by organic matter oxidation producing elevated alkalinity. The slight decrease in concentration between the seafloor and 9 mbsf likely reflects minor precipitation of authigenic carbonates. Between 9 mbsf and 14 mbsf, in the depth interval where SO_4^{2-} concentrations decrease, alkalinity concentrations increase due to the high rates of sulfate reduction. Between 14 mbsf and 23 mbsf, alkalinity decreases dramatically and is coincident with an increase in sulfate concentrations interpreted to represent the paleo-seafloor subsequently buried during a rapid sedimentation event. Between 22 and 31.5 mbsf, alkalinity concentrations increase and reflect both sulfate reduction and alkalinity production by organic matter oxidation and anaerobic methane oxidation at the SMI. The alkalinity concentration depth profile below the SMI at Site NGHP-01-15 is almost identical to that of nearby Site NGHP-01-14 with the exception of a zone of depleted alkalinity to 11.11 mM at ~79 mbsf. The region of low alkalinity between 77 and 79 mbsf corresponds to samples NGHP-01-15A-09X-1 and NGHP-01-15A-09X-3 that exhibit anomalously low dissolved Cl^- and Br^- concentrations due to gas-hydrate dissociation during the core recovery process contributing fresh water to the pore fluids. Alkalinty concentrations then increase to a maximum of ~40 mM at 92 mbsf and may reflect elevated *in situ* methane production from acetate fermentation to a depth of approximately 103 mbsf controlling CO_2 concentrations, thus affecting carbonate dissolution (fig. 10E). Below this depth, alkalinity concentrations decrease steadily to a value of 23.78 mM just below the seismically-inferred BSR at ~125 mbsf after which alkalinity is variable ranging from 17 to 27 mM.

Bromide concentrations in marine interstitial waters are sensitive to organic matter diagenesis, with concentrations higher than seawater reflecting organic matter decomposition. Bromide concentrations are near seawater value and relatively constant to ~ 30 mbsf coincident with the present-day SMI (fig. 10F), and may reflect selective decomposition of terrestrial organic matter over marine organic matter. Below the SMI, Br^- concentrations increase from 0.89 mM to 1.35 mM at 80 mbsf reflecting marine organic matter decomposition and coincident methane production resulting in progressive Br^- enrichment with depth. Bromide minima below 30 mbsf are the result of gas-hydrate dissociation during the core retrieval process as observed in the Cl^- concentration depth profile (figs. 10A and 10B). Below 80 mbsf, Br^- concentrations increase less with depth from 1.35 mM to 1.59 mM at 195 mbsf. A spike in Br^- concentrations occurs at ~120 mbsf, approximately 6 m above the seismically-inferred BSR, and is coincident with a maximum in Cl^-.

Organic Geochemistry

Organic geochemical studies at Site NGHP-01-15 (GDGH-11) included analysis of the composition of volatile hydrocarbons including methane, ethane, and propane (C_1–C_3) and fixed natural gases (that is, O_2, CO_2, and N_2+Ar) from headspace, void gas, and pressure core sampler (PCS) degassing experiments. In general, these analyses indicate that methane is the predominant hydrocarbon gas found in the cores at Site NGHP-01-15. Ethane was measurable in void gas and PCS samples at depths greater than ~40 mbsf. The headspace samples of sections overlying the sulfate-methane interface (SMI) were dominated by air and slightly depleted in carbon dioxide. Methane was moderately enriched just below the SMI, then decreased gradually through the seismically-inferred bottom-simulating reflector (BSR). Specific details of the shipboard gas chemistry results for Site NGHP-01-15, Hole A are provided in the following discussion.

Headspace gas analyses were performed on 57 samples from Hole NGHP-01-15A ranging in depth from 1.35 to 196.05 meters below seafloor (mbsf). The concentrations given here represent minimum proxy measurements of the actual concentrations due to limitations of the gas headspace method (Kvenvolden and Lorenson, 2000). The sediment pore water contained methane at concentrations ranging from non-detectable near the surface to 8.4 mM at ~35.6 mbsf (table 5), with an average concentration of 1.45 mM. Theoretical methane saturation in pore water under site-specific physical conditions, calculated using the Duan and others (1992) and Xu (2002, 2004) methodologies, ranges from 68.8 mM at the seafloor to 116.5 mM at 130 mbsf, then declines to 115.1 mM near the borehole completion depth of 210 mbsf. C_2 and C_3 hydrocarbon gases were not detected in headspace samples indicating a biogenic source of methane; however post expedition isotopic analyses will further constrain gas sources. Methane concentrations increase rapidly from non-detectable to 2.4 mM just above 31.5 mbsf, constraining the depth of the sulfate-methane interface (SMI) (fig. 12). Below the SMI, methane concentrations gradually decreased to less than 1 mM just below the bottom-simulating reflector (BSR). Methane concentrations increased to nearly 4 mM at ~45 m below the BSR. The headspace methane concentrations were generally more than an order of magnitude below saturation throughout the length of the borehole (fig. 12).

Carbon dioxide (CO_2) concentrations ranged from 0.8 to 19.5 mM in pore water contained within the sediment. An equivalent concentration expression of gas volume to sediment volume ranges from ~10,300 to nearly 212,800 microliters CO_2/liter wet sediment (table 4). CO_2 concentrations decrease at a rate of approximately 0.1 mM per meter from seafloor to the SMI (~28 mbsf). CO_2 levels then exhibited an increase through the SMI to ~90 mbsf, followed by a gentle decrease to the borehole completion depth of 220 mbsf.

Table 5. Headspace gas composition for Site NGHP-01-15.

Sample	Site	Hole	Core	Section	Interval (cm)	Sed wt. (g)	Sample depth (mbsf)	CO_2 (ppm-v)	C_1	C_2 (ppm-v)	C_3
15A-1H1-135-140	15	A	1	1	135–140	5.6	1.35	10,900	nd	nd	nd
15A-1H2-135-140	15	A	1	2	135–140	5.8	2.85	12,000	nd	nd	nd
15A-1H3-105-110	15	A	1	3	105–110	7.0	4.05	14,500	nd	nd	nd
15A-1H4-135-140	15	A	1	4	135–140	5.3	5.85	12,700	nd	nd	nd
15A-1H5-95-100	15	A	1	5	95–100	6.3	6.95	10,400	nd	nd	nd
15A-1H6-135-140	15	A	1	6	135–140	5.8	8.85	10,900	nd	nd	nd
15A-2H1-135-140	15	A	2	1	135–140	6.7	10.95	11,800	nd	nd	nd
15A-2H2-135-140	15	A	2	2	135–140	7.5	12.45	10,300	nd	nd	nd
15A-2H3-105-110	15	A	2	3	105–110	5.1	13.65	10,700	nd	nd	nd
15A-2H4-135-140	15	A	2	4	135–140	8.4	15.45	10,900	nd	nd	nd
15A-2H5-95-100	15	A	2	5	95–100	9.0	16.55	9,600	nd	nd	nd
15A-2H6-135-140	15	A	2	6	135–140	8.2	18.45	5,600	nd	nd	nd
15A-2H7-135-141	15	A	2	7	60–65	8.3	19.20	5,300	nd	nd	nd
15A-3H1-135-140	15	A	3	1	135–140	8.2	20.45	6,600	nd	nd	nd
15A-3H2-135-140	15	A	3	2	135–140	7.9	21.95	3,900	nd	nd	nd
15A-3H3-105-110	15	A	3	3	105–110	7.1	23.15	4,700	nd	nd	nd
15A-3H4-135-140	15	A	3	4	135–140	7.5	24.95	3,200	nd	nd	nd
15A-3H5-95-100	15	A	3	5	95–100	9.0	26.05	6,200	nd	nd	nd
15A-3H6-135-140	15	A	3	6	135–140	7.9	27.95	3,600	nd	nd	nd
15A-3H7-55-60	15	A	3	7	55–60	9.0	28.65	7,800	nd	nd	nd
15A-4H1-135-140	15	A	4	1	135–140	6.8	29.95	12,800	700	nd	nd
15A-4H2-135-140	15	A	4	2	135–140	7.6	31.45	16,300	9,500	nd	nd
15A-4H3-105-110	15	A	4	3	105–110	7.0	32.65	12,200	18,300	nd	nd
15A-4H4-135-140	15	A	4	4	135–140	7.3	34.45	11,900	31,000	nd	nd
15A-4H5-95-100	15	A	4	5	95–100	7.4	35.55	11,100	28,900	nd	nd
15A-4H6-85-90	15	A	4	6	85–90	10.7	36.95	12,600	8,400	nd	nd
15A-5H3-105-110	15	A	5	3	105–110	7.0	42.15	19,100	14,900	nd	nd
15A-5H5-95-100	15	A	5	5	95–100	6.5	45.05	20,300	14,300	nd	nd
15A-6H3-95-100	15	A	6	3	95–100	6.4	51.34	35,300	7,500	nd	nd
15A-6H5-85-90	15	A	6	5	85–90	6.9	54.15	36,000	9,200	nd	nd
15A-7H3-41-46	15	A	7	3	41–46	7.1	60.42	33,400	6,500	nd	nd
15A-7H5-50-55	15	A	7	5	50–55	7.9	62.97	39,100	8,900	nd	nd
15A-8H4-82-87	15	A	8	4	82–87	6.5	70.88	24,500	5,800	nd	nd
15A-8H5-71-76	15	A	8	5	71–76	6.8	72.14	23,900	8,400	nd	nd
15A-9X1-125-130	15	A	9	1	125–130	13.3	77.35	34,300	19,200	nd	nd
15A-9X2-68-73	15	A	9	2	68–73	10.2	78.28	48,800	14,400	nd	nd
15A-9X4-64-69	15	A	9	4	64–69	8.2	80.17	25,800	5,600	nd	nd
15A-11Y-30-32	15	A	11	Y	30–32	10.1	86.99	15,500	600	nd	nd
15A-12X3-85-90	15	A	12	3	85–90	8.9	91.55	83,800	9,000	nd	nd
15A-12X5-75-80	15	A	12	5	75–80	9.6	94.45	57,600	7,400	nd	nd
15A-13X2-85-90	15	A	13	2	85–90	10.4	99.65	34,800	8,800	nd	nd
15A-13X4-75-80	15	A	13	4	75–80	9.1	102.55	61,900	8,700	nd	nd
15A-14X3-85-90	15	A	14	3	85–90	12.2	110.75	16,200	3,400	nd	nd
15A-14X4-145-150	15	A	14	4	145–150	10.0	112.50	15,400	2,300	nd	nd
15A-16Y-23-24	15	A	16	Y	23–24	11.6	116.23	32,600	5,000	nd	nd
15A-17X3-0-5	15	A	17	3	0–5	10.1	118.89	16,100	4,400	nd	nd
15A-17X4-31-36	15	A	17	4	31–36	11.3	120.70	53,700	8,400	nd	nd
15A-18X3-85-90	15	A	18	3	85–90	11.1	130.45	9,900	2,600	nd	nd
15A-18X5-75-80	15	A	18	5	75–80	17.0	133.35	31,900	9,400	nd	nd
15A-19X1-85-90	15	A	19	1	85–90	11.6	137.05	19,900	7,300	nd	nd
15A-19X3-75-80	15	A	19	3	75–80	8.5	139.95	20,400	5,500	nd	nd
15A-20X3-75-80	15	A	20	3	75–80	9.4	149.55	13,700	5,100	nd	nd
15A-21X3-75-80	15	A	21	3	75–80	9.3	159.15	28,900	8,500	nd	nd
15A-22X2-135-140	15	A	22	2	135–140	8.8	167.85	22,100	5,400	nd	nd
15A-23X3-75-80	15	A	23	3	75–80	9.8	177.06	23,900	15,400	nd	nd
15A-24X3-75-80	15	A	24	3	75–80	7.7	187.95	9,500	7,500	nd	nd
15A-25X2-75-80	15	A	25	3	75–80	7.8	196.05	10,400	6,200	nd	nd

Table 5. Headspace gas composition for Site NGHP-01-15.–Continued

Sample	O_2	N_2+Ar	H_2S	C_1	C1	CO_2	CO_2	C_1/CO_2
		(ppm-v)		(mL/L WS)	(mM PW)	(mL/L WS)	(mM PW)	
15A-1H1-135-140	187,800	748,700	nd	nd	nd	50,600	3.0	-
15A-1H2-135-140	186,400	751,900	nd	nd	nd	53,000	3.4	-
15A-1H3-105-110	183,000	753,800	nd	nd	nd	50,600	3.4	-
15A-1H4-135-140	183,600	749,200	nd	nd	nd	62,700	4.3	-
15A-1H5-95-100	184,800	752,800	nd	nd	nd	41,700	2.9	-
15A-1H6-135-140	188,300	748,500	nd	nd	nd	48,300	3.5	-
15A-2H1-135-140	188,700	746,100	nd	nd	nd	43,800	3.2	-
15A-2H2-135-140	181,600	726,700	nd	nd	nd	33,000	2.5	-
15A-2H3-105-110	186,000	742,700	nd	nd	nd	55,400	4.1	-
15A-2H4-135-140	182,500	750,700	nd	nd	nd	29,800	2.3	-
15A-2H5-95-100	181,600	742,800	nd	nd	nd	24,000	1.8	-
15A-2H6-135-140	187,900	747,100	nd	nd	nd	15,800	1.2	-
15A-2H7-135-141	181,200	751,200	nd	nd	nd	14,700	1.1	-
15A-3H1-135-140	185,000	747,300	nd	nd	nd	18,800	1.5	-
15A-3H2-135-140	186,300	753,300	nd	nd	nd	11,600	0.9	-
15A-3H3-105-110	184,600	750,000	nd	nd	nd	16,100	1.3	-
15A-3H4-135-140	184,200	754,300	nd	nd	nd	10,300	0.8	-
15A-3H5-95-100	183,000	756,000	nd	nd	nd	15,400	1.2	-
15A-3H6-135-140	192,600	742,000	nd	nd	nd	10,800	0.9	-
15A-3H7-55-60	184,800	749,900	nd	nd	nd	19,600	1.6	-
15A-4H1-135-140	184,100	745,700	nd	2,500	0.2	46,500	3.7	0.1
15A-4H2-135-140	180,200	744,800	nd	29,900	2.4	51,200	4.2	0.6
15A-4H3-105-110	169,400	744,000	nd	63,900	5.2	42,600	3.5	1.5
15A-4H4-135-140	147,300	776,000	nd	102,600	8.4	39,300	3.2	2.6
15A-4H5-95-100	145,600	776,400	nd	94,200	7.7	36,200	3.0	2.6
15A-4H6-85-90	183,500	742,800	nd	16,300	1.4	24,400	2.1	0.7
15A-5H3-105-110	167,200	748,500	nd	52,000	4.3	66,700	5.6	0.8
15A-5H5-95-100	159,300	765,500	nd	55,000	4.6	78,100	6.5	0.7
15A-6H3-95-100	170,900	745,900	nd	29,200	2.5	138,300	11.7	0.2
15A-6H5-85-90	162,800	750,600	nd	32,900	2.8	128,400	11.0	0.3
15A-7H3-41-46	171,500	743,100	nd	22,400	1.9	114,700	9.9	0.2
15A-7H5-50-55	165,700	745,700	nd	26,600	2.3	116,800	10.2	0.2
15A-8H4-82-87	177,900	750,900	nd	22,300	2.0	94,200	8.2	0.2
15A-8H5-71-76	174,300	750,100	nd	30,500	2.7	86,800	7.6	0.4
15A-9X1-125-130	165,900	732,600	nd	26,300	2.5	46,900	4.4	0.6
15A-9X2-68-73	143,200	743,500	nd	30,000	2.7	102,000	9.3	0.3
15A-9X4-64-69	145,000	773,900	nd	15,800	1.4	73,200	6.6	0.2
15A-11Y-30-32	164,300	768,200	nd	1,200	0.1	32,700	3.0	0.0
15A-12X3-85-90	143,400	740,400	nd	22,900	2.1	212,800	19.5	0.1
15A-12X5-75-80	128,600	747,100	nd	16,900	1.6	131,300	12.1	0.1
15A-13X2-85-90	138,900	754,300	nd	17,900	1.7	70,500	6.6	0.3
15A-13X4-75-80	139,800	756,400	nd	21,400	2.0	152,200	14.1	0.1
15A-14X3-85-90	164,700	758,500	nd	5,300	0.5	25,600	2.5	0.2
15A-14X4-145-150	172,900	745,200	nd	5,000	0.5	33,100	3.1	0.1
15A-16Y-23-24	146,100	726,800	nd	8,600	0.8	55,900	5.4	0.2
15A-17X3-0-5	165,400	744,000	nd	9,200	0.9	34,000	3.2	0.3
15A-17X4-31-36	146,400	775,600	nd	15,000	1.4	95,900	9.2	0.2
15A-18X3-85-90	176,100	759,200	nd	4,800	0.5	18,200	1.8	0.3
15A-18X5-75-80	108,200	794,100	nd	8,000	0.9	27,200	2.9	0.3
15A-19X1-85-90	137,100	779,000	nd	12,600	1.2	34,200	3.3	0.4
15A-19X3-75-80	139,300	771,900	nd	14,900	1.4	55,100	5.2	0.3
15A-20X3-75-80	161,600	763,600	nd	12,100	1.2	32,200	3.1	0.4
15A-21X3-75-80	166,800	753,500	nd	20,300	2.0	68,900	6.7	0.3
15A-22X2-135-140	159,000	776,600	nd	13,900	1.4	57,000	5.5	0.2
15A-23X3-75-80	154,400	765,800	nd	34,000	3.4	52,900	5.2	0.6
15A-24X3-75-80	177,700	758,300	nd	23,200	2.3	29,400	2.9	0.8
15A-25X2-75-80	182,700	768,500	nd	18,700	1.8	31,500	3.1	0.6

Notes: nd = not detected. WS = Wet sediment. PW = porewater. Approximate detection limits are about 15 ppmv for methane, 30 ppmv for ethane, 50 ppmv for propane, and 20 ppmv for hydrogen sulfide.

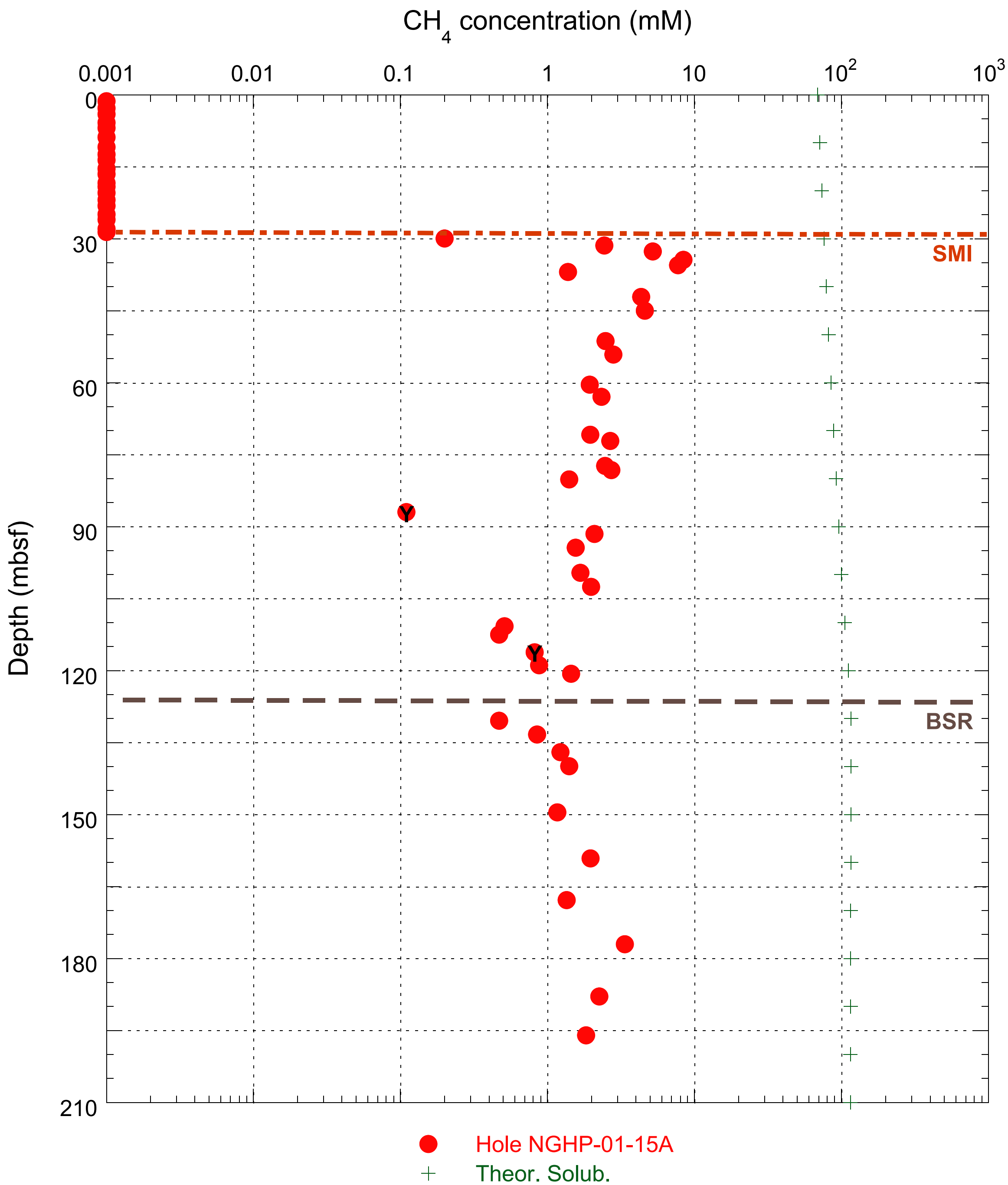

Figure 12. Plot of headspace methane gas concentration (mM) with depth for Hole NGHP-01-15A. Note the methane gradient at ~29 mbsf denoting the SMI. Values less than 0.003 mM are below instrument detection limits, but plotted for reference. Text inside a symbol denotes special coring tool (E, HRC; P, PCS; Y, FPC). Theoretical solubility of methane calculated using the Duan and others (1992) and Xu (2002, 2004) methodologies. [SMI, sulfate methane interface]

The results can be roughly divided into three zones based on CO_2 concentration. The lowest and declining (3.4 to 0.9) concentrations are found above the SMI at depths ranging from 0 to 30 mbsf (fig. 13). CO_2 concentrations ranging from 2.1 to 19.5 mM were found in the interval below the SMI. Below the BSR, CO_2 concentrations are generally low, ranging between 3 and 6 mM; however these concentrations are above surficial levels. The methane to carbon dioxide ratio did not reflect these zones. Instead, this ratio exhibits high magnitude intervals just below the SMI and near ~75 and 180 mbsf (fig. 14). A slight decreasing trend with depth indicated that methane may not be preferentially concentrated in relation to carbon dioxide between the SMI and BSR; although other proxy indicators did confirm the presence of gas hydrate in this borehole at ~80 mbsf and up to 25 percent porespace gas hydrate between 90 to 110 mbsf (see “Inorganic Geochemistry” and “Downhole Logging”). The air gases (N_2+Ar), and O_2 were the balance gases, however the (N_2+Ar)/O_2 ratios were typically greater than air reflecting the ratio in the pore water or indicating that some air was trapped in the headspace samples and some oxygen has likely dissolved preferentially compared to N_2. Air gases are present in all samples as the core plugs were degassed in an air headspace.

Void gas samples were collected from twelve different intervals ranging in depth from 38.9 to 180.2 mbsf. The void gas samples contained methane above 94 percent at all intervals, as noted in table 6. Methane concentrations within voids averaged nearly 971,000 ppm (± 10,500; 97.1 percent ± 1.05 percent). Carbon dioxide concentrations ranged from ~6,000 to 21,000 parts per million by volume (ppmv) and are tabulated with other gas data in table 6. The methane to carbon dioxide ratios were fairly uniform with increasing depth. This may indicate that any existing gas-hydrate formation has concentrated the methane relative to carbon dioxide in free gases with depth (fig. 14). Void gases exhibited the presence of low level C_2 concentrations, ranging from non-detectable to 132 ppmv. Ratio values for C_1 to C_2 gases ranged from ~7,300 to ~50,900 ppmv (average 28,660 ppmv), and showed the typical decreasing trend with depth (fig. 15). The concentrations are focused in the ‘normal’ occurrence range as depicted in the graph. The air gases (N_2+Ar), and O_2 composed the balance gases and reflect air contamination plus concentrations within the sediment.

Gas was collected from two pressure core sampler (PCS) intervals in Hole NGHP-01-15A. The gas concentration results are quite similar to the void gas results (tables 6 and 7); however C_1/CO_2 indicated slightly greater enrichment of methane in PCS gas results (fig. 14). Gas analysis of PCS samples from 86.7 mbsf demonstrated that methane from gas hydrate is present (see “Pressure Coring”). It should be noted that Cl^- values drop to 63 percent of modern seawater value at 79 mbsf, confirming the presence of concentrated gas hydrate within this depth interval (see “Inorganic Geochemistry”). Other visual and proxy measurements indicated presence of gas hydrate near this interval (see “Physical Properties” and “Downhole Logging”). Ratio values for C_1 to C_2 gases ranged from ~15,700 to ~25,400 ppmv, and showed the typical decreasing trend with depth (fig. 15). The concentrations are focused centrally in “normal” occurrence interval as depicted in the graph. These high methane concentrations versus low concentrations of ethane are strong evidence of a microbially dominated hydrocarbon gas source.

Microbiology

Hole NGHP-01-15A

Analysis of all microbiological samples will be shore-based. Twenty-one samples were collected for CEL, and 21 for SPH, one 30 cm section identified as anomalous on the IR scan of the score (MAF, MAG, MAA) for detailed microbiological studies and one 30 cm section identified as background (MBF, MBG, MBR) (table 8). The 30 cm sections were split into 3 subsections as described in the “Methods” chapter. Additional microbiological samples were taken (Lab code JUD, 34 samples; Lab code JAN, 22 samples). Samples were collected as described in the “Methods” chapter.

Physical Properties

Whole-round cores at NGHP Expedition 01, Site 15 were imaged using an IR camera on the catwalk to determine the location of temperature anomalies on the surface of core liners and enable sections containing potential gas hydrate to be quickly removed, preserved, and studied. After IR imaging was finished, non-destructive measurements were conducted on temperature-equilibrated whole-round core sections with the MSCL. Thermal conductivity measurements were also conducted on whole-round cores. Various tests were performed on split cores including: electrical resistivity by use of a Wenner array, *P*-wave velocity by inserted spades, and shear strength by mini-vane and Pocket Penetrometer. Core subsamples were placed in 10-mL beakers and dried at 105 °C to determine water content. Subsequently, the dried samples were analyzed for grain density using gas pycnometers and other sediment parameters were then calculated. See the “Physical Properties” section of the “Methods ” chapter for more details.

The physical properties program at Site NGHP-01-15 focused primarily on Hole NGHP-01-15A that was located about 36 km off the east coast of India within the KG Basin in about 930 m of water. Hole NGHP-01-15A was continuously cored to about 200 mbsf and had an overall core recovery of 85 percent. IR images indicated that gas hydrate was present from approximately 18 to 80 mbsf.

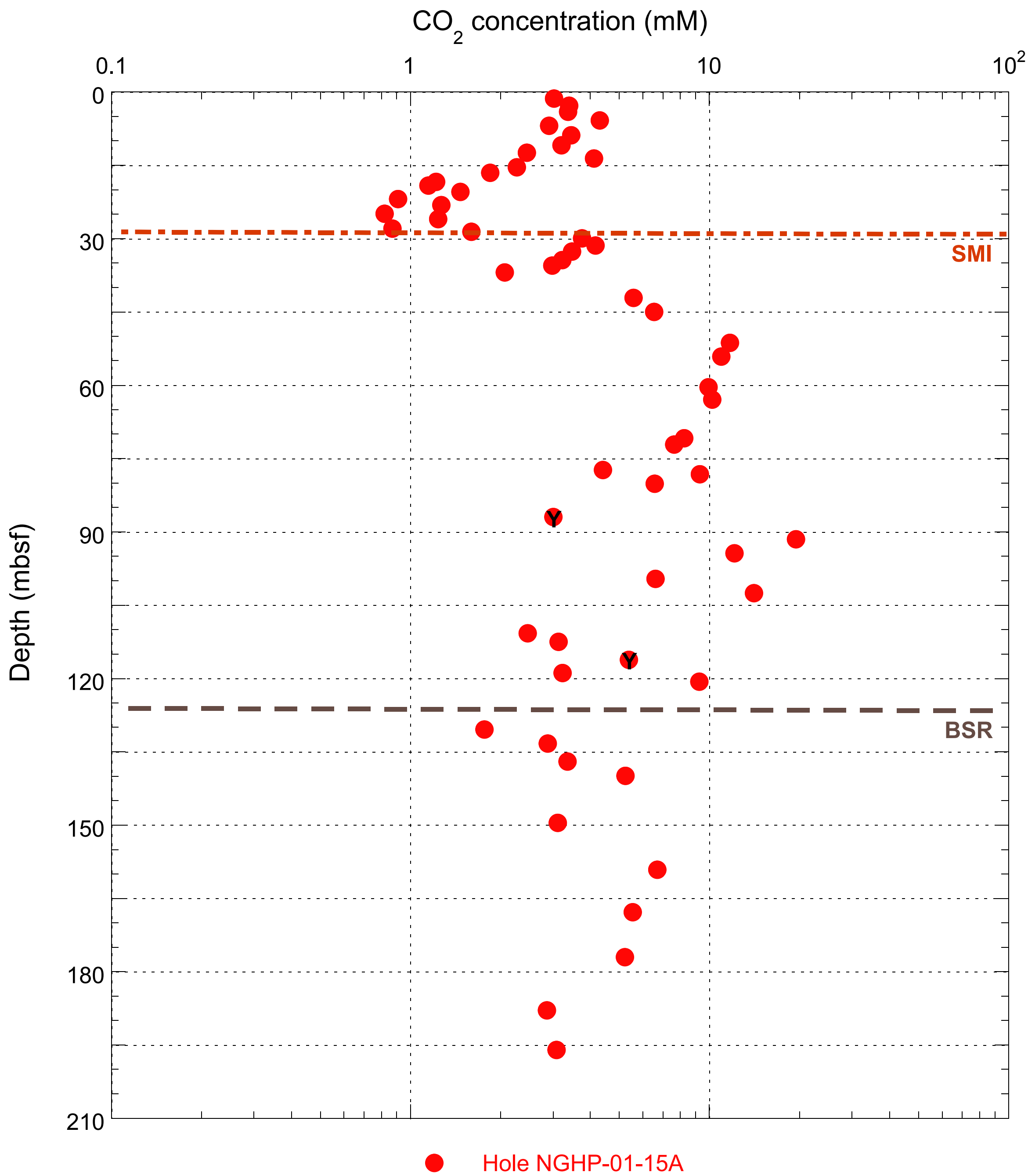

Figure 13. Plot of headspace carbon dioxide gas concentration (mM) with depth for Hole NGHP-01-15A. Text inside a symbol denotes special coring tool (E, HRC; P, PCS; Y, FPC).

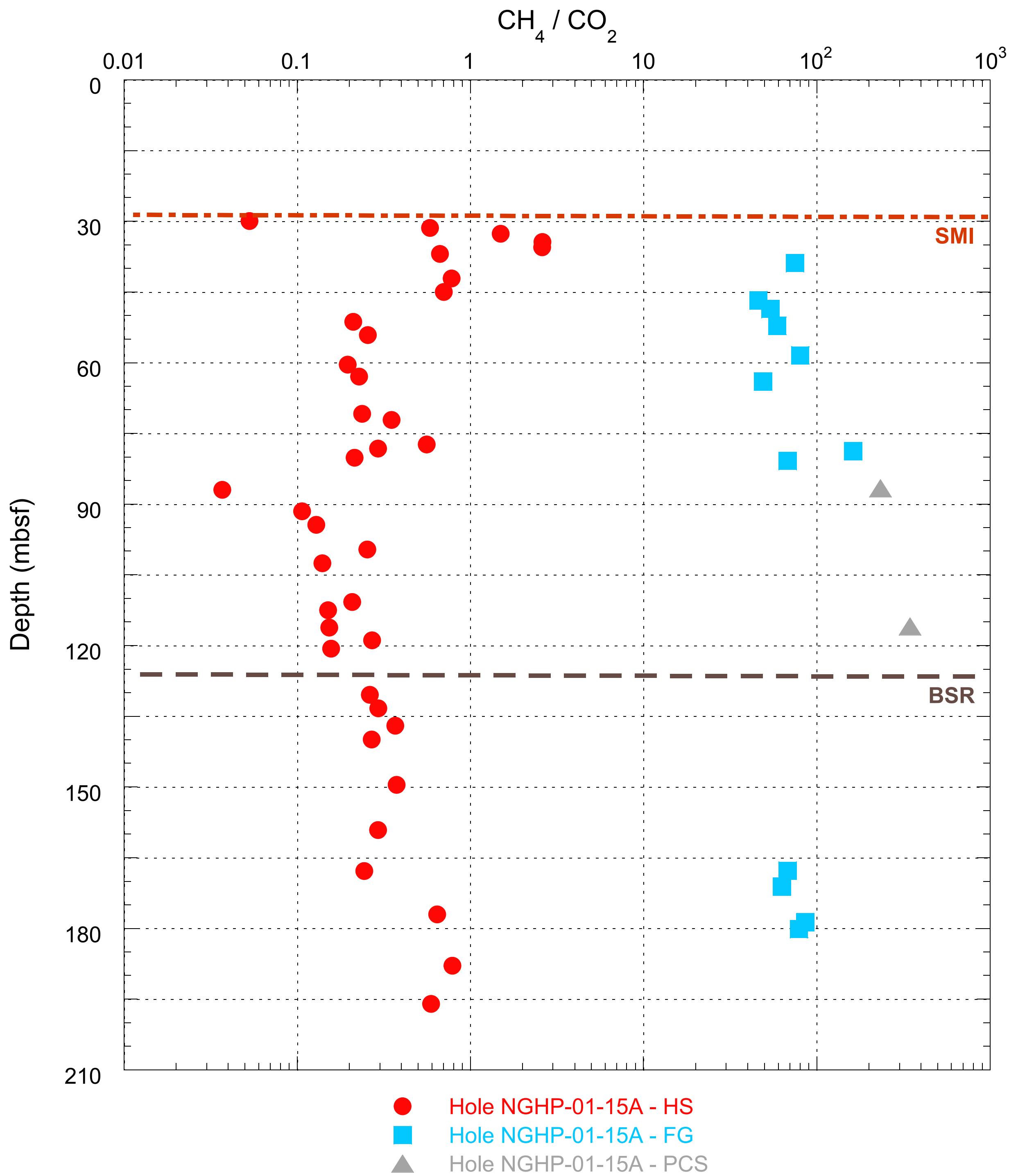

Figure 14. Plot of methane to carbon dioxide gas ratio with depth for headspace, free/void gas, and PCS gas for Hole NGHP-01-15A. Note the localized peaks in methane concentration, perhaps indicating the presence of free gas or gas hydrate. [PCS, Pressure Core Sampler]

Table 6. Void gas composition for Site NGHP-01-15.

Sample	Site	Hole	Core	Section	Interval (cm)	Sample depth (mbsf)	CO_2	C_1	C_2	C_3	O_2	N_2+Ar	H_2S	C_1/CO_2	C_1/C_2
							(ppmv) normalized to nitrogen+argon								
15A-5H1-78	15	A	5	1	78	38.88	12,600	944,600	20	nd	6,200	36,500	nd	70	47,200
15A-5H6-118	15	A	5	6	118	46.78	21,000	966,500	20	nd	2,400	10,100	nd	50	48,300
15A-6H1-99	15	A	6	1	99	48.59	18,100	968,500	20	nd	2,000	11,500	nd	50	48,400
15A-6H4-27	15	A	6	4	27	52.16	16,300	964,400	30	nd	2,200	17,000	nd	60	32,100
15A-7H1-138	15	A	7	1	138	58.48	12,200	972,900	20	nd	2,000	12,800	nd	80	48,600
15A-7H6-38	15	A	7	6	38	64	19,900	968,700	20	nd	1,600	9,700	nd	50	48,400
15A-9X2-118	15	A	9	2	118	78.78	6,000	968,300	80	nd	8,100	17,500	nd	160	12,100
15A-9X4-129	15	A	9	4	129	80.82	14,500	981,500	70	nd	1,500	2,400	nd	70	14,000
15A-22X2-131	15	A	22	2	131	167.81	14,300	970,200	130	nd	3,800	11,500	nd	70	7,500
15A-22X5-101	15	A	22	5	101	171.11	15,400	976,800	120	nd	1,600	6,100	nd	60	8,100
15A-23X4-92	15	A	23	4	92	178.73	11,400	983,300	120	nd	1,300	3,900	nd	90	8,200
15A-23X5-86	15	A	23	5	86	180.17	12,400	982,100	120	nd	1,200	4,100	nd	80	8,200

Notes: nd = not detected. nr = not recorded. Approximate detection limits are about 15 ppmv for methane, 30 ppmv for ethane, 50 ppmv for propane, and 20 ppmv for hydrogen sulfide.

Infrared Imaging

Environmental Conditions

The catwalk environment was monitored during the entire drilling operation at Site NGHP-01-15. Temperature on the catwalk remained relatively constant at ~30 °C, ranging from 28.5 to 32.5 °C during the drilling operation (fig. 16). Relative humidity ranged from 64 to 84 percent (fig. 16), which is consistent with a marine environment setting in the Indian Ocean. No adverse environmental conditions such as thunderstorms, rough seas, lightening, or high winds, persisted during drilling operations at this site.

Infrared Images

All APC and XCB cores from Site NGHP-01-15 were systematically scanned upon arrival on the catwalk using the track-mounted IR camera described in the “Physical Properties” section of the “Methods” chapter. IR anomalies, commonly referred to as “cold spots,” indicate gas-hydrate dissociation during core recovery, which subsequently provides guidance to catwalk sampling. Summary digital maps of the scans of all cores are available on the data DVD that accompanies this report and listings of the image files are presented in tables 9 and 10. Temperature arrays in text-formatted files were exported from the IR camera software and then concatenated for each core. The arrays were then further concatenated for all cores available in a given borehole. Downcore temperatures were averaged for each pixel row in the array, excluding pixels ~1 cm from the edge of the image and 2 cm along the midline of the image. Exclusion of these pixels minimized the effects caused by major thermal artifacts in the images. This processing enabled us to measure the average amplitude of the cold anomalies and identify warm anomalies due to voids from the background temperature field.

Infrared track imaging at Hole NGHP-01-15A consisted of 23 scans for a total scanned core length of approximately 150 m. The complete set of IR images collected for Hole NGHP-01-15A is presented in figure 17 along with the corresponding downcore temperatures. The median core temperature extracted from the IR images for Hole NGHP-01-15A ranged from a high of ~30 °C on core liner bottom ends near the deepest portion of the hole, to a low of 15 °C (~78 mbsf). As shown in figure 17, significant IR anomalies occurred in two places in Hole NGHP-01-15A. The shallowest gas-hydrate-bearing sediment appeared in Core NGHP-01-15A-01H (~18 mbsf) and the deepest gas-hydrate-bearing sediment appeared in Core NGHP-01-15A-09X, at an approximate depth of 80 mbsf. This correlates with a gas-hydrate occurrence and hydrate saturation calculated from the resistivity log (see “Downhole Logging”). Specifically, the hydrate saturation peaks at exactly the same depth as the IR anomaly (fig. 37). Temperatures extracted from thermal images show that the DT for this zone is large, with a value of about 6.4 °C.

Furthermore, this depth in hole also contains sandy layers based on the density and gamma ray logs as well as index properties.

IR images of the ends of core sections were acquired with a hand-held IR camera on the catwalk during sampling activities when possible. Forty-four core-end IR images were collected from Hole NGHP-01-15A. Figure 18 shows a typical section-end IR image from Section NGHP-01-15A-09X-4 (bottom). The relatively warm interior temperature at the center of this profile suggest that gas hydrate may have contributed to the thermal structure of this core.

However, no individual lenses of gas hydrate are apparent at this point in the core.

In addition to the IR core-end images, a hand-held camera was used to identify cold anomalies in the sediment selected for interstitial water samples. Whole-round samples were removed from the core and taken to the chemical laboratory for extrusion from the core liner and immediate interstitial water sampling. After extruding the sediment from the liner, IR imaging with a hand-held camera was used to identify gas hydrate or “cold spots” in the sediment and provide guidance for detailed sediment sampling. An example of a core liner IR anomaly with its extruded sediment is shown in figure 19. A sand lens in the same position of the IR anomaly is clearly visible.

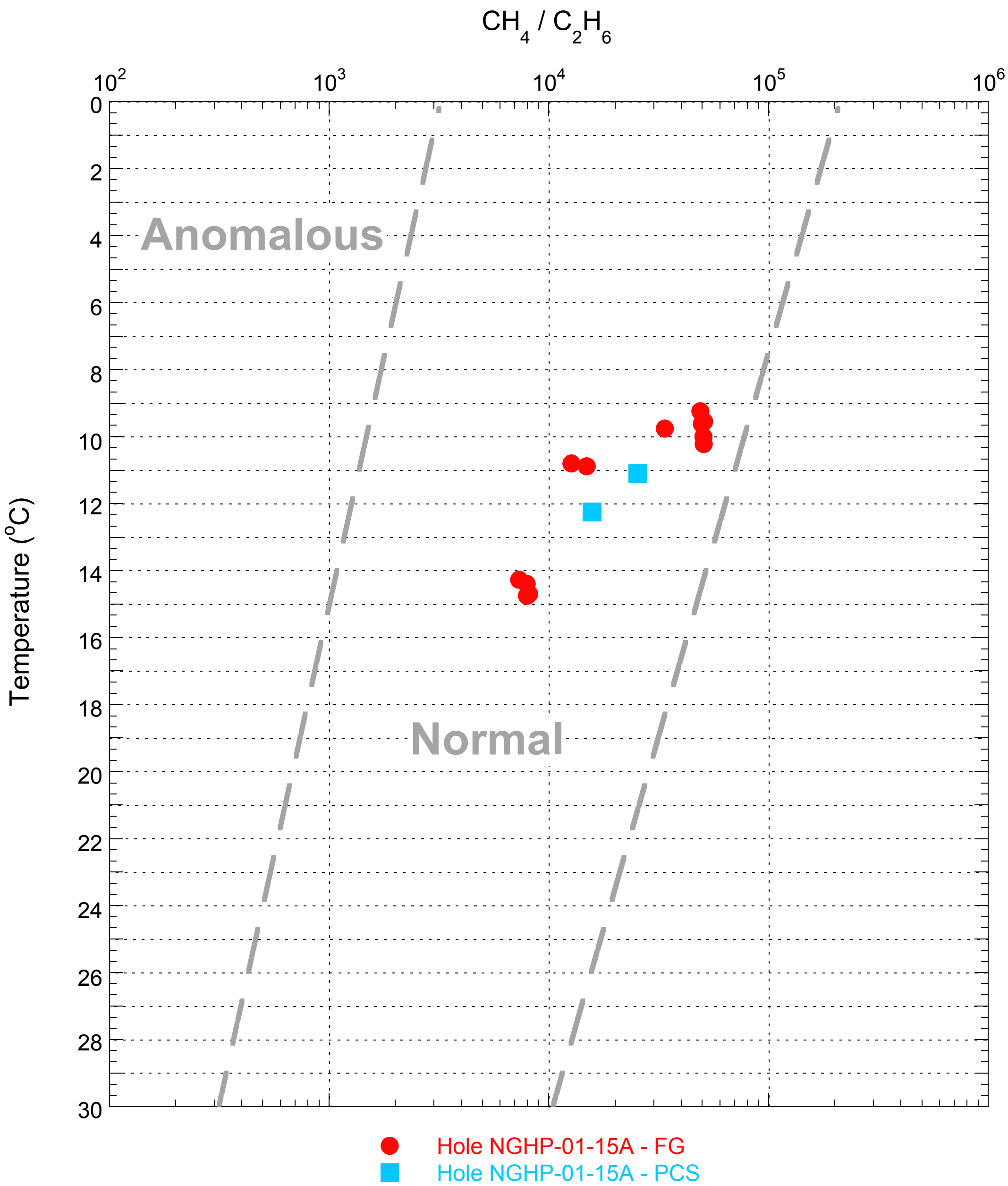

Figure 15. Plot of free/void gas and PCS methane to ethane gas ratio with depth for Hole NGHP-01-15A. Ethane levels were below detection limits for all headspace and PCS samples (tables 5 and 7). Note that the hydrocarbon gas occurrences fall into the typical range. [PCS, Pressure Core sampler]

Table 7. Pressure Core Sampler gas composition for Site NGHP-01-15.

Sample	Site	Hole	Core	Section	Sample depth (mbsf)	Time	Gas vol. (ml)	CO_2	C_1	C_2	C_3	O_2	N_2+Ar	H_2S	C_1/CO_2	C_1/C_2
								(ppmv) normalized to nitrogen+argon								
15A-11Y-t1	15	A	11	Y	86.7	1	-	3,400	969,500	40	nd	4,200	22,900	nd	300	24,200
15A-11Y-t2	15	A	11	Y	86.7	2	-	2,000	368,400	nd	nd	261,100	368,400	nd	200	-
15A-16Y-t1	15	A	16	Y	116	1	-	2,300	788,500	50	nd	35,400	173,700	nd	300	15,800

Notes: nd = not detected. Approximate detection limits are about 15 ppmv for methane, 30 ppmv for ethane, 50 ppmv for propane, and 20 ppmv for hydrogen sulfide.

Table 8. List of microbiological samples taken for Site NGHP-01-15.

Sample reference						Comments	Sample reference						Comments
Core, section	Sample code	Top (cm)	Bottom (cm)	Depth (mbsf)	Volume (cc)		Core, section	Sample code	Top (cm)	Bottom (cm)	Depth (mbsf)	Volume (cc)	
						NGHP-01-15A							
1H-5	CEL	95	100	6.95	5		5H-5	JUD	120	130	45.3	374	
2H-5	CEL	95	100	16.55	5		6H-3	JUD	110	120	51.49	374	
3H-5	CEL	95	100	26.05	5		6H-5	JUD	110	120	54.4	374	
4H-5	CEL	95	100	35.55	5		7H-3	JUD	56	66	60.57	374	
5H-5	CEL	95	100	45.05	5		7H-5	JUD	75	85	63.22	374	
6H-5	CEL	85	90	54.15	5		8H-4	JUD	97	107	71.03	374	
7H-5	CEL	50	55	62.97	5		8H-5	JUD	99	109	72.42	374	
8H-5	CEL	71	76	72.14	5		9X-4	JUD	89	99	80.42	374	
9X-4	CEL	64	69	80.17	62	WR TAKEN	12X-3	JUD	100	110	91.7	374	
12X-5	CEL	75	80	94.45	5		12X-5	JUD	100	110	94.7	374	
13X-4	CEL	75	80	102.55	5		13X-2	JUD	100	110	99.8	374	
14X-4	CEL	110	115	112.5	5		13X-4	JUD	100	110	102.8	374	
17X-3	CEL	0	5	118.89	5		14X-3	JUD	100	110	110.9	374	
18X-5	CEL	75	80	133.35	5		14X-5	JUD	20	30	112.75	374	
19X-3	CEL	75	80	139.95	5		17X-2	JUD	100	110	118.39	374	
20X-3	CEL	75	80	149.55	5		18X-3	JUD	100	110	130.6	374	
21X-3	CEL	75	80	159.15	5		18X-5	JUD	100	110	133.6	374	
22X-2	CEL	135	140	167.85	5		19X-1	JUD	100	110	137.2	374	
23X-3	CEL	75	80	177.06	5		19X-3	JUD	100	110	140.2	187	
24X-3	CEL	75	80	187.95	5		20X-3	JUD	100	110	149.8	374	
25X-2	CEL	75	80	196.05	5		21X-3	JUD	100	110	159.4	374	
1H-5	JAN	105	110	7.05	187		22X-3	JUD	20	30	168.1	374	
2H-5	JAN	105	110	16.65	187		23X-3	JUD	100	110	177.31	374	
3H-5	JAN	105	110	26.15	187		24X-3	JUD	100	110	188.2	374	
4H-5	JAN	105	110	35.65	187		25X-2	JUD	100	110	196.3	374	
5H-5	JAN	105	110	45.15	187		9X-2	MAF	83	93	78.43	374	
6H-5	JAN	95	100	54.25	187		9X-2	MAG	93	102	78.53	337	
7H-5	JAN	60	65	63.07	187		9X-2	MAR	73	83	78.33	374	
8H-5	JAN	81	86	72.24	187		12X-4	MBF	130	140	93.5	374	
9X-2	JAN	102	103	78.62	37		12X-4	MBG	140	150	93.6	374	
9X-4	JAN	74	79	80.27	187		12X-4	MBR	120	130	93.4	374	
12X-5	JAN	85	90	94.55	187		1H-5	SPH	100	105	7	187	
13X-4	JAN	85	90	102.65	187		2H-5	SPH	100	105	16.6	187	
14X-5	JAN	5	10	112.6	187		3H-5	SPH	100	105	26.1	187	
17X-2	JAN	85	90	118.24	187		4H-5	SPH	100	105	35.6	187	
18X-5	JAN	85	90	133.45	187		5H-5	SPH	100	105	45.1	187	
19X-3	JAN	85	90	140.05	187		6H-5	SPH	90	95	54.2	187	
20X-3	JAN	85	90	149.65	187		7H-5	SPH	55	60	63.02	187	
21X-3	JAN	85	90	159.25	187		8H-5	SPH	76	81	72.19	187	
22X-3	JAN	5	10	167.95	187		9X-4	SPH	69	74	80.22	187	
23X-3	JAN	85	90	177.16	187		12X-5	SPH	80	85	94.5	187	
24X-3	JAN	85	90	188.05	187		13X-4	SPH	80	85	102.6	187	
25X-2	JAN	85	90	196.15	187		14X-5	SPH	0	5	112.55	187	
1H-3	JUD	120	130	4.2	374		17X-2	SPH	80	85	118.19	187	
1H-5	JUD	120	130	7.2	374		18X-5	SPH	80	85	133.4	187	
2H-3	JUD	120	130	13.8	374		19X-3	SPH	80	85	140	187	
2H-5	JUD	120	130	16.8	374		20X-3	SPH	80	85	149.6	187	
3H-3	JUD	120	130	23.3	374		21X-3	SPH	80	85	159.2	187	
3H-5	JUD	120	130	26.3	374		22X-3	SPH	0	5	167.9	187	
4H-3	JUD	120	130	32.8	374		23X-3	SPH	80	85	177.11	187	
4H-5	JUD	120	130	35.8	374		24X-3	SPH	80	85	188	187	
5H-3	JUD	120	130	42.3	374		25X-2	SPH	80	85	196.1	187	

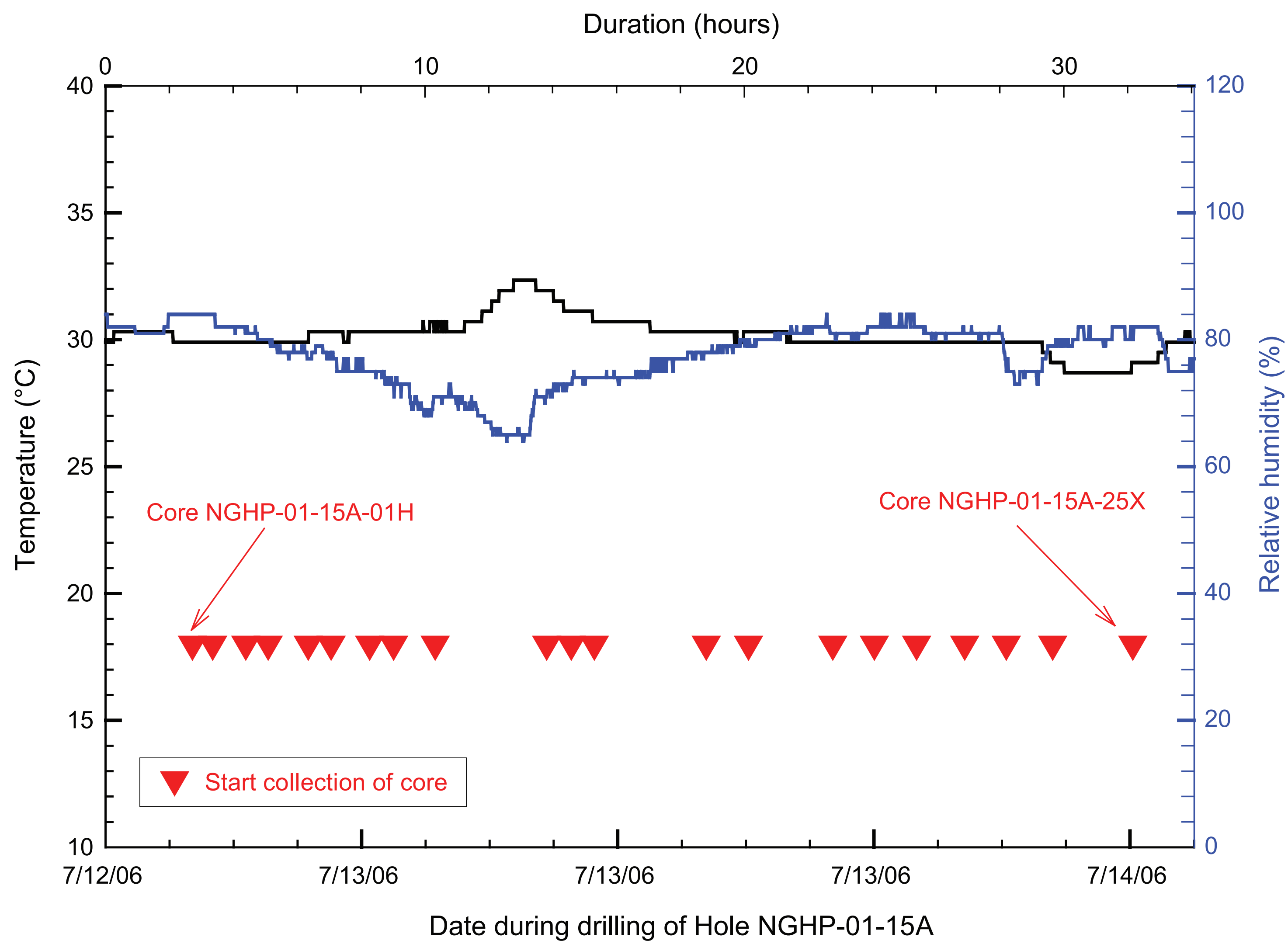

Figure 16. Catwalk temperature and humidity measurements as a function of time during drilling operations at Site NGHP-01-15.

Table 9. List of infrared image files collected from Hole NGHP-01-15A.

Core	Imaging length (cm)	First run	Date	Start time	Temperature (start/end) (°C)	Comments*
1H	940	x	7/13	1:43	29.9/29.9	15–30 °C
2H	970	x	7/13	2:21	29.9/29.9	15–30 °C
3H	970	x	7/13	3:23	29.9/29.9	15–30 °C
4H	950	x	7/13	4:05	29.9/29.9	15–30 °C
5H	960	x	7/13	5:20	29.9/29.9	15–30 °C
6H	970	x	7/13	6:03	30.3/30.3	15–30 °C
7H	820	x	7/13	7:15	30.3/30.3	15–30 °C
8H	910	x	7/13	8:00	30.3/30.3	15–30 °C
9X	560	x	7/13	9:18	30.3/30.3	15–30 °C
12X	880	x	7/13	12:47	32.3/32.3	15–30 °C
13X	680	x	7/13	13:33	31.5/31.5	15–30 °C
14X	860	x	7/13	14:16	31.1/31.1	15–30 °C
17X	370	x	7/13	17:46	30.3/30.3	15–30 °C
18X	780	x	7/13	19:05	30.3/30.3	15–30 °C
19X	525	x	7/13	21:43	29.9/29.9	15–30 °C
20X	700	x	7/13	23:01	29.9/29.9	15–30 °C
21X	940	x	7/14	0:20	29.9/29.9	15–30 °C
22X	830	x	7/14	1:50	29.9/29.9	15–30 °C
23X	950	x	7/14	3:08	29.9/29.9	15–30 °C
24X	950	x	7/14	4:35	29.9/29.9	15–30 °C
25X	410	x	7/14	7:05	28.7/28.7	15–30 °C

*Temperature range for images displayed during core collection.

Core-End Temperature Readings

Core-end temperature readings were taken on all cores immediately following the IR track imaging. Typically four temperature probes were inserted approximately 8 cm into the end of each core and allowed to remain there until the core was completely processed and removed from the catwalk. A summary of the core-end temperature results for cores from Hole NGHP-01-15A are presented in table 11 and figure 20. Temperatures from the center position probes are plotted versus depth and compared to same-depth IR temperature of the core liner. As expected, center probe temperatures are 5 to 10 °C less than the IR temperatures because the IR images measure the liner temperature, which has warmed closer to ambient temperatures than the center of the core, except where significant gas hydrate is present. Exceptions occur at 125, 135, and 195 mbsf in which probe temperature are equal or higher than IR temperatures, possibly due to longer equilibration times for those measurements.

Index Properties

Water content, porosity, bulk density, grain density, and magnetic susceptibility vary downhole such that three physical-property units can be defined with boundaries at 80 and 133 mbsf (figs. 21 and 22). The change in behavior agrees with the Lithostratigraphic description at this site that shows nannofossil-rich clay in the middle section separating clay in the upper section from nannofossil-bearing clay and clay in the bottom section (see "Lithostratigraphy"). This overall trend in property changes is also reflected in the wire-line logs.

The water content (related to solids) in the uppermost part of the core (88 percent) is lower than at previous sites (table 12). Furthermore, the rate of decrease with depth is also less. Porosity varies from 70 percent to 43 percent downhole. Except for an offset between 135 and 155 mbsf, bulk density data from wire-line logging are in close agreement with either MAD or MSCL values continuously downhole (fig. 21). Grain density varies from 2.33 to 2.77 g/cm^3 with an average value of 2.70 g/cm^3. The 2.33 g/cm^3 grain density value was from a woody sand recovered in a Fugro Pressure Core (FPC; NGHP-01-15A-11Y at 86.85 mbsf). This sand was more organic-rich and finer grained than a thinner layer of gas-hydrate-bearing sand in the center of the FPC.

Strength

Shear strength increased uniformly and linearly with depth to 30 mbsf then increased to the bottom of the hole but with more variation below that depth (tables 13 and 14; fig. 21). The boundary between APC and XCB coring is about 75 mbsf. Below that depth, slightly more variation exists, illustrating the effect of disturbance caused by rotary coring on sediment. Although testing was to be restricted to intact biscuits, it was occasionally difficult to differentiate between biscuits and adjacent disturbed sediment.

Table 10. List of infrared image files collected on section ends from Hole NGHP-01-15A.

Core	Section	Top	Bottom	Date	Time	Image #	Comments
1H	3	x		7/13	7:37	1	
1H	3	x		7/13	7:37	2	
2H	3	x		7/13	8:30	3	
2H	3	x		7/13	8:30	4	
3H	3	x		7/13	9:35	5	
3H	3	x		7/13	9:35	6	
4H	3	x		7/13	4:20	7	
4H	3	x		7/13	4:20	8	
5H	3	x		7/13	5:38	9	
5H	3	x		7/13	5:38	10	
6H	3	x		7/13	6:30	11	
6H	3	x		7/13	6:30	12	
7H	3	x		7/13	7:37	13	
7H	3	x		7/13	7:37	14	
8H	3	x		7/13	8:30	15	
8H	3	x		7/13	8:30	16	
9X	4	x		7/13	9:35	17	
9X	4	x		7/13	9:35	18	
12X	2		x	7/13	12:59	19	
12X	2		x	7/13	12:59	20	
13X	2		x	7/13	13:45	21	
13X	2		x	7/13	13:45	22	
14X	3	x		7/13	14:29	23	
14X	3	x		7/13	14:29	24	
17X	3	x		7/13	17:54	25	
17X	3	x		7/13	17:54	26	
18X	2	x		7/13	19:12	27	
18X	2	x		7/13	19:12	28	
19X	2	x		7/13	21:56	29	
19X	2	x		7/13	21:56	30	
20X	2	x		7/13	23:08	31	
20X	2	x		7/13	23:08	32	
20X	2	x		7/13	23:09	33	
20X	2	x		7/13	23:09	34	
21X	2	x		7/14	0:30	1	
21X	2	x		7/14	0:30	2	
22X	2	x		7/14	2:06	3	
22X	2	x		7/14	2:06	4	
23X	2	x		7/14	3:25	5	
23X	2	x		7/14	3:25	6	
24X	2	x		7/14	4:50	7	
24X	2	x		7/14	4:50	8	
25X	2	x		7/14	7:13	9	
25X	2	x		7/14	7:13	10	

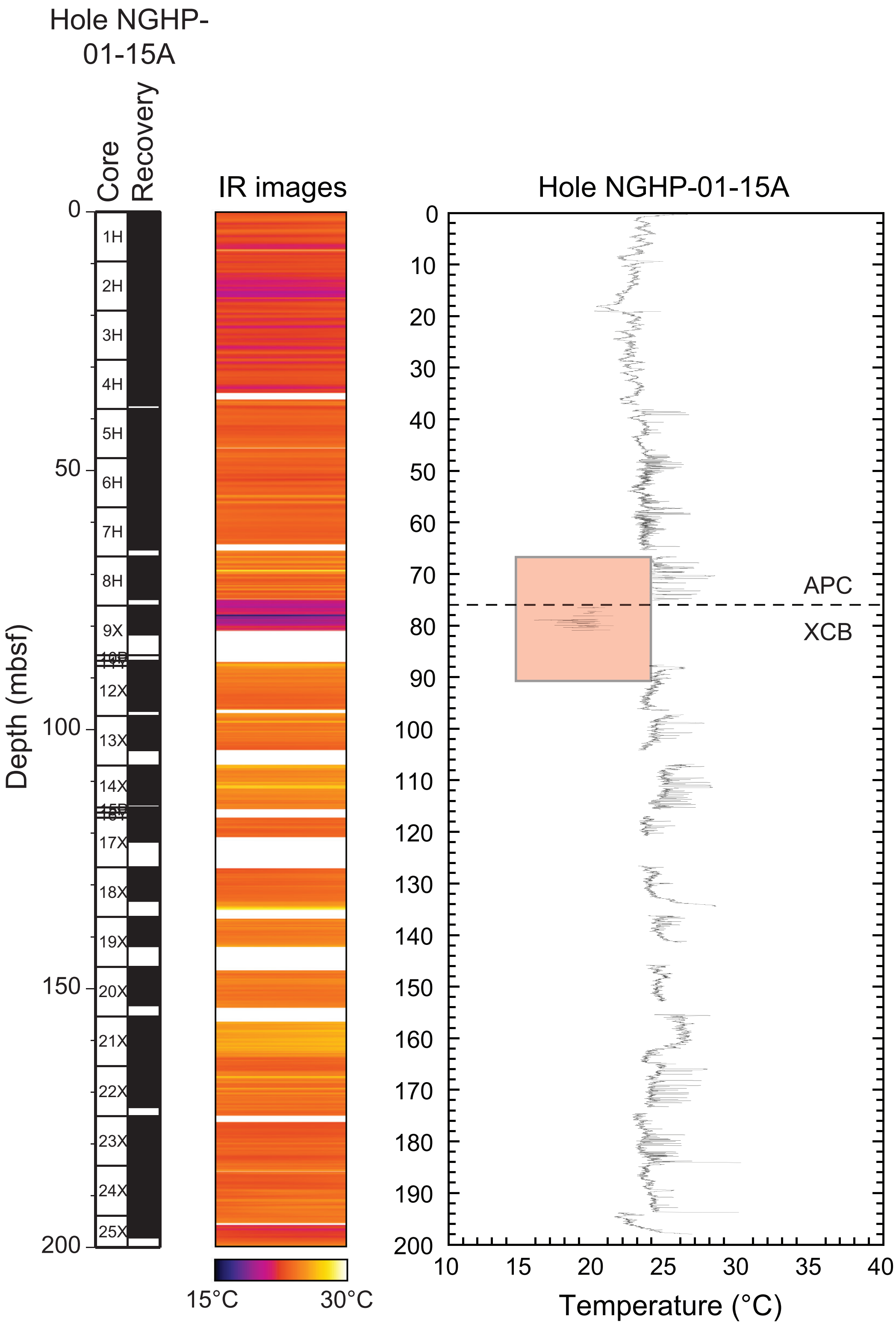

Figure 17. Infrared imaging and the derived downhole temperature profile for Hole NGHP-01-15A.

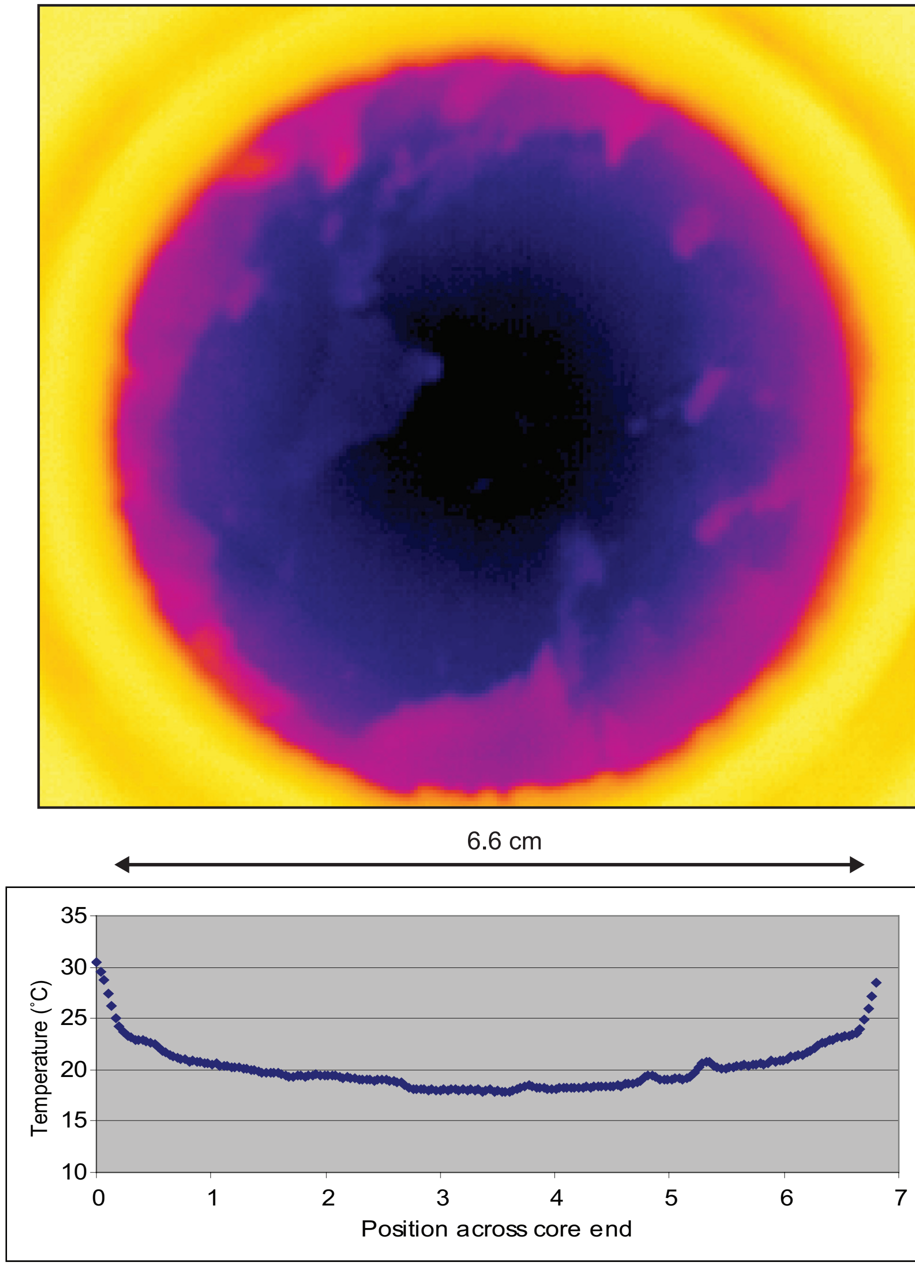

Figure 18. Selected downhole temperature from infrared imaging compared to same-depth center probe temperature measurements for Hole NGHP-01-15A.

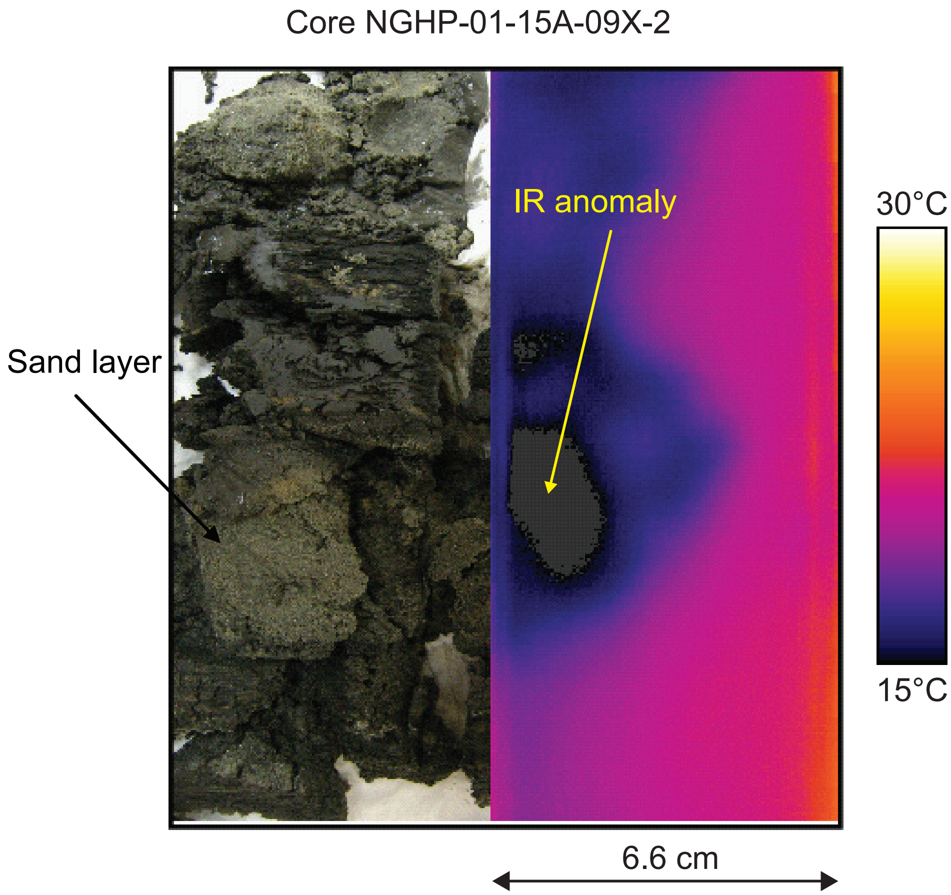

Figure 19. Core-end infrared image of Section NGHP-01-15A-09X-2, right side, with the corresponding reference temperature scale.

Table 11. List of temperature probe data collected at bottom of cores from Hole NGHP-01-15A.

Core	Section	Bottom	Date	In time	Out time	Temperature probe #	Comments
1H	last	x	7/13	1:45	1:58	1, 2, 3, 4	
2H	last	x	7/13	2:22	2:35	1, 2, 3, 4	
3H	last	x	7/13	3:25	3:35	1, 2, 3, 4	
4H	last	x	7/13	4:06	4:19	1, 2, 3, 4	
5H	last	x	7/13	5:21	5:37	1, 2, 3, 4	
6H	last	x	7/13	6:05	6:24	1, 2, 3, 4	
7H	last	x	7/13	7:15	7:37	1, 2, 3, 4	
8H	last	x	7/13	8:00	8:27	1, 2, 3, 4	
9X	last	x	7/13	9:18	9:38	1, 2, 3, 4	
12X	last	x	7/13	12:40	13:00	1, 2, 3, 4	
13X	last	x	7/13	13:34	13:45	1, 2, 3, 4	Hydrate
14X	last	x	7/13	14:18	14:32	1, 2, 3, 4	
17X	last	x	7/13	17:48	17:53	1, 2, 3, 4	
18X	last	x	7/13	19:07	19:14	1, 2, 3, 4	
19X	last	x	7/13	21:49	21:57	1, 2, 3, 4	
20X	last	x	7/13	23:03	NA	1, 2, 3, 4	
21X	last	x	7/14	0:20	0:30	1, 2, 3, 4	
22X	last	x	7/14	1:58	2:07	1, 2, 3, 4	
23X	last	x	7/14	3:10	3:25	1, 2, 3, 4	
24X	last	x	7/14	4:36	4:48	1, 2, 3, 4	
25X	last	x	7/14	7:05	7:12	1, 2, 3, 4	

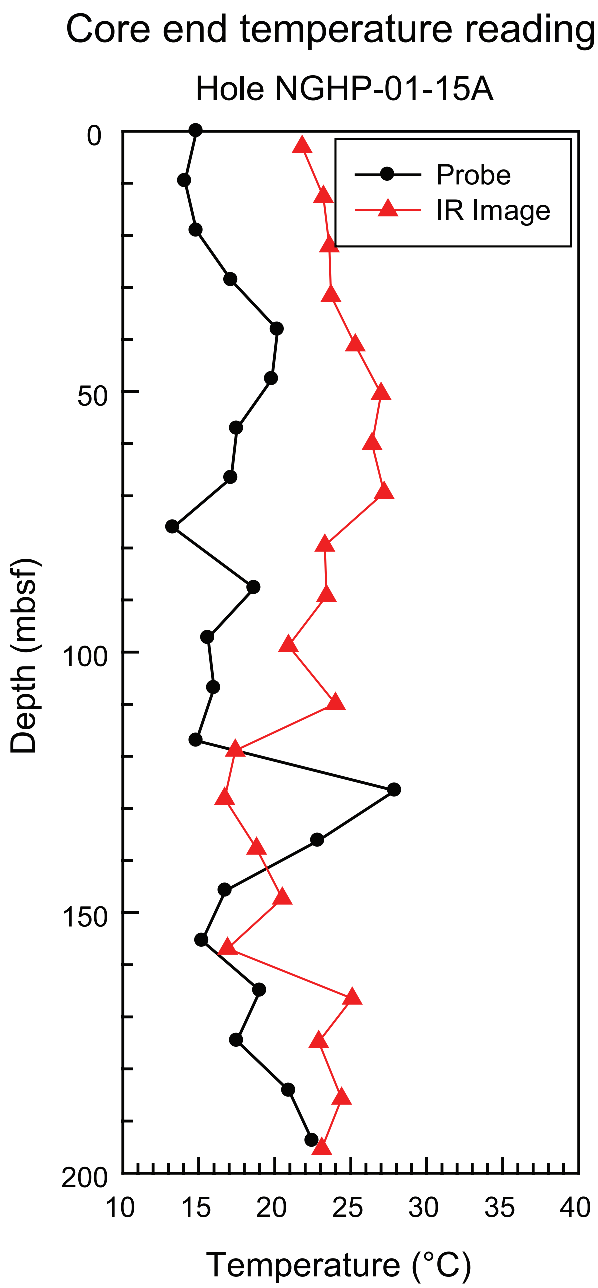

Figure 20. Core-end temperature measurements for Hole NGHP-01-15A.

The measured shear strengths were normalized to the effective vertical stress (σ'_v) (fig. 23) to provide qualitative information on the stress history of the sediment. The strength/effective vertical stress ranges from approximately 1.1 at the top of the hole to an average of about 0.1 near the bottom of the hole. Most of these values are in overall agreement with a number of other normally consolidated clays (Holtz and Kovacs, 1981). Hunt (1984) states that the strength/effective vertical stress ratio typically is between 0.4 and 0.16. The wide scatter in the results at the top of the hole reflect the dependency of this ratio on the stress path as well as the test method (Bjerrum, 1972; Ladd and others, 1977). Because eight values at the top of the hole are greater than 0.4, the implication is that the sediment at this location is slightly overconsolidated, probably due to removal of overburden. This agrees with the lower water content at the top of the hole compared with the other sites.

The peak (Sv) and remolded (Srem) vane shear strengths clearly increase with subbottom depth (fig. 24) and the sensitivity (St), which equals Sv/Srem, typically varies between 2.5 and 3. Sensitivity values represent the amount of strength loss after remolding and in extreme examples can reach values of 500 (Lambe and Whitman,1969). This sediment has low sensitivity (Holtz and Kovacs, 1981). High values of sensitivity are indicative of good quality core recovery because the sediment has not been highly disturbed.

Electrical Resistivity

Electrical resistivity values produced by wire-line logging, MSCL, and Wenner array all agree quite well below about 58 mbsf. Above this depth, hole conditions prohibited reliable wire-line logging. The resistivity values determined using the Wenner array on split cores are offset below the wire-line log values (fig. 22), in part because the Wenner measurements are conducted on intact core material, rather than a wider portion of core that may contain voids or small expansion cracks. Lower MSCL values are more representative of undisturbed sediment as they are less impacted by the presence of such micro voids caused by gas expansion.

Unlike other holes, for example, Hole NGHP-01-10B, the low wire-line resistivity values do not reflect exceptionally high zones of gas-hydrate concentration in Hole NGHP-01-15A. Resistivity determined using both MSCL and the Wenner array on split cores (table 15) increase near 31.5 mbsf, the approximate depth of the SMI. A possible explanation for this agreement is that methane is produced below the SMI and this gas expands upon core recovery disrupting the sediment structure.

The apparent formation factor is the ratio of the resistivity of a saturated sediment to the resistivity of the pore fluid and provides an indication of the relationships between sediment structure, void space, tortuosity, and other factors, and the ability of fluid to flow through the formation. Because pore water salinity typically varies a small amount in the recovered sediment and is similar to that of seawater (see "Inorganic Geochemistry"), we have normalized the measured Wenner resistivity values by that of seawater (approximately 0.2 Ω-m; table 15). Values range from about 2.0 at the top of the core to 7.0 at the bottom, with a spike between 76 and 87 mbsf (fig. 25). The spike is related to the presence of coarser-grained sediment. Other equations and methods exist for calculating formation factor; however, they require the use of empirical constants that have not yet been determined for the sediments at this location.

The presence of biscuits in XCB cores was assessed by continually inserting the electrodes of the Wenner array into the core between the depths of 137.85 and 137.94 mbsf. An observable trend between biscuits and infilling was not observed.

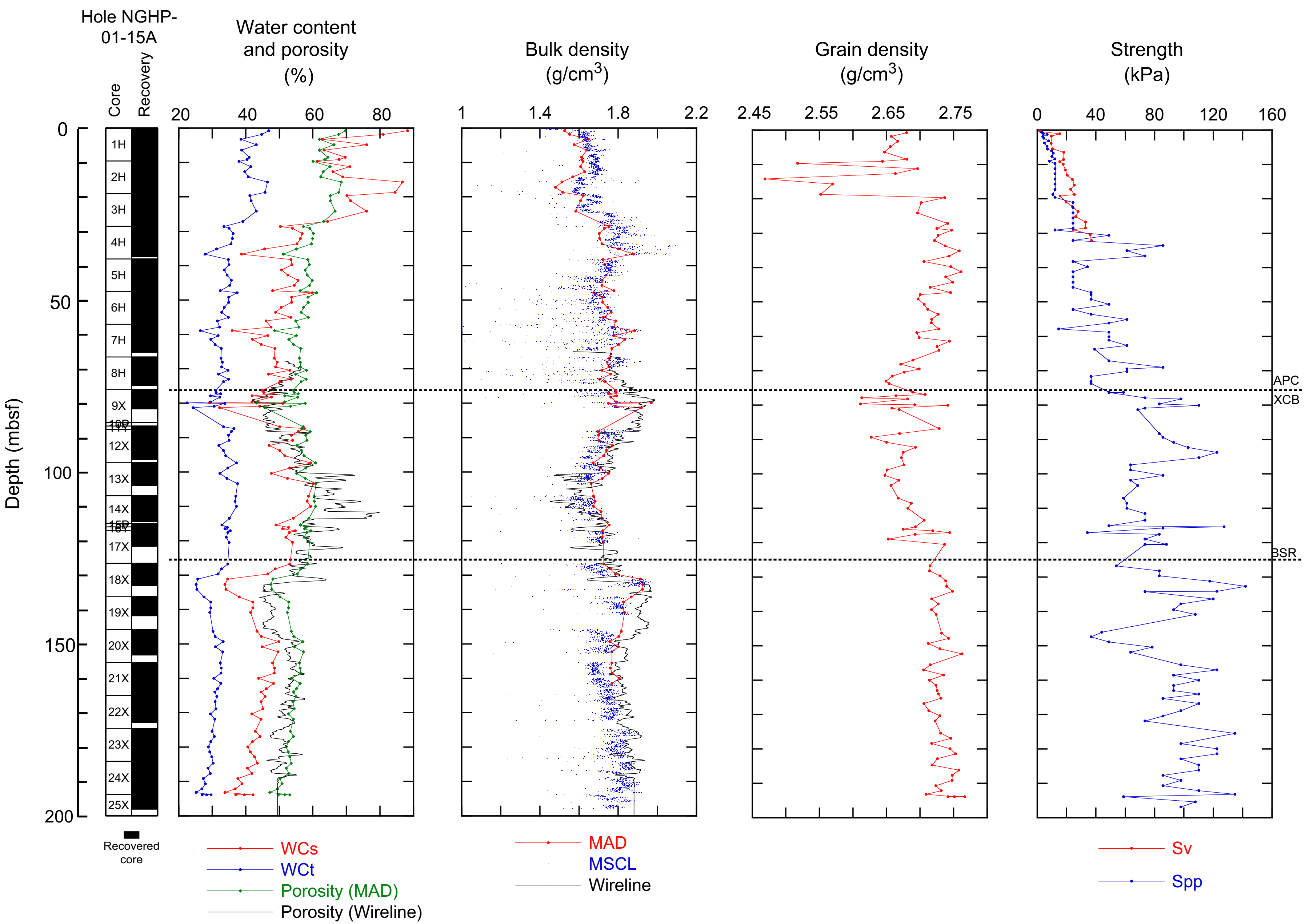

Figure 21. Profiles of core recovery, index, and strength properties for Hole NGHP-01-15A.

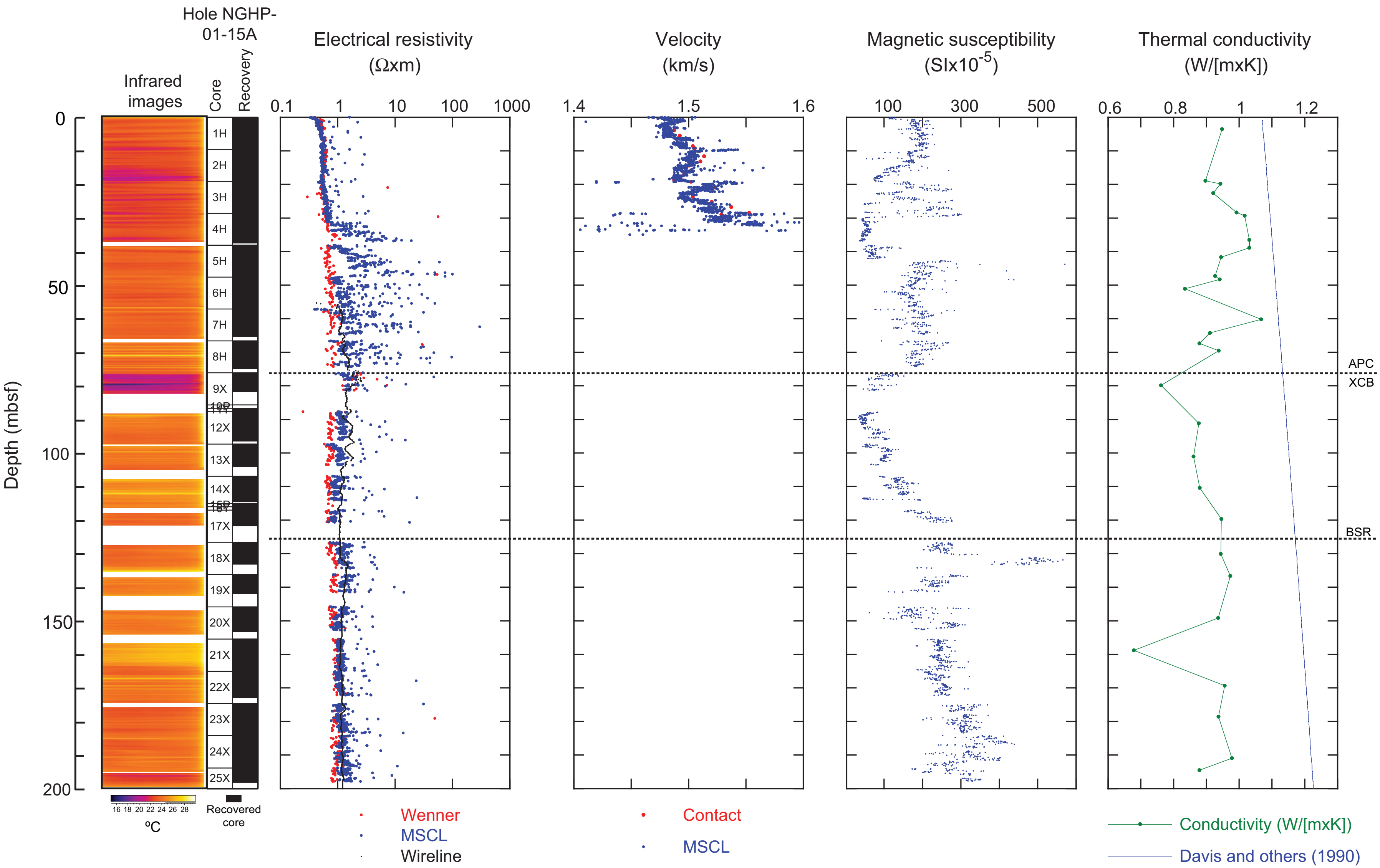

Figure 22. Profiles of infrared images, core recovery, electrical resistivity, acoustic *P*-wave velocity, magnetic susceptibility, and thermal conductivity for Hole NGHP-01-15A.

Table 12. Moisture and density (MAD) physical properties for Hole NGHP-01-15A.

Core, Section	Sample code	Depth, int, from (cm)	Depth, int, to (cm)	Depth (mbsf)	WCt (%)	WCs (%)	Grain density (g/cm³)	Bulk density (g/cm³)	Dry bulk density (g/cm³)	Porosity (%)	Void Ratio	Unit weight (kN/m³)
NGHP-01-15A												
1H-1	MAD	78	80	0.78	46.88	88.25	2.68	1.53	0.81	69.75	2.31	14.97
1H-2	MAD	36	38	1.86	44.75	81.01	2.66	1.55	0.86	67.72	2.10	15.22
1H-3	MAD	30	32	3.30	38.60	62.87	2.67	1.65	1.01	62.04	1.63	16.17
1H-4	MAD	36	38	4.86	43.19	76.04	2.66	1.58	0.89	66.31	1.97	15.45
1H-5	MAD	43	45	6.43	38.79	63.38	2.65	1.64	1.00	62.02	1.63	16.08
1H-6	MAD	102	104	8.52	41.06	69.68	2.68	1.61	0.95	64.54	1.82	15.81
1H-7	MAD	13	15	9.13	40.42	67.84	2.64	1.61	0.96	63.61	1.75	15.83
2H-1	MAD	12	14	9.72	38.04	61.40	2.52	1.62	1.00	60.11	1.51	15.90
2H-2	MAD	12	14	11.22	41.54	71.05	2.70	1.61	0.94	65.13	1.87	15.78
2H-3	MAD	12	14	12.72	39.74	65.95	2.66	1.63	0.98	63.13	1.71	15.98
2H-4	MAD	12	14	14.22	40.81	68.95	2.47	1.57	0.93	62.39	1.66	15.38
2H-5	MAD	12	14	15.72	46.45	86.75	2.57	1.51	0.81	68.48	2.17	14.83
2H-7	MAD	12	14	18.72	45.82	84.56	2.55	1.52	0.82	67.78	2.10	14.88
3H-1	MAD	57	59	19.67	41.25	70.21	2.74	1.62	0.95	65.19	1.87	15.90
3H-2	MAD	57	59	21.17	41.60	71.23	2.70	1.61	0.94	65.23	1.88	15.78
3H-4	MAD	57	59	24.17	43.19	76.03	2.70	1.58	0.90	66.65	2.00	15.52
3H-6	MAD	57	59	27.17	39.19	64.44	2.74	1.66	1.01	63.26	1.72	16.24
3H-7	MAD	57	59	28.67	33.49	50.34	2.73	1.75	1.17	57.22	1.34	17.19
4H-1	MAD	57	59	29.17	35.05	53.96	2.75	1.73	1.12	59.10	1.44	16.97
4H-2	MAD	57	59	30.67	36.26	56.88	2.73	1.70	1.09	60.19	1.51	16.70
4H-3	MAD	57	59	32.17	36.03	56.33	2.72	1.71	1.09	59.91	1.49	16.73
4H-4	MAD	57	59	33.67	35.60	55.28	2.74	1.72	1.11	59.60	1.48	16.84
4H-5	MAD	57	59	35.17	31.34	45.65	2.76	1.80	1.24	55.11	1.23	17.69
4H-6	MAD	57	59	36.67	27.93	38.75	2.74	1.88	1.35	51.16	1.05	18.43
5H-1	MAD	17	19	38.27	34.86	53.53	2.71	1.72	1.12	58.54	1.41	16.89
5H-2	MAD	17	19	39.77	34.98	53.80	2.75	1.73	1.13	59.01	1.44	16.97
5H-3	MAD	17	19	41.27	33.65	50.72	2.76	1.76	1.17	57.72	1.37	17.26
5H-4	MAD	17	19	42.77	34.46	52.57	2.74	1.74	1.14	58.39	1.40	17.05
5H-5	MAD	17	19	44.27	35.72	55.58	2.75	1.72	1.10	59.82	1.49	16.85
5H-6	MAD	17	19	45.77	35.27	54.50	2.72	1.72	1.11	59.06	1.44	16.84
5H-7	MAD	17	19	47.27	32.44	48.02	2.75	1.78	1.20	56.24	1.29	17.44
6H-1	MAD	29	31	47.89	37.46	59.90	2.70	1.68	1.05	61.19	1.58	16.43
6H-2	MAD	29	31	49.18	34.95	53.74	2.70	1.72	1.12	58.55	1.41	16.85
6H-3	MAD	29	31	50.68	34.95	53.73	2.71	1.72	1.12	58.63	1.42	16.88
6H-4	MAD	29	31	52.18	33.59	50.58	2.71	1.75	1.16	57.21	1.34	17.14
6H-5	MAD	29	31	53.59	32.86	48.95	2.73	1.77	1.19	56.54	1.30	17.31
6H-6	MAD	29	31	55.09	34.85	53.48	2.72	1.73	1.12	58.62	1.42	16.93
6H-7	MAD	29	31	56.09	31.53	46.05	2.72	1.79	1.22	54.95	1.22	17.53
7H-1	MAD	79	81	57.89	32.23	47.56	2.73	1.78	1.20	55.85	1.26	17.43
7H-2	MAD	36	38	58.96	26.47	36.00	2.70	1.88	1.39	48.60	0.95	18.47
7H-3	MAD	36	38	60.37	31.77	46.56	2.70	1.78	1.21	55.05	1.22	17.43
7H-4	MAD	50	52	61.47	29.58	42.01	2.74	1.84	1.29	52.91	1.12	18.00
7H-5	MAD	50	52	62.97	30.87	44.66	2.73	1.80	1.25	54.26	1.19	17.68
7H-6	MAD	50	52	64.12	32.75	48.71	2.73	1.77	1.19	56.43	1.30	17.33
8H-1	MAD	36	38	66.96	32.67	48.52	2.69	1.76	1.18	56.01	1.27	17.23
8H-2	MAD	9	11	68.12	33.07	49.40	2.67	1.74	1.17	56.29	1.29	17.11
8H-3	MAD	9	11	69.48	32.85	48.92	2.70	1.76	1.18	56.30	1.29	17.22
8H-4	MAD	38	40	70.44	34.72	53.19	2.68	1.72	1.12	58.15	1.39	16.83
8H-5	MAD	17	19	71.60	31.89	46.82	2.66	1.76	1.20	54.85	1.21	17.28
8H-6	MAD	24	26	73.06	34.87	53.55	2.65	1.71	1.11	58.06	1.38	16.73
8H-7	MAD	27	29	73.75	33.44	50.24	2.65	1.73	1.15	56.54	1.30	16.99
9X-1	MAD	18	20	76.28	31.01	44.96	2.69	1.79	1.23	54.12	1.18	17.54
9X-1	MAD	82	84	76.92	31.21	45.37	2.71	1.79	1.23	54.52	1.20	17.56
9X-1	MAD	116	118	77.26	32.55	48.27	2.66	1.75	1.18	55.65	1.25	17.18
9X-2	MAD	29	31	77.89	29.52	41.88	2.61	1.79	1.26	51.64	1.07	17.58
9X-2	MAD	64	66	78.24	32.29	47.69	2.68	1.76	1.19	55.52	1.25	17.28
9X-4	MAD	13	15	79.66	29.52	41.89	2.61	1.79	1.26	51.63	1.07	17.58
9X-4	MAD	40	42	79.93	22.53	29.08	2.69	1.97	1.53	43.31	0.76	19.32
9X-4	MAD	56	58	80.09	33.81	51.07	2.74	1.75	1.16	57.74	1.37	17.16
9X-5	MAD	7	9	80.89	30.64	44.17	2.66	1.79	1.24	53.40	1.15	17.52
9X-5	MAD	51	53	81.33	24.37	32.22	2.67	1.92	1.45	45.63	0.84	18.82
11Y-1	MAD	15	17	86.85	33.38	50.11	2.73	1.75	1.17	57.16	1.33	17.21
11Y-1	MAD	71	73	87.41	36.50	57.48	2.33	1.59	1.01	56.64	1.31	15.60
12X-1	MAD	59	61	88.29	35.75	55.64	2.67	1.70	1.09	59.17	1.45	16.64

Table 12. Moisture and density (MAD) physical properties for Hole NGHP-01-15A.—Continued

Core, Section	Sample code	Depth, int, from (cm)	Depth, int, to (cm)	Depth (mbsf)	WCt (%)	WCs (%)	Grain density (g/cm³)	Bulk density (g/cm³)	Dry bulk density (g/cm³)	Porosity (%)	Void Ratio	Unit weight (kN/m³)
NGHP-01-15A—Continued												
12X-2	MAD	18	20	89.38	34.90	53.61	2.63	1.70	1.11	57.89	1.37	16.67
12X-3	MAD	15	17	90.85	35.06	53.98	2.65	1.70	1.11	58.26	1.40	16.70
12X-4	MAD	13	15	92.33	31.97	46.99	2.69	1.77	1.21	55.26	1.24	17.37
12X-5	MAD	9	11	93.79	33.40	50.15	2.68	1.74	1.16	56.70	1.31	17.06
12X-6	MAD	9	11	95.29	34.07	51.67	2.67	1.73	1.14	57.40	1.35	16.93
13X-1	MAD	11	13	97.41	37.25	59.37	2.68	1.67	1.05	60.79	1.55	16.40
13X-2	MAD	9	11	98.89	34.70	53.14	2.65	1.71	1.12	57.89	1.37	16.77
13X-3	MAD	14	16	100.44	32.29	47.69	2.65	1.75	1.19	55.20	1.23	17.18
13X-4	MAD	9	11	101.89	34.42	52.49	2.67	1.72	1.13	57.74	1.37	16.86
13X-5	MAD	10	12	103.40	37.57	60.18	2.66	1.66	1.04	60.94	1.56	16.30
14X-1	MAD	20	22	107.10	37.01	58.75	2.67	1.67	1.05	60.47	1.53	16.42
14X-2	MAD	14	16	108.54	36.82	58.29	2.69	1.68	1.06	60.45	1.53	16.50
14X-3	MAD	14	16	110.04	37.24	59.35	2.68	1.67	1.05	60.83	1.55	16.41
14X-6	MAD	19	21	113.51	35.15	54.21	2.71	1.72	1.11	58.87	1.43	16.83
15P-1	MAD	42	44	115.42	32.89	49.01	2.69	1.75	1.18	56.29	1.29	17.20
16Y-1	MAD	17	19	116.17	34.54	52.77	2.68	1.72	1.13	57.94	1.38	16.86
16Y-1	MAD	54	56	116.54	33.79	51.03	2.72	1.74	1.16	57.52	1.35	17.11
17X-1	MAD	9	11	117.09	35.40	54.80	2.74	1.72	1.11	59.47	1.47	16.88
17X-2	MAD	24	26	117.63	34.66	53.05	2.69	1.72	1.12	58.23	1.39	16.88
17X-3	MAD	13	15	119.02	34.20	51.98	2.65	1.72	1.13	57.36	1.35	16.86
17X-4	MAD	11	13	120.50	35.06	53.98	2.74	1.73	1.12	59.04	1.44	16.93
18X-1	MAD	19	21	126.79	34.70	53.13	2.72	1.73	1.13	58.47	1.41	16.94
18X-2	MAD	9	11	128.19	32.81	48.84	2.71	1.76	1.18	56.40	1.29	17.27
18X-3	MAD	9	11	129.69	31.78	46.57	2.73	1.79	1.22	55.37	1.24	17.51
18X-4	MAD	9	11	131.19	25.74	34.66	2.74	1.91	1.42	48.08	0.93	18.78
18X-5	MAD	14	16	132.74	25.25	33.78	2.74	1.93	1.44	47.46	0.90	18.89
18X-6	MAD	5	7	134.15	25.44	34.12	2.75	1.92	1.44	47.78	0.92	18.88
19X-1	MAD	18	20	136.38	27.58	38.08	2.72	1.87	1.35	50.24	1.01	18.31
19X-2	MAD	15	17	137.85	29.65	42.14	2.73	1.83	1.29	52.86	1.12	17.92
19X-3	MAD	30	32	139.50	29.64	42.13	2.72	1.82	1.28	52.77	1.12	17.89
19X-4	MAD	21	23	140.91	29.31	41.46	2.72	1.83	1.30	52.43	1.10	17.98
20X-1	MAD	57	59	146.37	30.25	43.37	2.73	1.82	1.27	53.63	1.16	17.82
20X-2	MAD	57	59	147.87	30.89	44.69	2.74	1.80	1.25	54.36	1.19	17.69
20X-3	MAD	57	59	149.37	33.28	49.89	2.71	1.76	1.17	57.08	1.33	17.24
20X-4	MAD	57	59	150.87	31.00	44.93	2.73	1.80	1.24	54.48	1.20	17.66
20X-5	MAD	57	59	152.37	33.17	49.63	2.76	1.77	1.18	57.23	1.34	17.34
21X-1	MAD	14	16	155.54	32.46	48.06	2.72	1.77	1.19	56.01	1.27	17.34
21X-2	MAD	14	16	157.04	32.72	48.64	2.71	1.76	1.18	56.22	1.28	17.27
21X-3	MAD	14	16	158.54	32.66	48.50	2.74	1.77	1.19	56.42	1.29	17.36
21X-4	MAD	14	16	160.04	30.49	43.86	2.71	1.81	1.26	53.74	1.16	17.71
21X-5	MAD	14	16	161.54	32.57	48.31	2.72	1.77	1.19	56.22	1.28	17.35
21X-6	MAD	14	16	163.04	31.59	46.18	2.73	1.79	1.22	55.12	1.23	17.54
21X-7	MAD	14	16	164.04	30.83	44.57	2.73	1.80	1.25	54.26	1.19	17.69
22X-1	MAD	30	32	165.30	31.41	45.80	2.73	1.79	1.23	54.97	1.22	17.59
22X-2	MAD	30	32	166.80	30.85	44.62	2.71	1.80	1.24	54.09	1.18	17.62
22X-4	MAD	30	32	168.90	31.11	45.17	2.71	1.79	1.24	54.46	1.20	17.59
22X-5	MAD	30	32	170.40	29.51	41.85	2.73	1.83	1.29	52.71	1.11	17.96
22X-6	MAD	30	32	171.90	30.84	44.59	2.72	1.80	1.25	54.23	1.18	17.67
23X-2	MAD	64	66	175.45	30.00	42.86	2.73	1.82	1.27	53.32	1.14	17.86
23X-3	MAD	64	66	176.95	30.68	44.26	2.75	1.81	1.26	54.25	1.19	17.77
23X-4	MAD	64	66	178.45	29.59	42.04	2.72	1.83	1.29	52.71	1.11	17.90
23X-5	MAD	64	66	179.95	28.90	40.64	2.74	1.85	1.31	52.12	1.09	18.13
23X-6	MAD	64	66	181.45	29.29	41.43	2.75	1.84	1.30	52.67	1.11	18.07
23X-7	MAD	64	66	182.88	29.90	42.66	2.73	1.82	1.28	53.16	1.13	17.87
24X-1	MAD	49	51	184.69	30.31	43.49	2.72	1.81	1.26	53.56	1.15	17.76
24X-2	MAD	49	51	186.19	28.80	40.45	2.76	1.85	1.32	52.12	1.09	18.19
24X-3	MAD	49	51	187.69	29.49	41.83	2.75	1.84	1.30	52.87	1.12	18.02
24X-4	MAD	49	51	189.19	27.36	37.66	2.75	1.88	1.37	50.24	1.01	18.46
24X-5	MAD	49	51	190.69	28.01	38.91	2.72	1.86	1.34	50.84	1.03	18.24
24X-6	MAD	49	51	192.19	26.94	36.87	2.73	1.89	1.38	49.57	0.98	18.49
24X-7	MAD	49	51	193.19	25.25	33.78	2.71	1.91	1.43	47.18	0.89	18.78
25X-1	MAD	11	13	193.91	29.69	42.22	2.75	1.83	1.29	53.13	1.13	17.99
25X-1	MAD	11	13	193.91	28.37	39.60	2.77	1.87	1.34	51.67	1.07	18.31
25X-1	MAD	12	14	193.92	27.03	37.05	2.74	1.89	1.38	49.78	0.99	18.51

Table 13. Vane shear strength results for Hole NGHP-01-15A.

Core, section	Sample	Top (cm)	Depth (mbsf)	Sv (kPa)	Sres (kPa)	Srem (kPa)	St
			NGHP-01-15A				
1H-1	VS	31	0.31	1.7	1.5	0.7	2.6
1H-1	VS	52	0.52	3.0	2.5	1.3	2.3
1H-1	VS	110	1.10	15.3	11.5	5.4	2.8
1H-2	VS	30	1.80	9.7	7.0	2.1	4.5
1H-3	VS	92	3.92	9.6	6.6	3.1	3.1
1H-4	VS	95	5.45	10.5	7.4	3.9	2.7
1H-5	VS	48	6.48	18.2	13.2	6.6	2.8
1H-6	VS	108	8.58	18.1	12.8	7.4	2.4
1H-7	VS	22	9.22	15.4	11.9	5.3	2.9
2H-1	VS	35	9.95	17.9	11.9	6.7	2.6
2H-2	VS	55	11.65	19.3	13.2	8.2	2.3
2H-3	VS	55	13.15	20.6	13.6	8.6	2.4
2H-4	VS	35	14.45	24.2	16.5	9.1	2.7
2H-5	VS	45	16.05	25.3	14.8	9.9	2.6
2H-6	VS	15	17.25	22.9	13.6	6.9	3.3
2H-7	VS	15	18.75	25.5	13.8	8.2	3.1
3H-1	VS	15	19.25	15.6	11.5	5.8	2.7
3H-2	VS	35	20.95	19.7	18.1	11.5	1.7
3H-3	VS	15	22.25	23.9	13.2	9.9	2.4
3H-4	VS	15	23.75	28.0	14.8	10.7	2.6
3H-5	VS	15	25.25	26.3	16.5	11.5	2.3
3H-6	VS	15	26.75	32.9	19.7	13.2	2.5
3H-7	VS	40	28.50	32.9	21.4	13.2	2.5
4H-1	VS	40	29.00	24.7	14.0	9.9	2.5
4H-2	VS	35	30.45	36.2	24.7	13.2	2.8

Table 14. Pocket Penetrometer strength results for Hole NGHP-01-15A.

Core, section	Sample	Top (cm)	Depth (mbsf)	Spp (kPa)	Core, section	Sample	Top (cm)	Depth (mbsf)	Spp (kPa)
					NGHP-01-15A				
1H-1	PP	67	0.67	3.1	2H-5	PP	17	15.77	12.3
1H-1	PP	103	1.03	4.3	2H-6	PP	17	17.27	12.3
1H-1	PP	130	1.30	6.9	2H-7	PP	16	18.76	10.7
1H-2	PP	40	1.90	3.8	3H-1	PP	50	19.60	12.3
1H-2	PP	93	2.43	4.6	3H-2	PP	50	21.10	24.5
1H-3	PP	20	3.20	8.0	3H-3	PP	50	22.60	24.5
1H-3	PP	77	3.77	4.9	3H-4	PP	50	24.10	24.5
1H-4	PP	27	4.77	6.7	3H-5	PP	50	25.60	24.5
1H-4	PP	110	5.60	7.0	3H-6	PP	50	27.10	24.5
1H-5	PP	9	6.09	10.0	3H-7	PP	50	28.60	24.5
1H-5	PP	74	6.74	11.0	4H-1	PP	53	29.13	12.3
1H-6	PP	23	7.73	10.1	4H-2	PP	53	30.63	49.0
1H-6	PP	95	8.45	12.3	4H-3	PP	53	32.13	24.5
1H-7	PP	7	9.07	8.4	4H-4	PP	53	33.63	85.8
2H-1	PP	17	9.77	12.3	4H-5	PP	53	35.13	61.3
2H-2	PP	17	11.27	12.3	4H-6	PP	53	36.63	73.5
2H-3	PP	17	12.77	12.3	5H-1	PP	18	38.28	24.5
2H-4	PP	17	14.27	12.3	5H-2	PP	18	39.78	34.3

Table 14. Pocket Penetrometer strength results for Hole NGHP-01-15A.—Continued

Core, section	Sample	Top (cm)	Depth (mbsf)	Spp (kPa)	Core, section	Sample	Top (cm)	Depth (mbsf)	Spp (kPa)
NGHP-01-15A									
5H-3	PP	18	41.28	24.5	15P-1	PP	14	115.14	49.0
5H-4	PP	18	42.78	24.5	15P-1	PP	43	115.43	127.4
5H-5	PP	18	44.28	24.5	15P-1	PP	81	115.81	85.8
5H-6	PP	18	45.78	24.5	17X-1	PP	10	117.10	34.3
5H-7	PP	18	47.28	36.8	17X-2	PP	24	117.63	83.3
6H-1	PP	32	47.92	36.8	17X-3	PP	13	119.02	73.5
6H-2	PP	32	49.21	36.8	17X-4	PP	12	120.51	88.2
6H-3	PP	32	50.71	49.0	17X-4	PP	15	120.54	73.5
6H-4	PP	32	52.21	24.5	18X-1	PP	20	126.80	53.9
6H-5	PP	32	53.62	36.8	18X-2	PP	10	128.20	83.3
6H-6	PP	32	55.12	61.3	18X-3	PP	10	129.70	83.3
6H-7	PP	37	56.17	49.0	18X-4	PP	10	131.20	117.6
7H-1	PP	80	57.90	14.7	18X-5	PP	14	132.74	142.1
7H-2	PP	18	58.78	49.0	18X-6	PP	6	134.16	122.5
7H-3	PP	18	60.19	49.0	18X-6	PP	20	134.30	73.5
7H-4	PP	18	61.15	49.0	19X-1	PP	19	136.39	120.1
7H-5	PP	18	62.65	61.3	19X-2	PP	16	137.86	98.0
7H-6	PP	18	63.80	39.2	19X-3	PP	31	139.51	93.1
8H-1	PP	57	67.17	49.0	19X-4	PP	22	140.92	107.8
8H-2	PP	100	69.03	85.8	20X-1	PP	30	146.10	44.1
8H-3	PP	10	69.49	61.3	20X-2	PP	10	147.40	36.8
8H-4	PP	20	70.26	61.3	20X-3	PP	10	148.90	49.0
8H-5	PP	26	71.69	36.8	20X-4	PP	10	150.40	78.4
8H-6	PP	26	73.08	36.8	20X-5	PP	10	151.90	63.7
8H-7	PP	26	73.74	36.8	21X-1	PP	15	155.55	98.0
9X-1	PP	19	76.29	49.0	21X-2	PP	15	157.05	122.5
9X-1	PP	23	76.33	58.8	21X-3	PP	15	158.55	93.1
9X-1	PP	25	76.35	49.0	21X-4	PP	15	160.05	110.3
9X-2	PP	29	77.89	73.5	21X-5	PP	15	161.55	93.1
9X-2	PP	65	78.25	98.0	21X-6	PP	15	163.05	93.1
9X-4	PP	13	79.66	83.3	21X-7	PP	15	164.05	110.3
9X-4	PP	54	80.07	110.3	22X-1	PP	32	165.32	85.8
9X-5	PP	9	80.91	73.5	22X-2	PP	32	166.82	110.3
9X-5	PP	52	81.34	68.6	22X-4	PP	32	168.92	98.0
12X-1	PP	60	88.30	83.3	22X-5	PP	32	170.42	85.8
12X-2	PP	19	89.39	85.8	22X-6	PP	32	171.92	73.5
12X-3	PP	16	90.86	93.1	23X-2	PP	65	175.46	134.8
12X-4	PP	14	92.34	102.9	23X-4	PP	65	178.46	98.0
12X-5	PP	10	93.80	122.5	23X-5	PP	65	179.96	122.5
12X-6	PP	10	95.30	110.3	23X-6	PP	65	181.46	122.5
13X-1	PP	12	97.42	63.7	23X-7	PP	65	182.89	98.0
13X-2	PP	10	98.90	63.7	24X-1	PP	49	184.69	110.3
13X-3	PP	14	100.44	85.8	24X-2	PP	49	186.19	110.3
13X-4	PP	10	101.90	63.7	24X-3	PP	49	187.69	85.8
13X-5	PP	11	103.41	68.6	24X-4	PP	49	189.19	98.0
14X-1	PP	16	107.06	58.8	24X-5	PP	49	190.69	85.8
14X-2	PP	15	108.55	61.3	24X-6	PP	49	192.19	110.3
14X-3	PP	15	110.05	61.3	24X-7	PP	49	193.19	134.8
14X-4	PP	15	111.55	73.5	25X-1	PP	12	193.92	58.8
14X-6	PP	20	113.52	73.5	25X-2	PP	13	195.43	107.8
					25X-3	PP	13	196.93	98.0

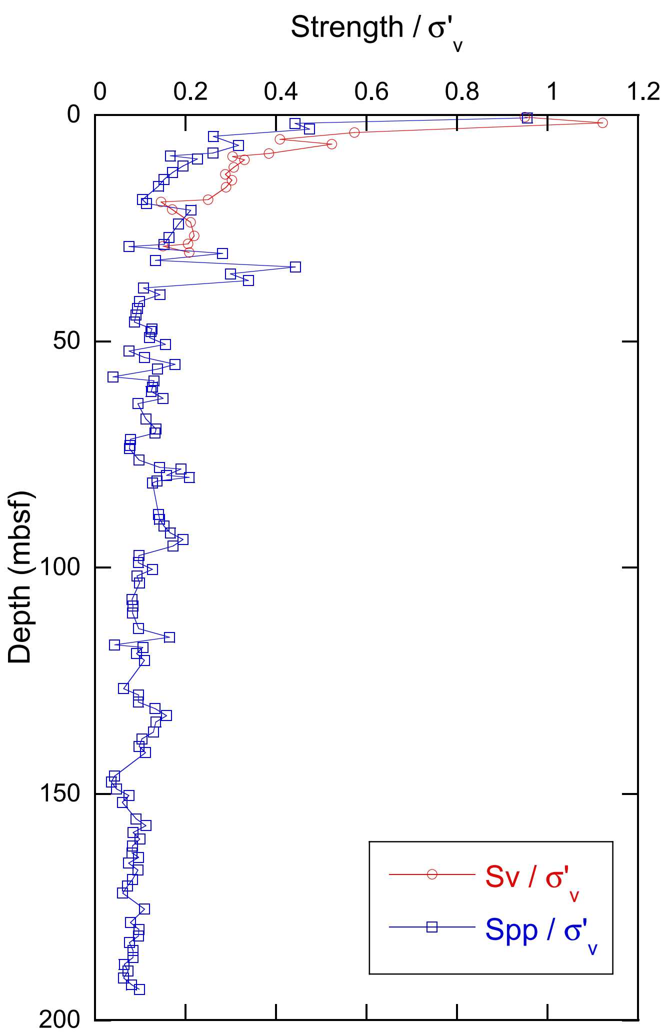

Figure 23. Shear strengths normalized to the effective vertical stress versus subbottom depth for Hole NGHP-01-15A.

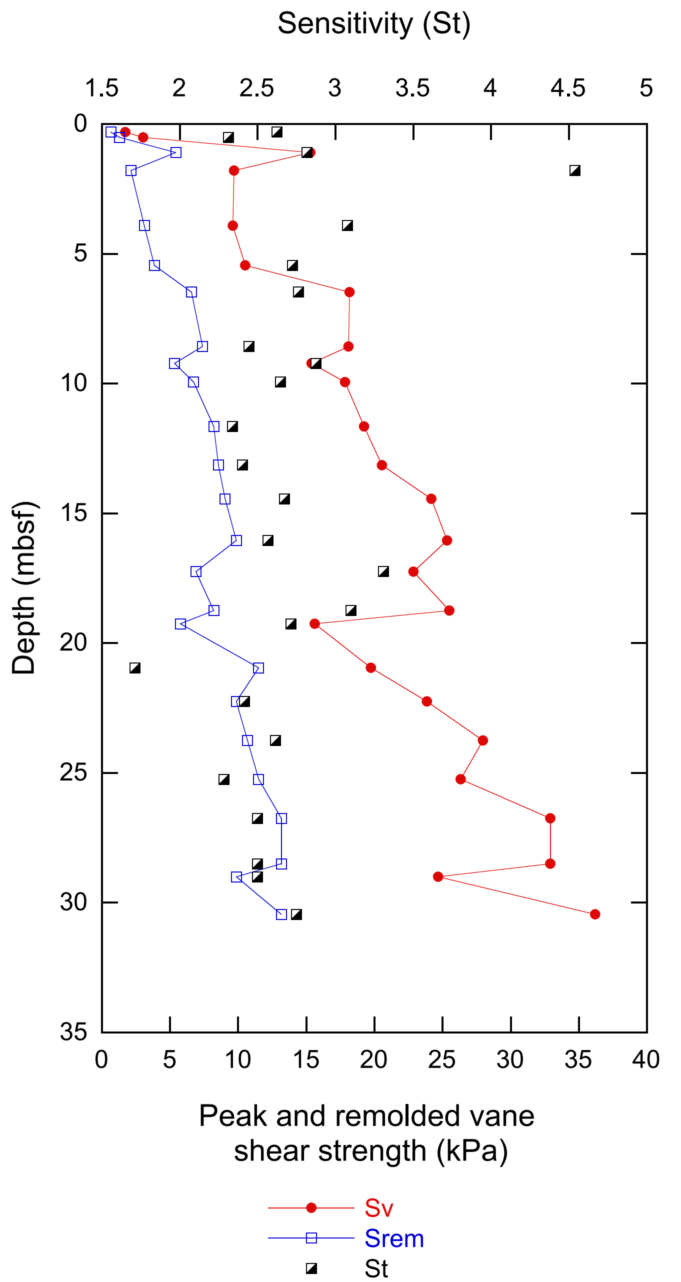

Figure 24. Peak and remolded vane shear strengths and sensitivity for Hole NGHP-01-15A. [Sv, peak vane shear strength; Srem, remolded vane shear strength; St, shear strength sensitivity]

Table 15. Wenner array electrical resistivity and formation factor results for Hole NGHP-01-15A. (To view the complete table, please see the ASCII files.)

Core, section	Sample	Top (cm)	Depth (mbsf)	Electrical resistivity (W×m)	Apparent formation factor	Comments
			NGHP-01-15A			
1H-1	ER	32	0.32	0.413	2.065	
1H-1	ER	44	0.44	0.416	2.080	
1H-1	ER	63	0.63	0.499	2.495	
1H-1	ER	81	0.81	0.51	2.550	
1H-1	ER	95	0.95	0.537	2.685	
1H-1	ER	108	1.08	0.569	2.845	
1H-1	ER	118	1.18	0.524	2.620	
1H-1	ER	128	1.28	0.509	2.545	
1H-2	ER	10	1.60	0.525	2.625	
1H-2	ER	30	1.80	0.52	2.600	
1H-2	ER	50	2.00	0.516	2.580	
1H-2	ER	70	2.20	0.529	2.645	
1H-2	ER	90	2.40	0.509	2.545	
1H-2	ER	110	2.60	0.528	2.640	
1H-2	ER	130	2.80	0.529	2.645	
1H-3	ER	17	3.17	0.579	2.895	
1H-3	ER	33	3.33	0.597	2.985	
1H-3	ER	52	3.52	0.555	2.775	
1H-3	ER	72	3.72	0.537	2.685	
1H-3	ER	92	3.92	0.534	2.670	
1H-4	ER	15	4.65	0.533	2.665	
1H-4	ER	35	4.85	0.531	2.655	
1H-4	ER	55	5.05	0.533	2.665	
1H-4	ER	75	5.25	0.534	2.670	
1H-4	ER	95	5.45	0.526	2.630	
1H-4	ER	115	5.65	0.523	2.615	
1H-4	ER	135	5.85	0.523	2.615	
1H-5	ER	15	6.15	0.611	3.055	
1H-5	ER	35	6.35	0.553	2.765	
1H-5	ER	55	6.55	0.556	2.780	
1H-5	ER	75	6.75	0.532	2.660	
1H-5	ER	88	6.88	0.613	3.065	
1H-6	ER	10	7.60	0.553	2.765	
1H-6	ER	15	7.65	0.569	2.845	
1H-6	ER	30	7.80	0.564	2.820	
1H-6	ER	35	7.85	0.542	2.710	
1H-6	ER	55	8.05	0.551	2.755	
1H-6	ER	75	8.25	0.541	2.705	
1H-6	ER	95	8.45	0.564	2.820	
1H-6	ER	115	8.65	0.564	2.820	
1H-6	ER	135	8.85	0.571	2.855	
2H-1	ER	15	9.75	0.647	3.235	
2H-1	ER	35	9.95	0.63	3.150	
2H-1	ER	55	10.15	0.623	3.115	
2H-1	ER	75	10.35	0.638	3.190	
2H-1	ER	95	10.55	0.633	3.165	
2H-1	ER	115	10.75	0.598	2.990	
2H-1	ER	129	10.89	0.616	3.080	
2H-2	ER	15	11.25	0.593	2.965	
2H-2	ER	35	11.45	0.579	2.895	
2H-2	ER	55	11.65	0.647	3.235	
2H-2	ER	75	11.85	0.619	3.095	

Table 15. Wenner array electrical resistivity and formation factor results for Hole NGHP-01-15A. (To view the complete table, please see the ASCII files.)—Continued

Core, section	Sample	Top (cm)	Depth (mbsf)	Electrical resistivity (W×m)	Apparent formation factor	Comments
NGHP-01-15A—Continued						
2H-2	ER	95	12.05	0.608	3.040	
2H-2	ER	115	12.25	0.595	2.975	
2H-3	ER	15	12.75	0.596	2.980	
2H-3	ER	35	12.95	0.573	2.865	
2H-3	ER	55	13.15	0.62	3.100	
2H-3	ER	75	13.35	0.596	2.980	
2H-3	ER	95	13.55	0.601	3.005	
2H-4	ER	15	14.25	0.6	3.000	
2H-4	ER	35	14.45	0.556	2.780	
2H-4	ER	55	14.65	0.548	2.740	
2H-4	ER	75	14.85	0.555	2.775	
2H-4	ER	95	15.05	0.6	3.000	
2H-4	ER	115	15.25	0.547	2.735	
2H-4	ER	135	15.45	0.568	2.840	
2H-5	ER	15	15.75	0.572	2.860	
2H-5	ER	35	15.95	0.533	2.665	
2H-5	ER	55	16.15	0.556	2.780	
2H-5	ER	75	16.35	0.572	2.860	
2H-5	ER	90	16.50	0.56	2.800	
2H-6	ER	15	17.25	0.529	2.645	
2H-6	ER	35	17.45	0.546	2.730	
2H-6	ER	55	17.65	0.578	2.890	
2H-6	ER	75	17.85	0.559	2.795	
2H-6	ER	95	18.05	0.529	2.645	
2H-6	ER	115	18.25	0.546	2.730	
2H-7	ER	15	18.75	0.523	2.615	
2H-7	ER	35	18.95	0.508	2.540	
2H-7	ER	55	19.15	0.533	2.665	
3H-1	ER	15	19.25	0.551	2.755	
3H-1	ER	45	19.55	0.558	2.790	
3H-1	ER	65	19.75	0.535	2.675	
3H-1	ER	85	19.95	0.543	2.715	
3H-1	ER	105	20.15	0.562	2.810	
3H-1	ER	125	20.35	0.524	2.620	
3H-2	ER	15	20.75	0.547	2.735	
3H-2	ER	15	20.75	0.576	2.880	
3H-2	ER	35	20.95	0.504	2.520	
3H-2	ER	55	21.15	0.573	2.865	
3H-2	ER	75	21.35	0.506	2.530	
3H-2	ER	95	21.55	0.57	2.850	
3H-2	ER	115	21.75	0.535	2.675	
3H-3	ER	15	22.25	0.579	2.895	
3H-3	ER	35	22.45	0.553	2.765	
3H-3	ER	55	22.65	0.478	2.390	
3H-3	ER	75	22.85	0.438	2.190	
3H-3	ER	95	23.05	0.515	2.575	
3H-4	ER	15	23.75	0.296	1.480	
3H-4	ER	35	23.95	0.522	2.610	
3H-4	ER	75	24.35	0.551	2.755	
3H-4	ER	95	24.55	0.592	2.960	
3H-4	ER	124	24.84	0.645	3.225	
3H-5	ER	15	25.25	0.578	2.890	
3H-5	ER	35	25.45	0.598	2.990	
3H-5	ER	55	25.65	0.67	3.350	
3H-5	ER	80	25.90	0.572	2.860	

Table 15. Wenner array electrical resistivity and formation factor results for Hole NGHP-01-15A. (To view the complete table, please see the ASCII files.)—Continued

Core, section	Sample	Top (cm)	Depth (mbsf)	Electrical resistivity (W×m)	Apparent formation factor	Comments
NGHP-01-15A—Continued						
3H-6	ER	15	26.75	0.665	3.325	
3H-6	ER	35	26.95	0.619	3.095	
3H-6	ER	55	27.15	0.637	3.185	
3H-6	ER	75	27.35	0.548	2.740	
3H-6	ER	95	27.55	0.568	2.840	
3H-6	ER	115	27.75	0.617	3.085	
3H-7	ER	15	28.25	0.568	2.840	
3H-7	ER	40	28.50	0.656	3.280	
4H-1	ER	20	28.80	0.659	3.295	
4H-1	ER	40	29.00	0.473	2.365	
4H-1	ER	60	29.20	0.641	3.205	
4H-1	ER	80	29.40	0.616	3.080	
4H-1	ER	120	29.80	0.727	3.635	
4H-1	ER	120	29.80	0.617	3.085	
4H-2	ER	15	30.25	0.662	3.310	
4H-2	ER	35	30.45	0.551	2.755	
4H-2	ER	55	30.65	0.707	3.535	
4H-2	ER	75	30.85	0.649	3.245	
4H-2	ER	95	31.05	0.596	2.980	
4H-3	ER	15	31.75	0.668	3.340	
4H-3	ER	35	31.95	0.777	3.885	
4H-3	ER	67	32.27	0.687	3.435	
4H-3	ER	95	32.55	0.657	3.285	
4H-4	ER	15	33.25	0.665	3.325	
4H-4	ER	35	33.45	0.658	3.290	
4H-4	ER	55	33.65	0.899	4.495	
4H-4	ER	83	33.93	0.702	3.510	
4H-5	ER	20	34.80	0.883	4.415	
4H-5	ER	40	35.00	0.822	4.110	
4H-5	ER	60	35.20	0.953	4.765	
4H-5	ER	90	35.50	0.889	4.445	
4H-6	ER	15	36.25	1.075	5.375	
4H-6	ER	55	36.65	0.796	3.980	
5H-1	ER	20	38.30	0.665	3.325	
5H-1	ER	40	38.50	0.741	3.705	
5H-1	ER	60	38.70	0.714	3.570	
5H-1	ER	80	38.90	0.671	3.355	
5H-1	ER	100	39.10	0.516	2.580	
5H-1	ER	120	39.30	0.726	3.630	
5H-1	ER	140	39.50	0.702	3.510	
5H-2	ER	15	39.75	0.7	3.500	
5H-2	ER	35	39.95	0.668	3.340	
5H-2	ER	55	40.15	0.618	3.090	
5H-2	ER	75	40.35	0.613	3.065	
5H-2	ER	95	40.55	0.664	3.320	
5H-2	ER	115	40.75	0.686	3.430	
5H-2	ER	135	40.95	0.695	3.475	
5H-3	ER	15	41.25	0.692	3.460	
5H-3	ER	35	41.45	0.733	3.665	
5H-3	ER	55	41.65	0.694	3.470	
5H-3	ER	80	41.90	0.651	3.255	
5H-3	ER	100	42.10	0.593	2.965	
5H-4	ER	15	42.75	0.66	3.300	
5H-4	ER	35	42.95	0.655	3.275	
5H-4	ER	58	43.18	0.728	3.640	

Table 15. Wenner array electrical resistivity and formation factor results for Hole NGHP-01-15A. (To view the complete table, please see the ASCII files.)—Continued

Core, section	Sample	Top (cm)	Depth (mbsf)	Electrical resistivity (W×m)	Apparent formation factor	Comments
NGHP-01-15A—Continued						
5H-4	ER	78	43.38	0.603	3.015	
5H-4	ER	100	43.60	0.644	3.220	
5H-4	ER	120	43.80	0.66	3.300	
5H-5	ER	15	44.25	0.85	4.250	
5H-5	ER	35	44.45	0.624	3.120	
5H-5	ER	55	44.65	0.737	3.685	
5H-5	ER	75	44.85	0.705	3.525	
5H-6	ER	15	45.75	0.713	3.565	
5H-6	ER	35	45.95	0.692	3.460	
5H-6	ER	55	46.15	0.899	4.495	
5H-6	ER	83	46.43	0.81	4.050	
5H-6	ER	110	46.70	0.844	4.220	
5H-6	ER	125	46.85	0.755	3.775	
5H-7	ER	18	47.28	0.721	3.605	
6H-1	ER	20	47.80	0.625	3.125	
6H-1	ER	40	48.00	0.689	3.445	
6H-1	ER	60	48.20	0.753	3.765	
6H-1	ER	85	48.45	0.851	4.255	
6H-1	ER	105	48.65	0.701	3.505	
6H-2	ER	15	49.04	0.734	3.670	
6H-2	ER	35	49.24	0.79	3.950	
6H-2	ER	55	49.44	0.723	3.615	
6H-2	ER	75	49.64	0.749	3.745	
6H-2	ER	120	50.09	0.864	4.320	
6H-3	ER	20	50.59	0.796	3.980	
6H-3	ER	45	50.84	0.775	3.875	
6H-3	ER	75	51.14	0.609	3.045	
6H-4	ER	15	52.04	0.756	3.780	
6H-4	ER	40	52.29	0.726	3.630	
6H-4	ER	40	52.29	0.639	3.195	
6H-4	ER	55	52.44	0.73	3.650	
6H-4	ER	80	52.69	0.779	3.895	
6H-4	ER	105	52.94	0.781	3.905	
6H-4	ER	125	53.14	0.736	3.680	
6H-5	ER	15	53.45	0.774	3.870	
6H-5	ER	35	53.65	0.825	4.125	
6H-5	ER	55	53.85	0.8	4.000	
6H-5	ER	75	54.05	0.824	4.120	
6H-6	ER	20	55.00	0.812	4.060	
6H-6	ER	40	55.20	0.718	3.590	
6H-6	ER	82	55.62	0.742	3.710	
6H-7	ER	20	56.00	0.9	4.500	
6H-7	ER	65	56.45	0.811	4.055	
7H-1	ER	35	57.45	0.656	3.280	
7H-1	ER	55	57.65	0.601	3.005	
7H-1	ER	75	57.85	0.673	3.365	
7H-1	ER	95	58.05	0.571	2.855	
7H-1	ER	115	58.25	0.706	3.530	
7H-1	ER	135	58.45	0.746	3.730	
7H-2	ER	20	58.80	0.89	4.450	
7H-2	ER	40	59.00	1.062	5.310	
7H-2	ER	60	59.20	0.737	3.685	
7H-2	ER	80	59.40	0.987	4.935	
7H-2	ER	100	59.60	0.837	4.185	

Table 15. Wenner array electrical resistivity and formation factor results for Hole NGHP-01-15A. (To view the complete table, please see the ASCII files.)—Continued

Core, section	Sample	Top (cm)	Depth (mbsf)	Electrical resistivity (W×m)	Apparent formation factor	Comments
NGHP-01-15A—Continued						
7H-2	ER	120	59.80	0.769	3.845	
7H-3	ER	15	60.16	0.811	4.055	
7H-3	ER	40	60.41	0.787	3.935	
7H-4	ER	15	61.12	0.763	3.815	
7H-4	ER	40	61.37	0.876	4.380	
7H-4	ER	60	61.57	1.138	5.690	
7H-4	ER	90	61.87	0.765	3.825	
7H-4	ER	135	62.32	0.858	4.290	
7H-5	ER	15	62.62	0.806	4.030	
7H-5	ER	35	62.82	0.8	4.000	
7H-6	ER	15	63.77	0.753	3.765	
7H-6	ER	35	63.97	0.761	3.805	
7H-6	ER	55	64.17	0.75	3.750	
7H-6	ER	90	64.52	0.665	3.325	
8H-1	ER	30	66.90	0.866	4.330	
8H-1	ER	50	67.10	1.165	5.825	
8H-1	ER	50	67.10	0.998	4.990	
8H-1	ER	70	67.30	1.045	5.225	
8H-1	ER	110	67.70	1.015	5.075	
8H-2	ER	28	68.31	0.816	4.080	
8H-2	ER	85	68.88	0.769	3.845	
8H-2	ER	110	69.13	0.625	3.125	
8H-3	ER	21	69.60	0.662	3.310	
8H-4	ER	20	70.26	0.861	4.305	
8H-4	ER	40	70.46	0.907	4.535	
8H-4	ER	68	70.74	0.918	4.590	
8H-5	ER	45	71.88	0.8	4.000	
8H-6	ER	25	73.07	0.838	4.190	
8H-6	ER	51	73.33	0.872	4.360	
8H-7	ER	20	73.68	0.666	3.330	
8H-7	ER	40	73.88	0.769	3.845	
8H-7	ER	60	74.08	0.824	4.120	
8H-7	ER	80	74.28	0.841	4.205	
9X-1	ER	26	76.36	2.55	12.750	Sand—GH core
9X-1	ER	51	76.61	2.543	12.715	Sand
9X-1	ER	84	76.94	2.197	10.985	
9X-1	ER	117	77.27	2.059	10.295	Clay with underlying sand
9X-2	ER	5	77.65	2.859	14.295	Fine grained
9X-2	ER	28	77.88	1.896	9.480	Sandier
9X-2	ER	45	78.05	4.884	24.420	Sand
9X-2	ER	59	78.19	1.289	6.445	Fine grained
9X-2	ER	65	78.25	1.772	8.860	
9X-4	ER	14	79.67	2.033	10.165	
9X-4	ER	31	79.84	7.202	36.010	Sand
9X-4	ER	47	80.00	1.224	6.120	
9X-4	ER	54	80.07	1.547	7.735	Fine grained
9X-5	ER	8	80.90	2.106	10.530	Fine grained
9X-5	ER	38	81.20	1.269	6.345	
9X-5	ER	51	81.33	1.94	9.700	Thin sand layer
12X-1	ER	1	87.71	0.248	1.240	
12X-1	ER	3	87.73	1.016	5.080	Fine grained
12X-1	ER	16	87.86	1.365	6.825	Sandy
12X-1	ER	37	88.07	1.074	5.370	
12X-1	ER	56	88.26	0.749	3.745	

Table 15. Wenner array electrical resistivity and formation factor results for Hole NGHP-01-15A. (To view the complete table, please see the ASCII files.)—Continued

Core, section	Sample	Top (cm)	Depth (mbsf)	Electrical resistivity (W×m)	Apparent formation factor	Comments
			NGHP-01-15A—Continued			
12X-1	ER	75	88.45	0.957	4.785	
12X-1	ER	95	88.65	0.742	3.710	Carbonates
12X-1	ER	120	88.90	0.751	3.755	
12X-1	ER	140	89.10	0.771	3.855	
12X-2	ER	10	89.30	0.739	3.695	
12X-2	ER	30	89.50	0.836	4.180	
12X-2	ER	50	89.70	0.753	3.765	
12X-2	ER	72	89.92	0.791	3.955	
12X-2	ER	90	90.10	0.866	4.330	
12X-2	ER	109	90.29	0.888	4.440	
12X-3	ER	10	90.80	0.674	3.370	
12X-3	ER	30	91.00	0.757	3.785	
12X-3	ER	50	91.20	0.762	3.810	
12X-3	ER	71	91.41	0.718	3.590	
12X-3	ER	87	91.57	0.786	3.930	
12X-4	ER	15	92.35	0.929	4.645	
12X-4	ER	34	92.54	0.939	4.695	
12X-4	ER	55	92.75	0.701	3.505	
12X-4	ER	77	92.97	0.727	3.635	
12X-4	ER	96	93.16	0.738	3.690	
12X-4	ER	115	93.35	0.815	4.075	
12X-5	ER	15	93.85	0.749	3.745	
12X-5	ER	35	94.05	0.728	3.640	
12X-5	ER	56	94.26	0.69	3.450	
12X-5	ER	76	94.46	0.757	3.785	
12X-6	ER	10	95.30	0.722	3.610	
12X-6	ER	30	95.50	0.695	3.475	
12X-6	ER	48	95.68	0.757	3.785	
12X-6	ER	66	95.86	0.771	3.855	
12X-6	ER	86	96.06	0.787	3.935	
13X-1	ER	12	97.42	0.587	2.935	
13X-1	ER	35	97.65	0.696	3.480	
13X-1	ER	55	97.85	0.68	3.400	
13X-1	ER	76	98.06	0.635	3.175	
13X-1	ER	94	98.24	0.715	3.575	
13X-1	ER	115	98.45	0.737	3.685	
13X-1	ER	135	98.65	0.827	4.135	
13X-2	ER	7	98.87	0.725	3.625	
13X-2	ER	35	99.15	0.81	4.050	
13X-2	ER	55	99.35	0.778	3.890	
13X-2	ER	75	99.55	0.857	4.285	
13X-3	ER	15	100.45	0.82	4.100	
13X-3	ER	36	100.66	0.704	3.520	
13X-3	ER	55	100.85	0.831	4.155	
13X-3	ER	79	101.09	0.726	3.630	
13X-3	ER	95	101.25	0.761	3.805	
13X-3	ER	115	101.45	0.842	4.210	
13X-3	ER	135	101.65	0.781	3.905	
13X-4	ER	15	101.95	0.679	3.395	
13X-4	ER	35	102.15	0.714	3.570	
13X-4	ER	55	102.35	0.731	3.655	
13X-4	ER	66	102.46	0.672	3.360	
13X-5	ER	15	103.45	0.632	3.160	

Table 15. Wenner array electrical resistivity and formation factor results for Hole NGHP-01-15A. (To view the complete table, please see the ASCII files.)—Continued

Core, section	Sample	Top (cm)	Depth (mbsf)	Electrical resistivity (W×m)	Apparent formation factor	Comments
NGHP-01-15A—Continued						
13X-5	ER	21	103.51	0.69	3.450	
14X-1	ER	15	107.05	0.658	3.290	
14X-1	ER	35	107.25	0.663	3.315	
14X-1	ER	55	107.45	0.73	3.650	
14X-1	ER	75	107.65	0.7	3.500	
14X-1	ER	95	107.85	0.667	3.335	
14X-1	ER	115	108.05	0.658	3.290	
14X-1	ER	135	108.25	0.753	3.765	
14X-2	ER	15	108.55	0.611	3.055	
14X-2	ER	35	108.75	0.628	3.140	
14X-2	ER	55	108.95	0.646	3.230	
14X-2	ER	75	109.15	0.687	3.435	
14X-2	ER	95	109.35	0.749	3.745	
14X-2	ER	115	109.55	0.667	3.335	
14X-2	ER	136	109.76	0.706	3.530	
14X-3	ER	15	110.05	0.656	3.280	
14X-3	ER	36	110.26	0.649	3.245	
14X-3	ER	56	110.46	0.741	3.705	
14X-3	ER	76	110.66	0.721	3.605	
14X-4	ER	15	111.55	0.867	4.335	
14X-4	ER	35	111.75	0.769	3.845	
14X-4	ER	55	111.95	0.694	3.470	
14X-4	ER	75	112.15	0.748	3.740	
14X-4	ER	95	112.35	0.724	3.620	
14X-4	ER	107	112.47	0.689	3.445	
14X-6	ER	20	113.52	0.824	4.120	
14X-6	ER	40	113.72	0.713	3.565	
14X-6	ER	60	113.92	0.693	3.465	
14X-6	ER	77	114.09	0.865	4.325	
15P-1	ER	16	115.16	0.688	3.440	Intact pressure core
15P-1	ER	79	115.79	0.822	4.110	
17X-1	ER	15	117.15	0.699	3.495	
17X-1	ER	34	117.34	0.673	3.365	
17X-2	ER	14	117.53	0.626	3.130	
17X-2	ER	38	117.77	0.65	3.250	
17X-2	ER	58	117.97	0.736	3.680	
17X-2	ER	74	118.13	0.765	3.825	
17X-3	ER	19	119.08	0.812	4.060	
17X-3	ER	35	119.24	0.789	3.945	
17X-3	ER	55	119.44	0.681	3.405	
17X-3	ER	76	119.65	0.686	3.430	
17X-3	ER	95	119.84	0.743	3.715	
17X-3	ER	115	120.04	0.769	3.845	
17X-3	ER	135	120.24	0.718	3.590	
17X-4	ER	9	120.48	0.66	3.300	
17X-4	ER	20	120.59	0.651	3.255	
18X-1	ER	19	126.79	0.953	4.765	
18X-1	ER	35	126.95	0.704	3.520	
18X-1	ER	55	127.15	0.809	4.045	
18X-1	ER	75	127.35	0.746	3.730	
18X-1	ER	95	127.55	0.922	4.610	
18X-1	ER	115	127.75	0.791	3.955	
18X-1	ER	135	127.95	0.742	3.710	

Table 15. Wenner array electrical resistivity and formation factor results for Hole NGHP-01-15A. (To view the complete table, please see the ASCII files.)—Continued

Core, section	Sample	Top (cm)	Depth (mbsf)	Electrical resistivity (W×m)	Apparent formation factor	Comments
NGHP-01-15A—Continued						
18X-2	ER	15	128.25	0.644	3.220	
18X-2	ER	35	128.45	0.76	3.800	
18X-2	ER	55	128.65	0.716	3.580	
18X-2	ER	75	128.85	0.725	3.625	
18X-2	ER	95	129.05	0.749	3.745	
18X-2	ER	117	129.27	0.721	3.605	
18X-3	ER	15	129.75	0.789	3.945	
18X-3	ER	46	130.06	0.674	3.370	
18X-3	ER	66	130.26	0.904	4.520	
18X-3	ER	83	130.43	0.711	3.555	
18X-4	ER	12	131.22	0.887	4.435	
18X-4	ER	35	131.45	0.845	4.225	
18X-4	ER	56	131.66	0.818	4.090	
18X-4	ER	75	131.85	1.185	5.925	
18X-4	ER	95	132.05	0.868	4.340	
18X-4	ER	115	132.25	0.916	4.580	
18X-4	ER	135	132.45	0.903	4.515	
18X-5	ER	14	132.74	0.892	4.460	
18X-5	ER	36	132.96	0.955	4.775	
18X-5	ER	56	133.16	0.933	4.665	
18X-5	ER	75	133.35	0.977	4.885	
18X-6	ER	7	134.17	0.925	4.625	
18X-6	ER	17	134.27	1.182	5.910	
19X-1	ER	15	136.35	0.998	4.990	
19X-1	ER	35	136.55	0.929	4.645	
19X-1	ER	56	136.76	0.836	4.180	
19X-1	ER	75	136.95	0.845	4.225	
19X-2	ER	15	137.85	0.785	3.925	Biscuit/infilling start
19X-2	ER	16	137.86	0.861	4.305	
19X-2	ER	17	137.87	0.841	4.205	Alternating
19X-2	ER	18	137.88	0.857	4.285	readings in
19X-2	ER	19	137.89	0.876	4.380	biscuits
19X-2	ER	20	137.90	0.935	4.675	and
19X-2	ER	21	137.91	0.846	4.230	infilling
19X-2	ER	22	137.92	0.806	4.030	
19X-2	ER	23	137.93	0.785	3.925	
19X-2	ER	24	137.94	0.816	4.080	Biscuit/infilling end
19X-2	ER	45	138.15	0.839	4.195	
19X-2	ER	65	138.35	0.865	4.325	
19X-2	ER	85	138.55	0.82	4.100	
19X-2	ER	105	138.75	0.853	4.265	
19X-2	ER	125	138.95	0.868	4.340	
19X-2	ER	145	139.15	0.901	4.505	
19X-3	ER	10	139.30	0.861	4.305	
19X-3	ER	30	139.50	0.97	4.850	
19X-3	ER	51	139.71	0.757	3.785	
19X-3	ER	71	139.91	0.766	3.830	
19X-4	ER	7	140.77	0.785	3.925	
19X-4	ER	24	140.94	0.76	3.800	
19X-4	ER	45	141.15	0.87	4.350	
19X-4	ER	65	141.35	0.826	4.130	Dark organic-rich layer
19X-4	ER	77	141.47	0.944	4.720	
20X-1	ER	30	146.10	0.715	3.575	
20X-1	ER	50	146.30	0.802	4.010	
20X-1	ER	75	146.55	0.8	4.000	

Table 15. Wenner array electrical resistivity and formation factor results for Hole NGHP-01-15A. (To view the complete table, please see the ASCII files.)—Continued

Core, section	Sample	Top (cm)	Depth (mbsf)	Electrical resistivity (W×m)	Apparent formation factor	Comments
NGHP-01-15A—Continued						
20X-1	ER	95	146.75	0.706	3.530	
20X-1	ER	115	146.95	0.802	4.010	
20X-1	ER	130	147.10	0.766	3.830	
20X-2	ER	15	147.45	0.859	4.295	
20X-2	ER	35	147.65	0.944	4.720	
20X-2	ER	55	147.85	0.872	4.360	
20X-2	ER	75	148.05	0.752	3.760	
20X-2	ER	95	148.25	0.8	4.000	
20X-2	ER	115	148.45	0.94	4.700	
20X-2	ER	135	148.65	0.856	4.280	
20X-3	ER	15	148.95	0.803	4.015	
20X-3	ER	35	149.15	0.785	3.925	
20X-3	ER	55	149.35	0.747	3.735	
20X-4	ER	15	150.45	0.803	4.015	
20X-4	ER	35	150.65	0.805	4.025	
20X-4	ER	55	150.85	0.821	4.105	
20X-4	ER	75	151.05	0.827	4.135	
20X-4	ER	95	151.25	0.777	3.885	
20X-4	ER	115	151.45	0.735	3.675	
20X-4	ER	135	151.65	0.82	4.100	
20X-5	ER	15	151.95	1.1	5.500	
20X-5	ER	42	152.22	1.361	6.805	
20X-5	ER	60	152.40	0.928	4.640	
20X-5	ER	89	152.69	0.953	4.765	
21X-1	ER	15	155.55	0.829	4.145	
21X-1	ER	35	155.75	0.93	4.650	
21X-1	ER	55	155.95	0.853	4.265	
21X-1	ER	80	156.20	0.901	4.505	
21X-1	ER	100	156.40	1.013	5.065	
21X-1	ER	120	156.60	0.912	4.560	
21X-2	ER	26	157.16	0.996	4.980	
21X-2	ER	84	157.74	1.089	5.445	
21X-2	ER	100	157.90	1.127	5.635	
21X-2	ER	125	158.15	1.089	5.445	
21X-3	ER	15	158.55	0.92	4.600	
21X-3	ER	35	158.75	0.882	4.410	
21X-3	ER	55	158.95	0.965	4.825	
21X-4	ER	15	160.05	1.221	6.105	
21X-4	ER	35	160.25	0.977	4.885	
21X-4	ER	55	160.45	1.013	5.065	
21X-4	ER	75	160.65	1.079	5.395	
21X-4	ER	100	160.90	1.025	5.125	
21X-4	ER	120	161.10	0.902	4.510	
21X-4	ER	140	161.30	0.999	4.995	
21X-5	ER	15	161.55	0.853	4.265	
21X-5	ER	40	161.80	1.025	5.125	
21X-5	ER	60	162.00	0.973	4.865	
21X-5	ER	80	162.20	1.204	6.020	
21X-5	ER	100	162.40	1	5.000	
21X-5	ER	120	162.60	0.894	4.470	
21X-6	ER	15	163.05	1.023	5.115	
21X-6	ER	35	163.25	1.081	5.405	
21X-6	ER	55	163.45	0.981	4.905	
21X-6	ER	90	163.80	1.039	5.195	
21X-7	ER	15	164.05	1.062	5.310	

Table 15. Wenner array electrical resistivity and formation factor results for Hole NGHP-01-15A. (To view the complete table, please see the ASCII files.)—Continued

Core, section	Sample	Top (cm)	Depth (mbsf)	Electrical resistivity (W×m)	Apparent formation factor	Comments
NGHP-01-15A—Continued						
21X-7	ER	35	164.25	0.997	4.985	
21X-7	ER	55	164.45	1.185	5.925	
22X-1	ER	25	165.25	0.878	4.390	
22X-1	ER	54	165.54	0.891	4.455	
22X-1	ER	75	165.75	0.882	4.410	
22X-1	ER	97	165.97	0.852	4.260	
22X-1	ER	125	166.25	1.022	5.110	
22X-2	ER	33	166.83	0.97	4.850	
22X-2	ER	61	167.11	0.866	4.330	
22X-2	ER	83	167.33	0.924	4.620	
22X-2	ER	100	167.50	0.978	4.890	
22X-2	ER	118	167.68	1.051	5.255	
22X-4	ER	20	168.80	1.135	5.675	
22X-4	ER	40	169.00	0.991	4.955	
22X-4	ER	60	169.20	0.926	4.630	
22X-4	ER	80	169.40	0.911	4.555	
22X-4	ER	104	169.64	0.992	4.960	
22X-4	ER	134	169.94	0.968	4.840	
22X-5	ER	25	170.35	1.054	5.270	
22X-5	ER	40	170.50	0.859	4.295	
22X-5	ER	64	170.74	1.071	5.355	
22X-5	ER	88	170.98	1.161	5.805	
22X-5	ER	130	171.40	0.964	4.820	
22X-6	ER	17	171.77	1.446	7.230	
22X-6	ER	37	171.97	1.127	5.635	
22X-6	ER	53	172.13	0.969	4.845	
23X-2	ER	16	174.97	1.057	5.285	
23X-2	ER	35	175.16	1.131	5.655	
23X-2	ER	60	175.41	0.977	4.885	
23X-2	ER	80	175.61	1.086	5.430	
23X-2	ER	100	175.81	1.046	5.230	
23X-2	ER	120	176.01	1.043	5.215	
23X-3	ER	15	176.46	1.216	6.080	
23X-3	ER	35	176.66	1.019	5.095	
23X-3	ER	55	176.86	0.886	4.430	
23X-4	ER	15	177.96	1.143	5.715	
23X-4	ER	34	178.15	0.991	4.955	
23X-4	ER	55	178.36	0.987	4.935	
23X-4	ER	75	178.56	0.962	4.810	
23X-4	ER	95	178.76	0.919	4.595	
23X-4	ER	127	179.08	1.008	5.040	
23X-5	ER	20	179.51	0.852	4.260	
23X-5	ER	40	179.71	0.864	4.320	
23X-5	ER	60	179.91	0.944	4.720	
23X-5	ER	80	180.11	0.857	4.285	
23X-5	ER	100	180.31	0.96	4.800	
23X-5	ER	125	180.56	0.957	4.785	
23X-6	ER	15	180.96	1.099	5.495	
23X-6	ER	35	181.16	0.834	4.170	
23X-6	ER	55	181.36	0.86	4.300	
23X-6	ER	73	181.54	1.007	5.035	
23X-6	ER	100	181.81	1.189	5.945	
23X-6	ER	120	182.01	0.795	3.975	
23X-7	ER	15	182.39	1.099	5.495	
23X-7	ER	35	182.59	0.826	4.130	
23X-7	ER	55	182.79	0.801	4.005	

Table 15. Wenner array electrical resistivity and formation factor results for Hole NGHP-01-15A. (To view the complete table, please see the ASCII files.)—Continued

Core, section	Sample	Top (cm)	Depth (mbsf)	Electrical resistivity (W×m)	Apparent formation factor	Comments
NGHP-01-15A—Continued						
23X-7	ER	75	182.99	1.305	6.525	
23X-7	ER	94	183.18	1.048	5.240	
24X-1	ER	20	184.40	1.071	5.355	
24X-1	ER	35	184.55	1.373	6.865	
24X-1	ER	55	184.75	0.949	4.745	
24X-1	ER	75	184.95	0.769	3.845	
24X-1	ER	95	185.15	0.839	4.195	
24X-1	ER	115	185.35	1.195	5.975	
24X-2	ER	15	185.85	1.052	5.260	
24X-2	ER	35	186.05	0.931	4.655	
24X-2	ER	55	186.25	0.895	4.475	
24X-2	ER	75	186.45	1.021	5.105	
24X-2	ER	95	186.65	0.955	4.775	
24X-2	ER	131	187.01	0.847	4.235	
24X-3	ER	15	187.35	0.799	3.995	
24X-3	ER	35	187.55	0.773	3.865	
24X-3	ER	66	187.86	1.084	5.420	
24X-3	ER	66	187.86	0.794	3.970	
24X-4	ER	15	188.85	1.086	5.430	
24X-4	ER	35	189.05	1.015	5.075	
24X-4	ER	55	189.25	1.057	5.285	
24X-4	ER	77	189.47	1.026	5.130	
24X-4	ER	102	189.72	1.04	5.200	
24X-4	ER	120	189.90	1.078	5.390	
24X-4	ER	140	190.10	1.035	5.175	
24X-5	ER	15	190.35	0.962	4.810	
24X-5	ER	35	190.55	1.161	5.805	
24X-5	ER	55	190.75	1.008	5.040	
24X-5	ER	75	190.95	0.944	4.720	
24X-5	ER	95	191.15	0.891	4.455	
24X-5	ER	115	191.35	0.984	4.920	
24X-5	ER	132	191.52	1.151	5.755	
24X-6	ER	15	191.85	1.132	5.660	
24X-6	ER	35	192.05	0.963	4.815	
24X-6	ER	65	192.35	0.989	4.945	
24X-6	ER	92	192.62	0.92	4.600	
24X-7	ER	15	192.85	1.209	6.045	
24X-7	ER	35	193.05	1.003	5.015	
24X-7	ER	55	193.25	1.258	6.290	
25X-1	ER	15	193.95	0.855	4.275	
25X-1	ER	35	194.15	0.907	4.535	
25X-1	ER	53	194.33	0.963	4.815	
25X-1	ER	76	194.56	0.881	4.405	
25X-1	ER	95	194.75	0.8	4.000	
25X-1	ER	118	194.98	0.854	4.270	
25X-1	ER	136	195.16	0.882	4.410	
25X-2	ER	15	195.45	0.901	4.505	
25X-2	ER	36	195.66	0.841	4.205	
25X-2	ER	55	195.85	0.894	4.470	
25X-2	ER	70	196.00	0.9	4.500	
25X-3	ER	15	196.95	0.78	3.900	
25X-3	ER	35	197.15	0.822	4.110	
25X-3	ER	55	197.35	0.978	4.890	
25X-3	ER	75	197.55	0.794	3.970	
25X-3	ER	96	197.76	0.89	4.450	
25X-3	ER	109	197.89	0.827	4.135	

P-Wave Velocity

P-wave velocity (V_p) measured with the MSCL increased slightly from 1.49 km/s in the top of the hole (fig. 22) to 1.55 km/s at a subbottom depth of 32 m, which represents the depth where gas and voids present in the sediment prevented further valid measurements from being logged. The contact V_p values of 1.48 to 1.55 km/s (table 16) are in agreement with the MSCL values at the top of the hole. Valid contact V_p measurements could not be determined below 30.45 mbsf. Both techniques are adversely affected by the SMI located at about 31.5 mbsf (see "Organic Geochemistry"). Methane, which is typically produced below the SMI, may come out of solution if present in a high enough concentration and attenuate acoustic signals.

Magnetic Susceptibility

Wide excursions exist in the magnetic susceptibility data indicating that primary and secondary magnetic minerals are present in alternating non-uniform high and low frequency layers (fig. 22; see "Lithostratigraphy"). The trend of increasing magnetic susceptibility with depth in the middle of the core helps define the physical property unit boundaries at 80 and 133 mbsf.

Thermal Conductivity

Thermal conductivities vary between 0.679 and 1.067 W/(m×K) and decrease slightly with subbottom depth (table 17 and fig. 22). Such values are well within the range of marine sediments (for example, Novosel and others, 2007), although they are all lower than values determined by Davis and others (1990) for sediment from Cascadia and the Nankai Trough.

Downhole Temperature Measurements

A number of different tools are available for determining downhole sediment temperature (see "Physical Properties" in "Methods" chapter). Although five attempts were made, only four provided usable *in situ* temperature data at Site NGHP-01-15, and two of those measurements are only of fair quality. Seafloor temperature intercept was determined to be 7.7 ± 0.3 °C and the geothermal gradient was determined to be 40 ± 2 °C per km (fig. 26 and table 18). The base of the gas-hydrate stability zone is predicted at 125 mbsf assuming pure methane and porewater salinity of 35 ppt (Sloan, 1998), which is the same as the observed BSR depth (shipboard-calculated seafloor temperature 7.7 °C, geothermal gradient 39 °C per km).

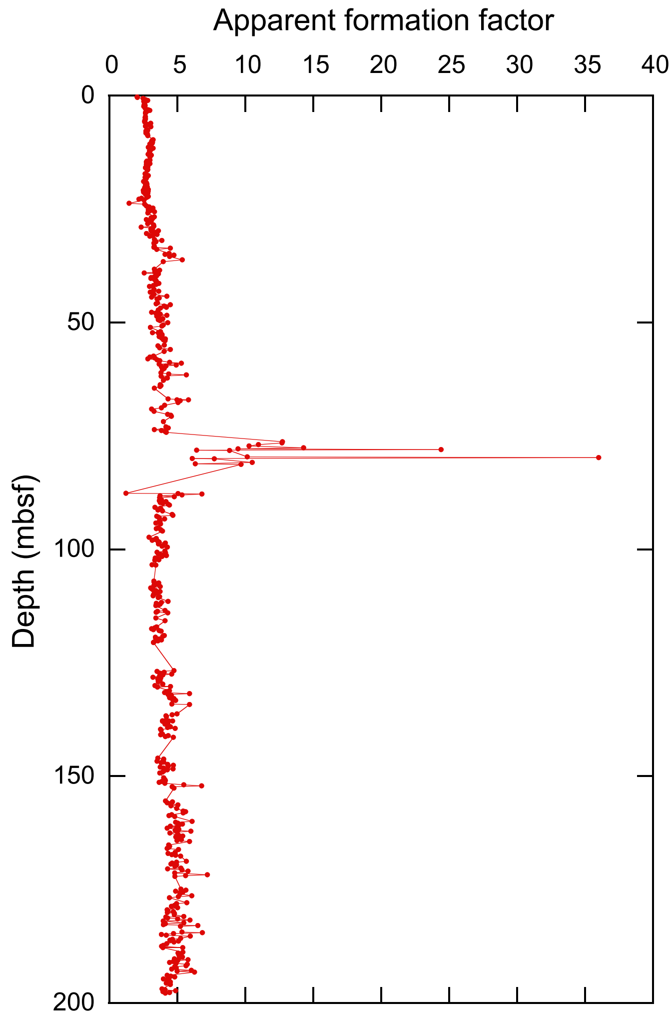

Figure 25. Apparent formation factor versus subbottom depth for Hole NGHP-01-15A.

Pressure Coring

The main objectives of pressure coring during NGHP Expedition 01 were to quantify natural gas composition and concentration in sediments and to determine the nature and distribution of gas hydrate and free gas within the sediment matrix. Secondary objectives were to obtain measurements of physical properties on gas-hydrate-bearing sediments under in-situ conditions, which can be used to help interpret regional seismic data, and obtain samples under full pressure for shorebased studies. To achieve these objectives, we conducted depressurization experiments and captured resultant gas to calculate gas-hydrate quantity, made nondestructive measurements (X-ray imaging, *P*-wave velocity, gamma density) at *in situ* pressures and during depressurization to examine gas-hydrate habit within sediments, and archived gas-hydrate-bearing sediments at *in situ* pressures for more comprehensive investigations on shore.

Table 16. Contact *P*-wave velocity results determined on split cores sections from Hole NGHP-01-15A.

Core, section	Sample	Top (cm)	Depth (mbsf)	Vp (km/s)
		NGHP-01-15A		
1H-1	VP	118	1.18	1.492
1H-2	VP	30	1.8	1.484
1H-3	VP	92	3.92	1.488
1H-4	VP	95	5.45	1.492
1H-5	VP	55	6.55	1.499
1H-6	VP	115	8.65	1.504
1H-7	VP	22	9.22	1.505
2H-1	VP	35	9.95	1.510
2H-2	VP	55	11.65	1.514
2H-3	VP	55	13.15	1.510
2H-4	VP	35	14.45	1.501
2H-5	VP	35	15.95	1.502
2H-6	VP	15	17.25	1.496
2H-7	VP	15	18.75	1.488
3H-1	VP	15	19.25	1.502
3H-2	VP	35	20.95	1.522
3H-3	VP	15	22.25	1.504
3H-4	VP	15	23.75	1.504
3H-5	VP	15	25.25	1.520
3H-6	VP	15	26.75	1.537
3H-7	VP	40	28.5	1.553
4H-1	VP	40	29	1.529
4H-2	VP	35	30.45	1.522

The BSR at Site NGHP-01-15, located in the Krishna-Godavari Basin, has an estimated depth of 126 mbsf. Site NGHP-01-15 is situated at the toe of a slope where slumps and slides may have deposited material and near a possible fault. There were no LWD data for this site.

Pressure Core Operations and Measurements

Pressure coring tools were deployed four times at Site NGHP-01-15 (table 19); two PCS cores and two FPC cores. Figures 27 and 28 show the pressure and temperature history of the cores during deployment, coring, recovery, and chilling (in the ice shuck) of the pressure coring tools. Figures 29, 30, and show the measurements made on the two successful cores at full pressure, during depressurization, and during repressurization. Figures 32 and 33 show the gas and fluid released from the successful cores and the character of the pressure decrease during depressurization.

Core NGHP-01-15A-11Y (86.7 mbsf) retrieved a full core (0.85 m) at near *in situ* pressure (table 19). The core was transferred to the MSCL-P and X-ray images, gamma density and *P*-wave velocity measurements were collected (fig. 29A). Core NGHP-01-15A-11Y had a zone of strongly layered low density from 62 to 74 cm and a drop in *P*-wave velocity, signifying possible free gas, at 37 cm. Before the core was depressurized, the pressure was first increased to investigate the velocity of the sediment at 37 cm, since the high velocity of a gas-hydrate layer could have been masked by exsolved gas. At 200 bar, the gas was forced back into solution but the velocity was similar to the surrounding sediment (fig. 31). Core NGHP-01-15A-11Y was depressurized in the MSCL–P, where gas evolved at 37–40 cm, near the original low velocities, and also within layer of low density at about 70 cm. After the depressurization, the layer near 37 cm had lowered in density by 0.4 g/cm^3 more than any other section of sediment. This core released 3.68 liters of methane, corresponding to 0.9 percent methane hydrate as a percent of pore volume or 9.2 mL of methane hydrate (table 20). A final MSCL–P scan was collected at atmospheric pressure which showed an intact core but with much lower density (fig. 30A). When the core was split, the low-density zone originally at 62–74 cm (now at 75–83 cm) was found to be a woody turbidite, accounting for the extremely light X-ray image of this zone. The layer near 37 cm that evolved gas during depressurization (now at 39–44 cm) was found to be a clean sand layer. Three salinity and chlorinity measurements were made on this core: one in the clay above the clean sand (26–39 cm, 33 ppt, no chlorinity), one in the clean sand (39–44 cm, 25 ppt, 436.4 mM), and one in the sand layer directly above the woody material (72–75 cm, 33 ppt, 537.0 mM). The clean sand showed a clear freshening signal compared to the two other measurements in the core, as well as other measurements in nearby XCB cores (see “Inorganic Geochemistry”).

Table 17. Thermal conductivity results for Hole NGHP-01-15A.

Core, section	Sample	Top (cm)	Depth (mbsf)	Thermal conductivity (W/[m×K])
		NGHP-01-15A		
1H-3	TC	55	3.55	0.948
2H-7	TC	32	18.92	0.897
3H-1	TC	75	19.85	0.943
3H-3	TC	55	22.65	0.921
3H-7	TC	30	28.40	0.992
4H-1	TC	75	29.35	1.017
4H-6	TC	45	36.55	1.031
5H-1	TC	78	38.88	1.031
5H-3	TC	59	41.69	0.945
5H-7	TC	17	47.27	0.927
6H-1	TC	72	48.32	0.941
6H-3	TC	73	51.12	0.835
7H-3	TC	20	60.21	1.067
7H-6	TC	62	64.24	0.911
8H-1	TC	75	67.35	0.879
8H-3	TC	17	69.56	0.938
9X-4	TC	35	79.88	0.762
12X-3	TC	50	91.20	0.877
13X-3	TC	75	101.05	0.861
14X-3	TC	55	110.45	0.880
17X-3	TC	80	119.69	0.946
18X-3	TC	50	130.10	0.944
19X-1	TC	45	136.65	0.973
20X-3	TC	40	149.20	0.936
21X-3	TC	40	158.80	0.679
22X-4	TC	75	169.35	0.956
23X-4	TC	75	178.56	0.937
24X-5	TC	75	190.95	0.978
25X-1	TC	75	194.55	0.879

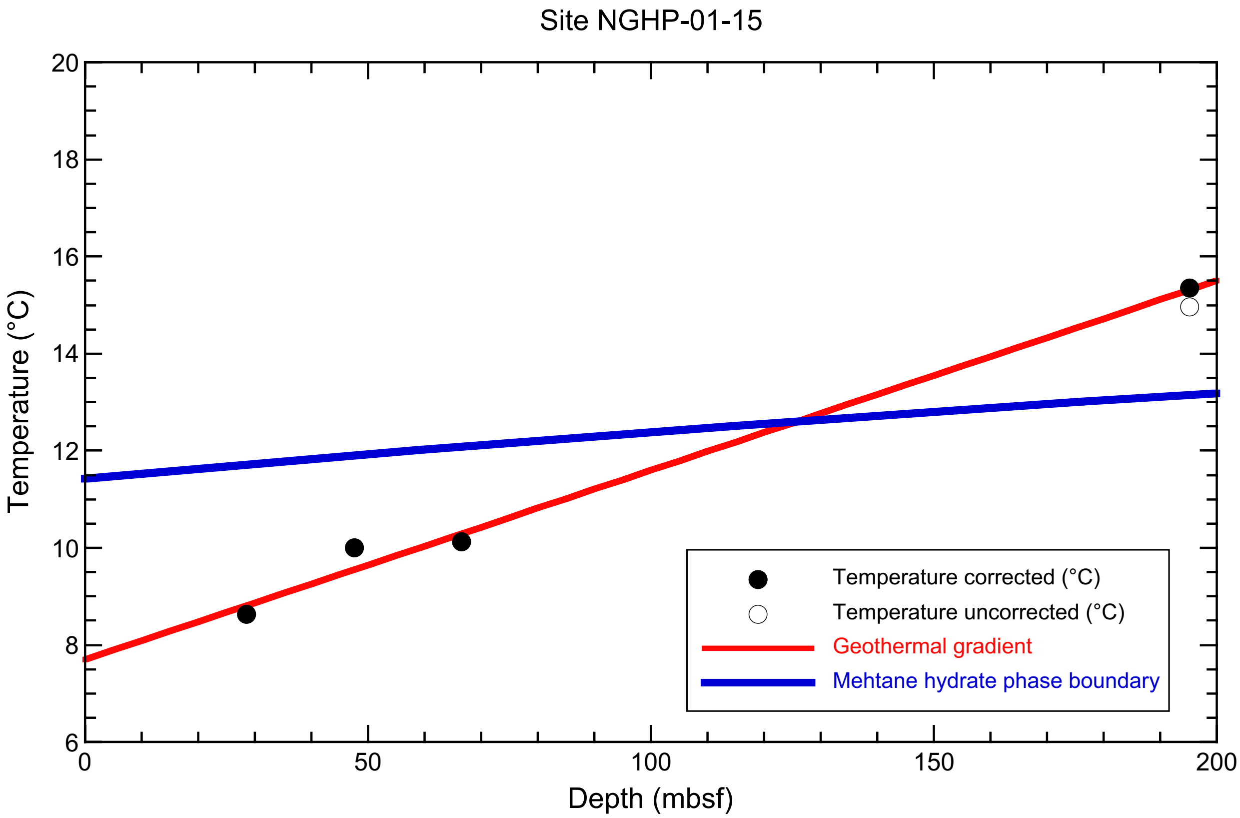

Figure 26. Geothermal gradient and estimated depth to the BSR from *in situ* temperature measurements for Hole NGHP-01-15A. [BSR, bottom-simulating reflector]

Table 18. *In situ* temperature estimates for Site NGHP-01-15.

Depth (mbsf)	Core	Assumed thermal conductivity (W/m×K)	Tool	Temperature (°C)	Ad-hoc calibration correction	Corrected temperature (°C)	Estimated uncertainty	Data quality
28.5	A03H	0.95	APCT-3	8.63	0	8.63	0.15	Fair
47.6	A05H	0.95	APCT-3	10	0	10	0.06	Good
66.6	A07H	0.95	APCT-3	10.12	0	10.12	0.06	Good
137.6	A18X	0.95	DVTP	N/A	0.50	N/A	N/A	Poor
195.2	A24X	0.95	DVTP	14.96	0.50	15.35	0.15	Fair-good

Table 19. Summary of pressure-coring operations at Site NGHP-01-15.

Core ID	Top of core (mbsf)	Length recovered (cm)*	Length curated (cm)*	Pressure at core depth (bar)	Pressure recovered (bar)			Comments
					logged**		gauge***	
					NGHP-01-15			
10P	85.7	0	0	103	72		70	Normal operation
11Y	86.7	85	84	103	96		97	Normal operation
15P	115.0	--	88	106	7		--	No pressure; data logger offset by 6–7 bar
16Y	116.0	86	91	106	89	@10 °C	85	Tool data logger offset by 10–15 bar

Notes:

Water depth at Site NGHP-01-15 is 938 m. P=PCS, Y=FPC, E=HRC.

*Length measured from X-ray and gamma density analysis, which may not match curated core length.

**Last pressure recorded before data logger disconnected from corer autoclave. Temperature 2–4 °C unless otherwise noted.

***Pressure measured when autoclave pressure transducer connected to external gauge. Pressure measured at 7 °C unless otherwise noted.

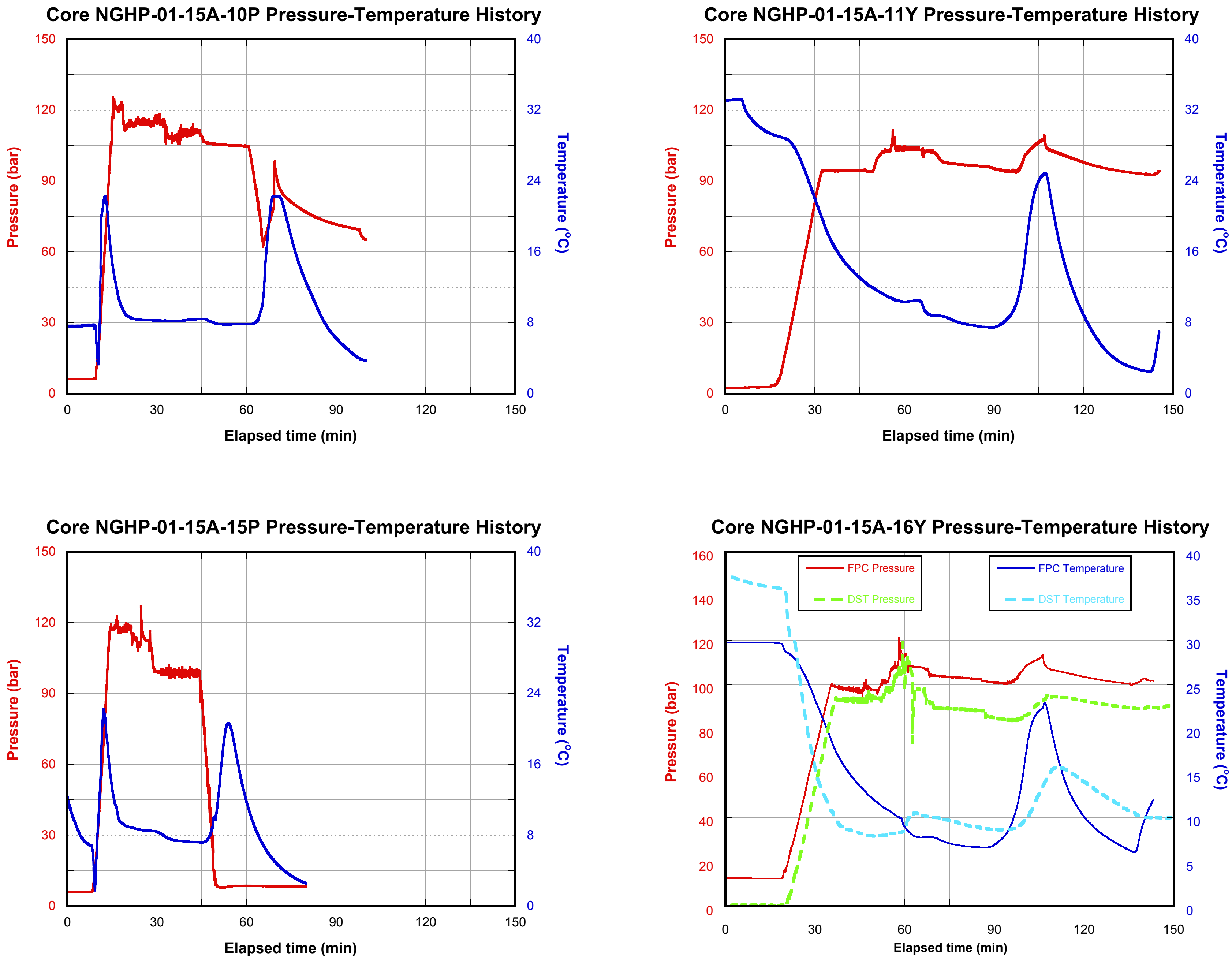

Figure 27. Temperature and pressure versus elapsed time for each pressure corer deployment as recorded by the corer's internal data logger.

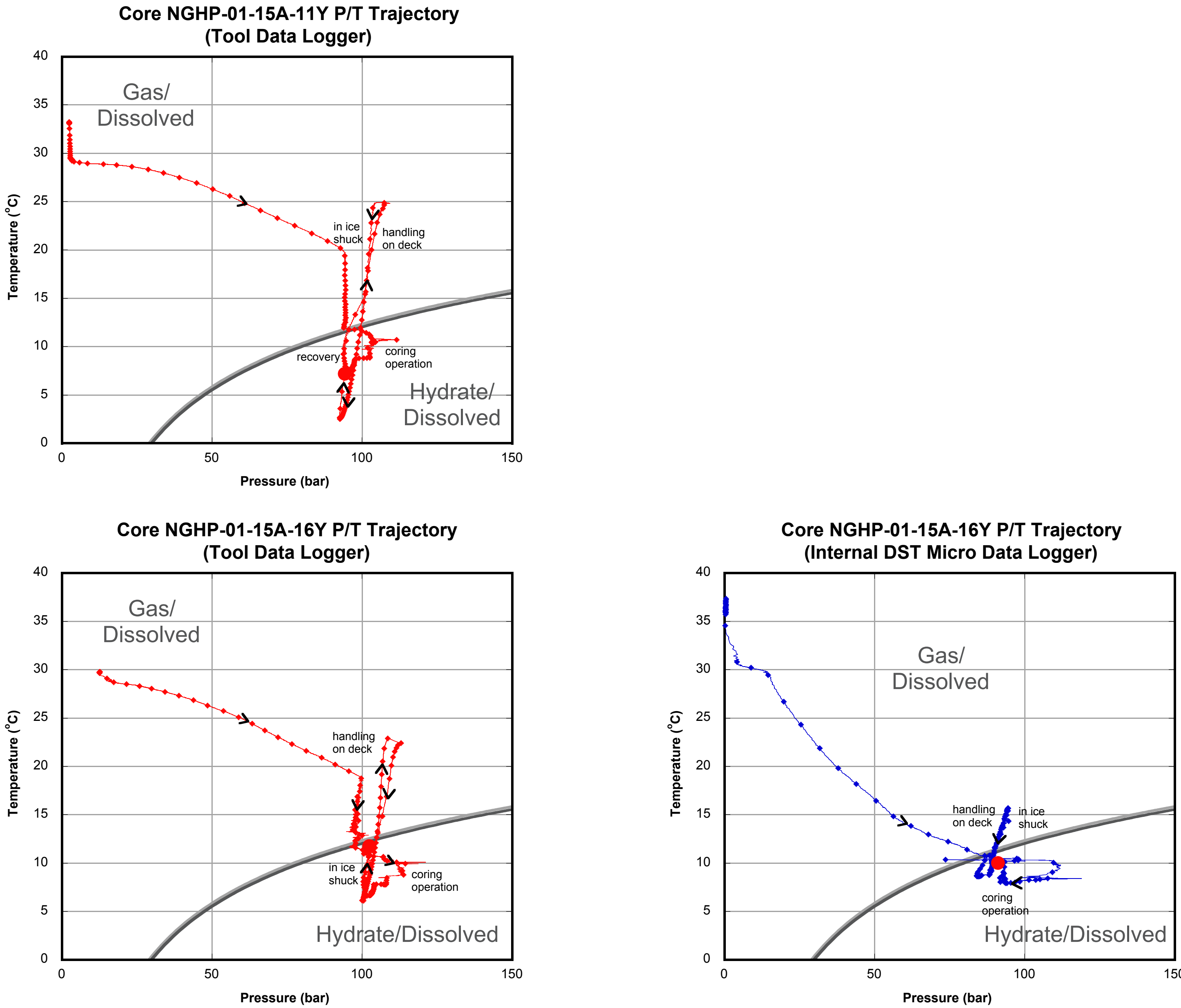

Figure 28. Temperature versus pressure for each successful pressure corer deployment, showing trajectories relative to gas hydrate stability at 30 ppt and 35 ppt salinity, calculated from Xu (2002, 2004). Small dots are approximately every minute. Large dot is final temperature and pressure of autoclave prior to data logger removal.

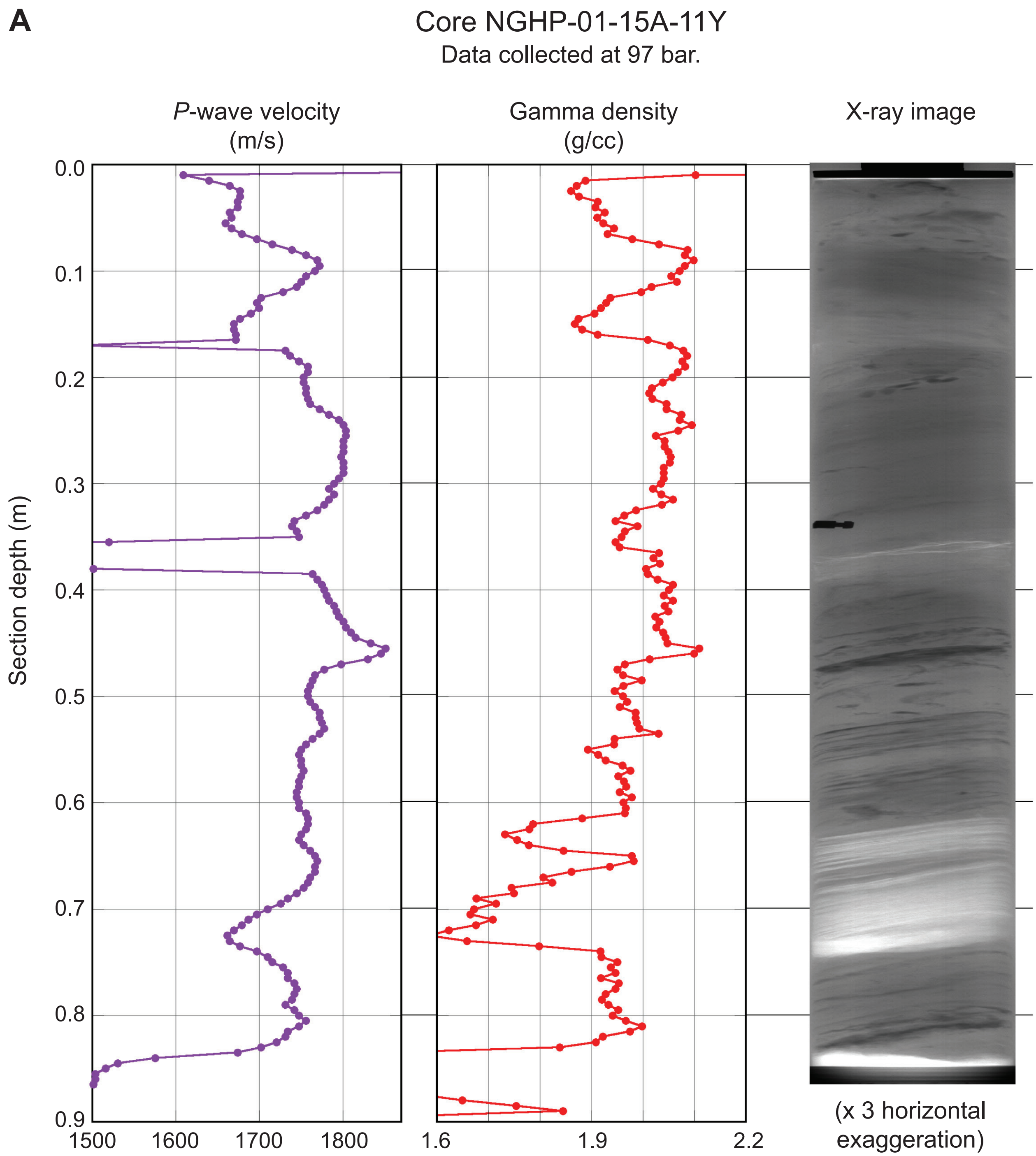

Figure 29. Data collected at near *in situ* pressure and 7 °C for Cores NGHP-01-15A-11Y and -16Y, including X-ray images, gamma density, and P-wave velocity. X-ray images have been stretched 300 percent in the cross-core direction to show detail.

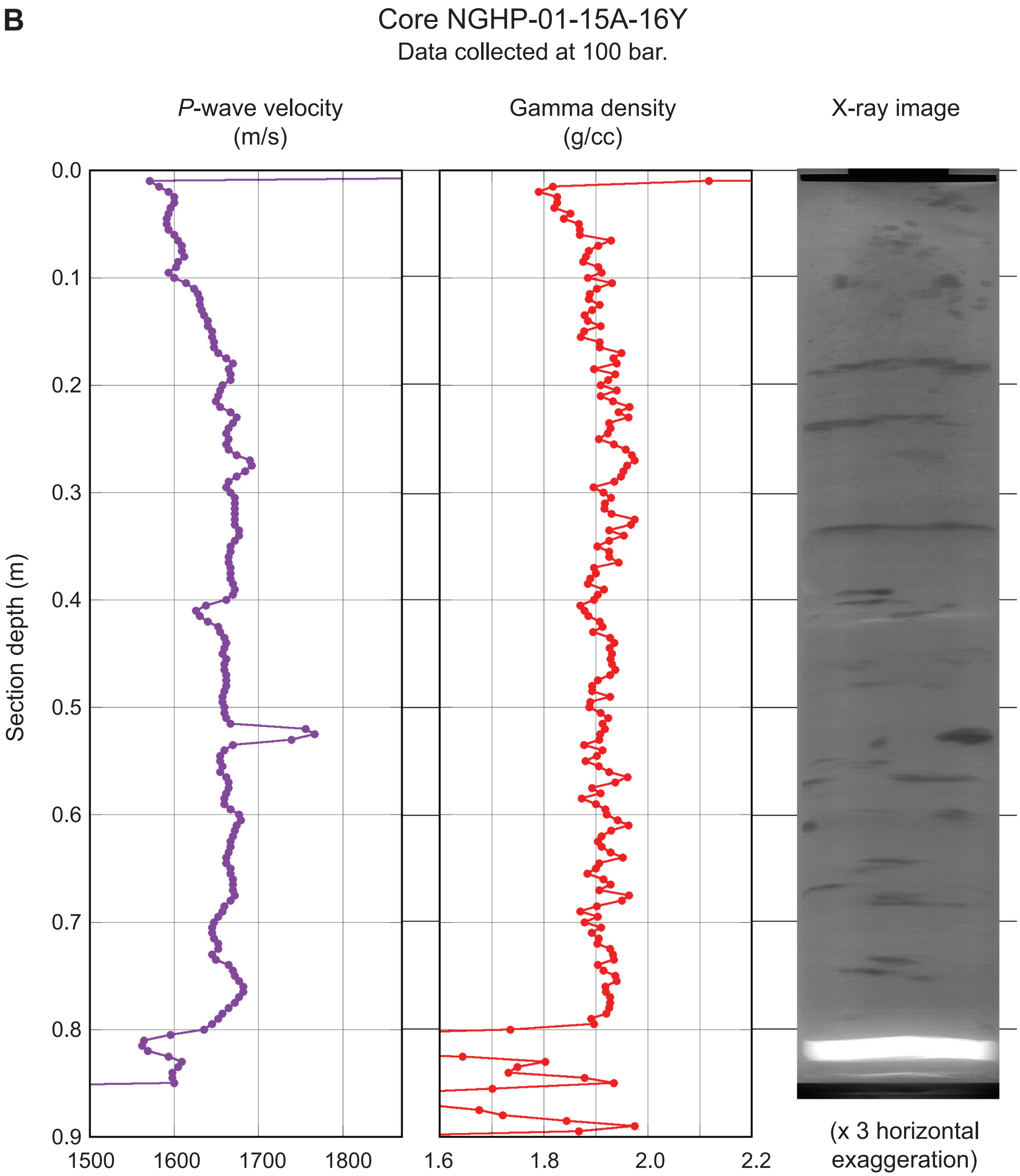

Figure 29. Data collected at near *in situ* pressure and 7 °C for Cores NGHP-01-15A-11Y and -16Y, including X-ray images, gamma density, and P-wave velocity. X-ray images have been stretched 300 percent in the cross-core direction to show detail.—Continued

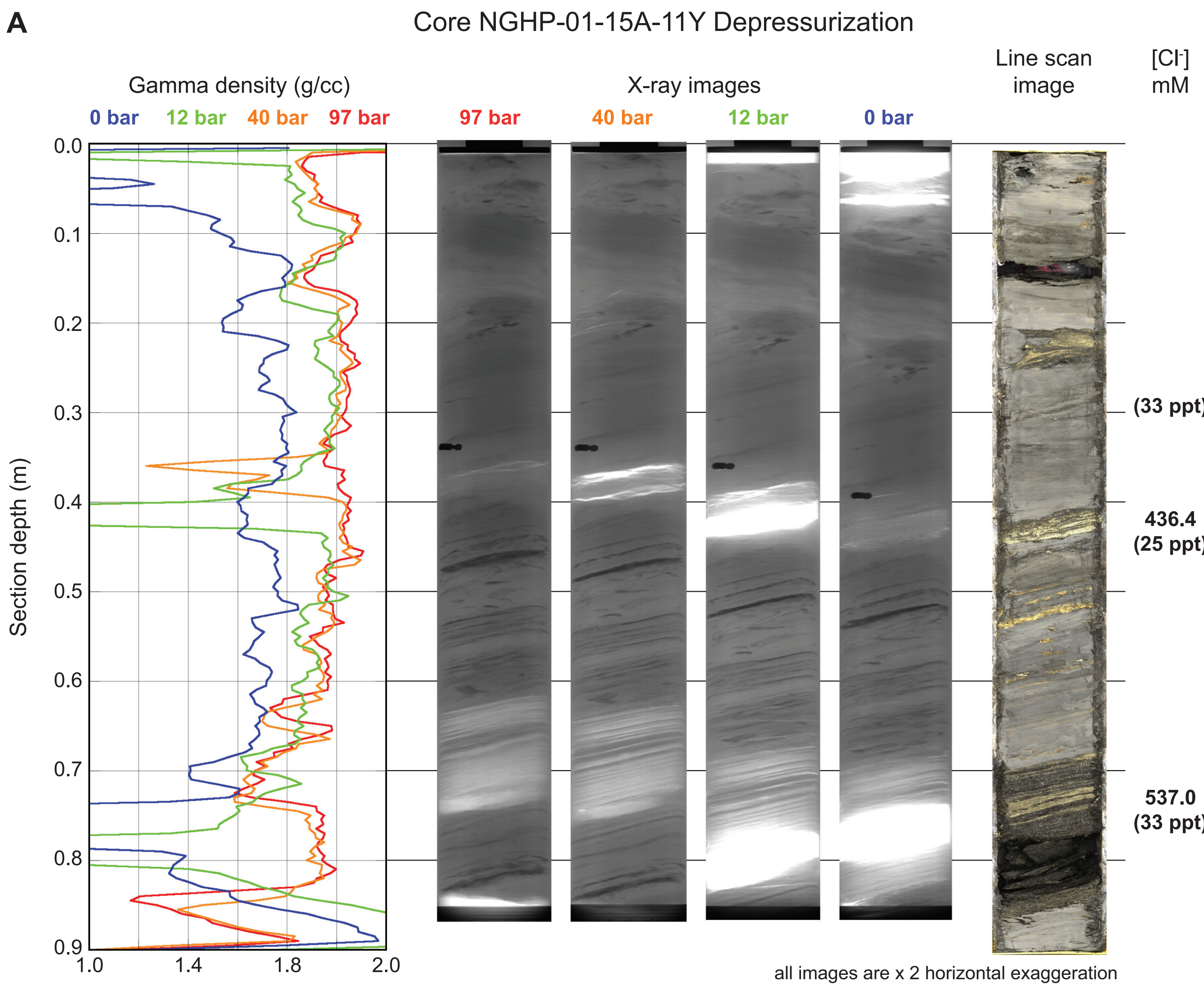

Figure 30. Summary of data taken on Cores NGHP-01-15A-11Y and -16Y before, during, and after depressurization, including gamma density profiles collected before and after depressurization, X-ray images collected before and after depressurization, and line scan images collected after depressurization. Salinity data (in ppt) are included with chlorinity data for Core NGHP-01-15A-11Y. Arrow on Core NGHP-01-15A-16Y shows very hard carbonate nodule that correlated with high P-wave velocity measurement.

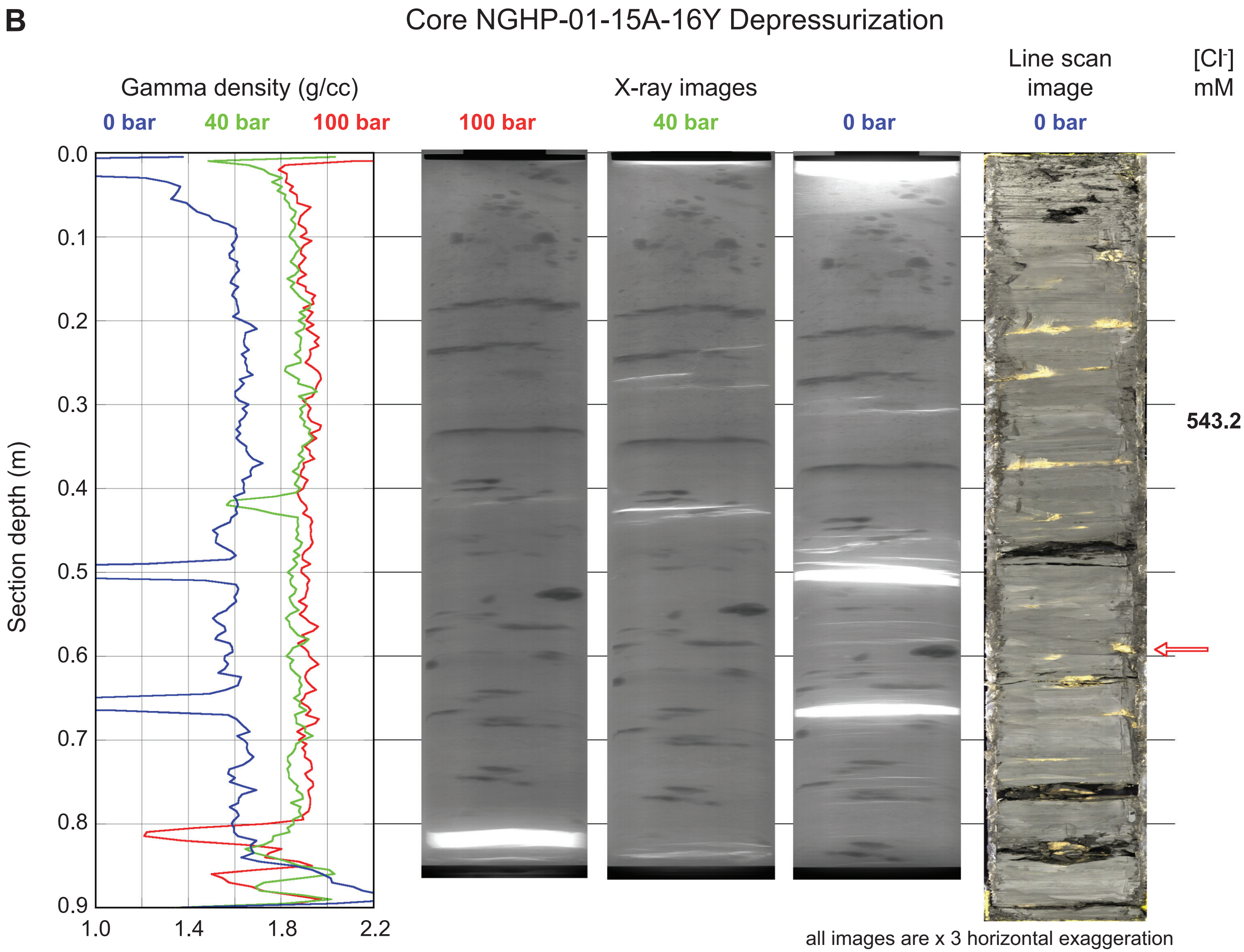

Figure 30. Summary of data taken on Cores NGHP-01-15A-11Y and -16Y before, during, and after depressurization, including gamma density profiles collected before and after depressurization, X-ray images collected before and after depressurization, and line scan images collected after depressurization. Salinity data (in ppt) are included with chlorinity data for Core NGHP-01-15A-11Y. Arrow on Core NGHP-01-15A-16Y shows very hard carbonate nodule that correlated with high P-wave velocity measurement.—Continued

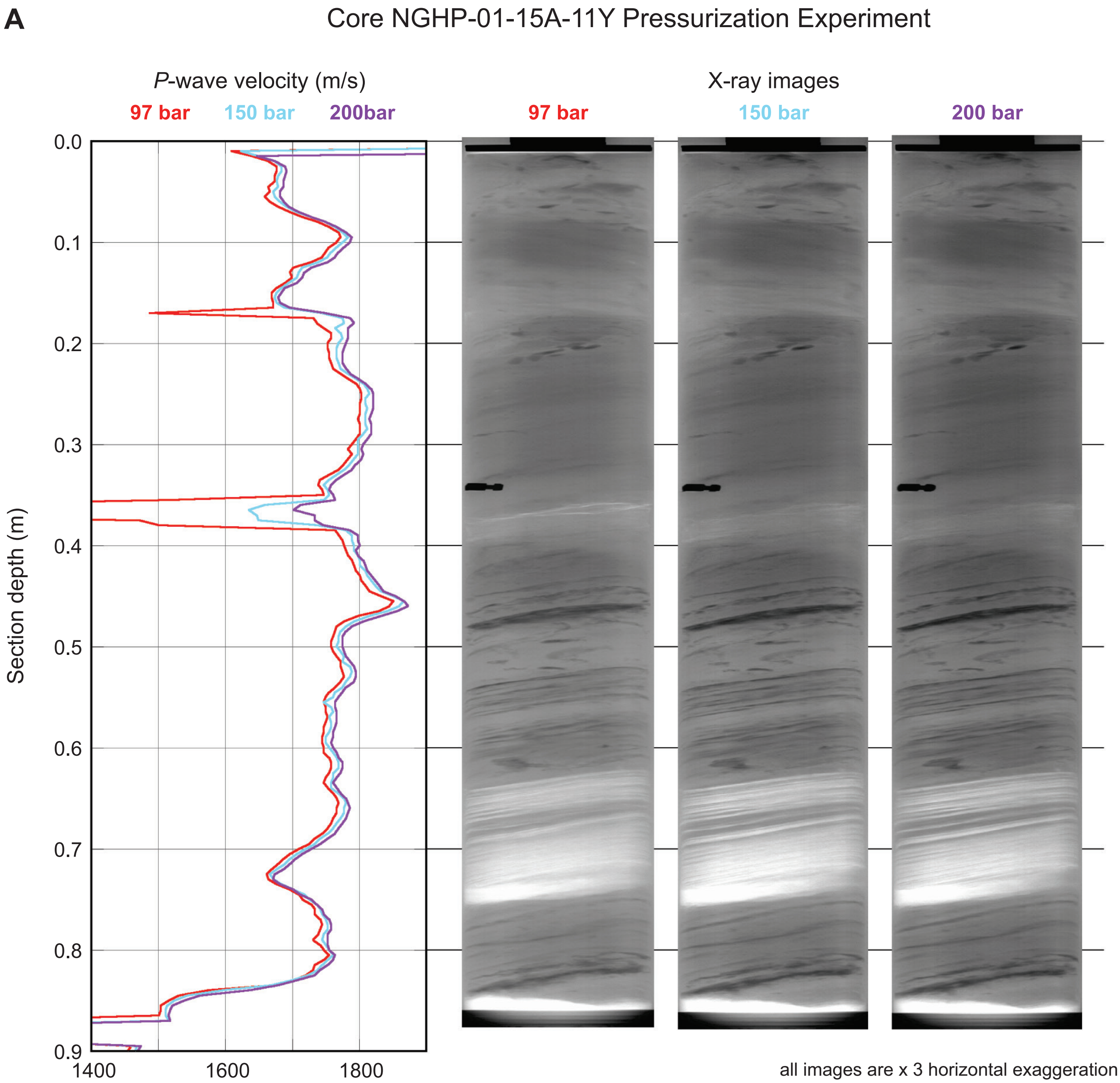

Figure 31. Summary of data taken on Cores NGHP-01-15A-11Y and -16Y at pressures higher than *in situ* pressure, including P-wave velocity profiles collected before and after pressurization and X-ray images collected before and after pressurization. Data on Core NGHP-01-15A-11Y were collected before any depressurization. Data on Core NGHP-01-15A-16Y were collected after full depressurization.

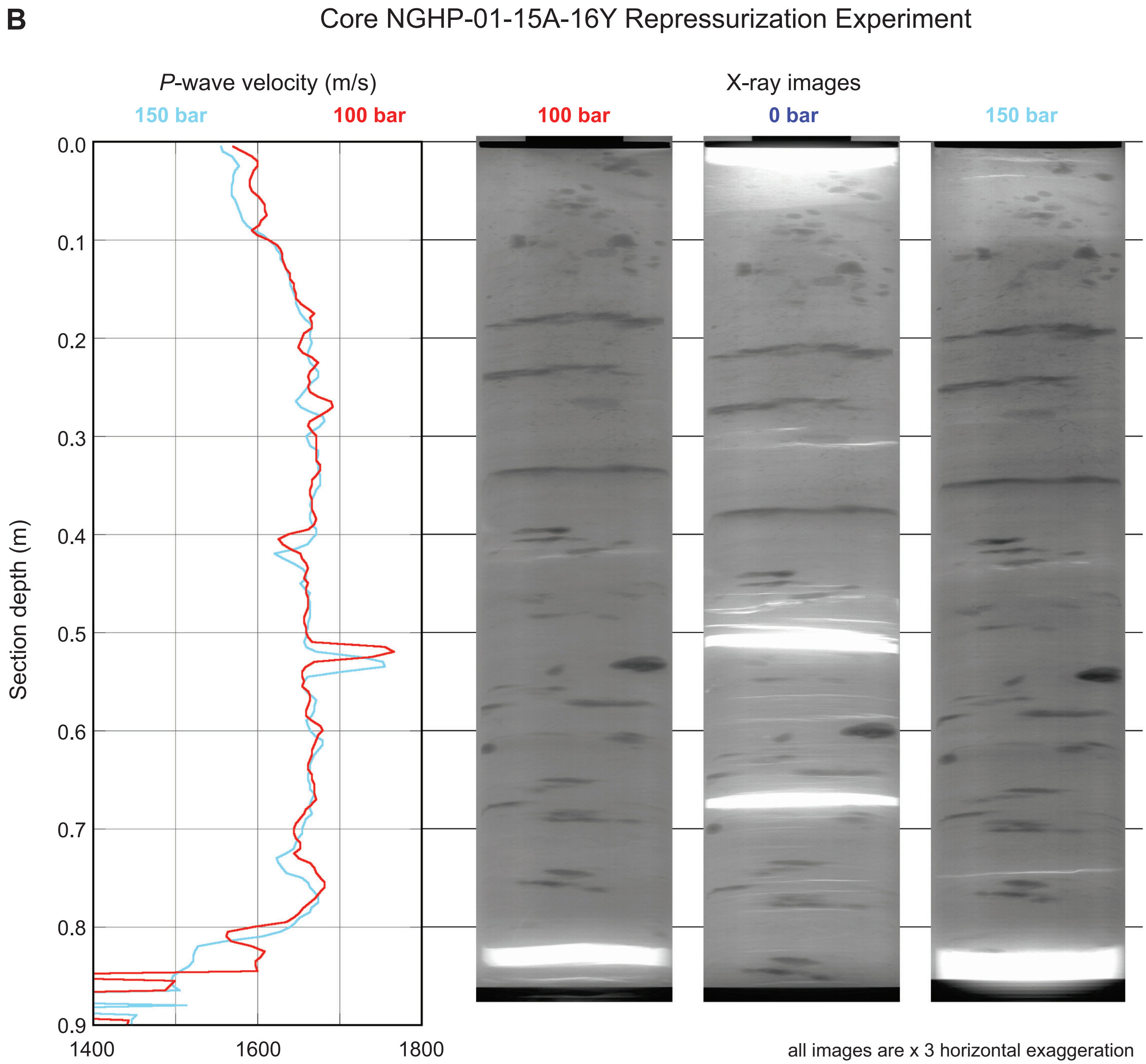

Figure 31. Summary of data taken on Cores NGHP-01-15A-11Y and -16Y at pressures higher than *in situ* pressure, including P-wave velocity profiles collected before and after pressurization and X-ray images collected before and after pressurization. Data on Core NGHP-01-15A-11Y were collected before any depressurization. Data on Core NGHP-01-15A-16Y were collected after full depressurization.—Continued

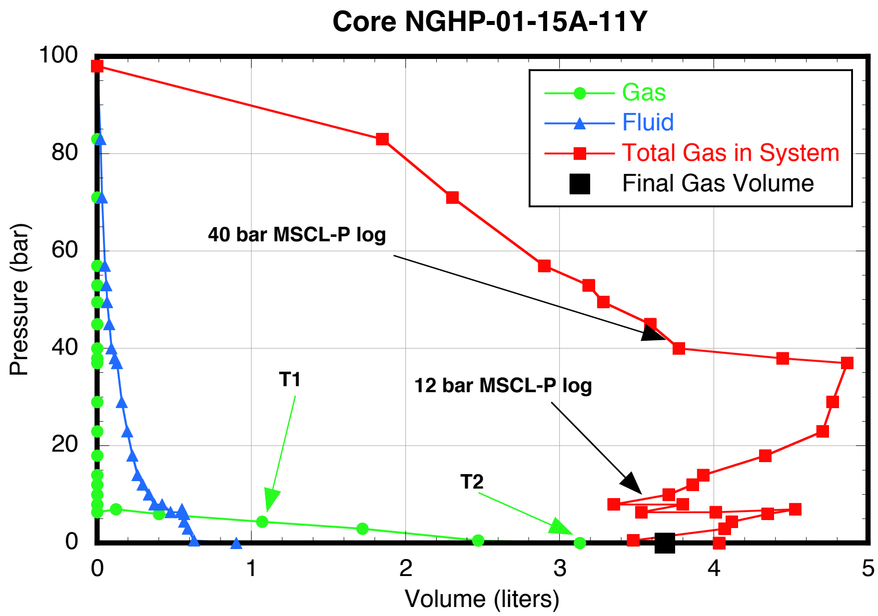

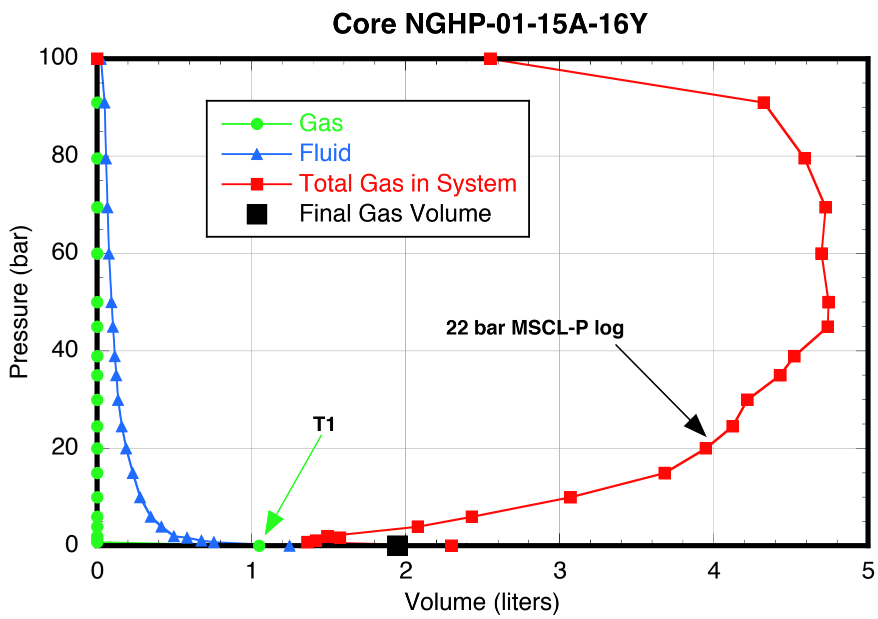

Figure 32. Pressure versus volume for successful pressure cores at Site NGHP-01-15, also showing placement of intermediate X-ray or gamma density scans and gas samples (see "Organic Geochemistry"). [Green circles, gas; blue triangles, fluid volume; red squares, total gas volume in system (calculated as described in the "Methods" chapter); large black square, final calculated gas from cores; T (number), gas samples]

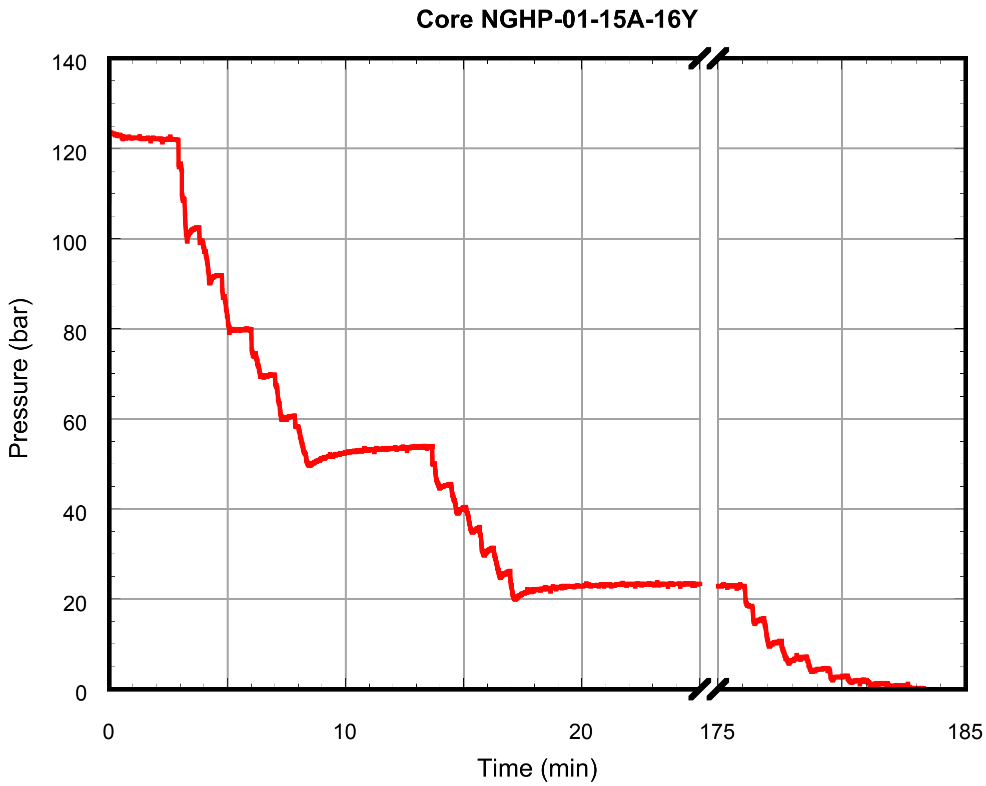

Figure 33. Pressure versus time for the depressurization of Core NGHP-01-15A-16Y.

Table 20. Methane hydrate volume and concentration in pore space for successful pressure cores at Site NGHP-01-15. Values required for calculation of methane hydrate concentration are also included.

Parameter	Units	NGHP-01-15A-11Y	NGHP-01-15A-11Y (5 cm-thick sand layer)	NGHP-01-15A-16Y
Core diameter	mm	57	57	57
Sediment length	cm	85	85	86
Sediment porosity	%	45	45	47
Pore volume	*liters*	*0.971*	*0.971*	*1.035*
Volume methane collected	liters	3.65	3.65	1.83
Methane concentration in pore fluids	mM	0.1	0.1	0.8
Total methane in core	*mmol*	*160.0*	*160.0*	*84.8*
In situ salinity	ppt	33.5	33.5	33.5
Methane saturation*	mM	94.2	94.2	107.9
Methane in pore fluids, assuming saturation	*mmol*	*91.4*	*91.4*	*67.5*
Excess methane	*mmol*	*67.5*	*67.5*	*–31.3*
Volume of methane hydrate	*ml*	*9.2*	*9.2*	*0.0*
Methane hydrate, % of pore volume	*%*	*0.9***	*16.1*	*0***

Notes:

Rows in italics are calculated parameters.

*Methane saturation calculated from Xu (2002, 2004) using a water depth of 938 mbsl, a thermal gradient of 39 °C/km, a seafloor temperature of 7.73 °C, and the above salinities.

**Assuming all gas hydrate is evenly distributed throughout the pore space.

Core NGHP-01-15A-16Y (116 mbsf), collected just above the BSR (129 mbsf), retrieved a full core (0.88 m) at pressure (table 19). This core was not chilled quickly as the ice shuck was not full of ice, and spent half an hour outside of the gas-hydrate stability zone, which was longer than usual (fig. 28). Core NGHP-01-15A-16Y was transferred to the MSCL–P and X-ray images, gamma density and *P*-wave velocity measurements were collected (fig. 29B). The X-ray image revealed a core with many high density lumps and layers which were shown to be carbonate layers and nodules (compare the X-ray image at one atmosphere with the line scan image of the split core; fig. 30B). There was a solitary high *P*-wave velocity spike at a depth of 52 cm. This core released 1.95 liters of methane, which, if uniformly distributed, infers that this core was undersaturated in methane at *in situ* temperature and pressure (table 20). The lack of pressure plateaus or rebounds in the pressure-volume or pressure-time profiles supports this conclusion (figs. 32 and 33). To test the possibility that the velocity spike was caused by localized gas-hydrate cementation in an otherwise undersaturated core, the core was repressurized following the complete degassing process and logged again (fig. 31B). If the *P*-wave velocity spike observed in this core had been caused by gas-hydrate cementation, then it would not have been present when the core was repressurized with seawater. The velocity spike remained after depressurization (fig. 31B), and it was concluded that the velocity spike was caused by a very hard and prominent nodule of carbonate found at that location when the core was split and which is also shown clearly on the X-ray image (52 cm before depressurization, 59 cm after depressurization). One chlorinity measurement was made on this core (29–38 cm, 543.2 mM), which was similar to background chlorinities at this depth.

Gas-Hydrate Concentration, Nature, and Distribution from Pressure Coring

Two of the four pressure cores at Site NGHP-01-15 were recovered at sufficient pressures to accurately assess the total concentration of methane and hence the predicted amount of gas hydrate. The calculated methane concentration for these cores is shown in figure 34 in relation to the phase boundaries for Structure I methane hydrate. (All pressure cores released nearly pure methane with less than 60 ppm ethane, confirming Structure I methane hydrate; see “Organic Geochemistry”). Below the BSR and base of gas-hydrate stability there was a zone of elevated resistivity (130–155 mbsf) seen in the wire-line resistivity logs (see “ Downhole Logging”), but both of the successful cores were above the base of gas-hydrate stability and hence there is no information from pressure coring on the possible existence of free gas in the zone of elevated resistivity below the BSR.

Estimates of gas-hydrate concentration from chlorinity measurements and pressure coring differ in scale and are, therefore, not always the same. For instance, Core NGHP-01-15A-11Y was calculated to have an average gas-hydrate concentration of 0.9 percent of pore volume from methane mass balance calculations, but the gas-hydrate concentrations calculated from freshening in the interstitial water samples taken in the same core vary from 0 percent to 18 percent (see “Inorganic Geochemistry”). These two data sets are complementary, not contradictory. If all 9.2 mL of gas hydrate in Core NGHP-01-15A-11Y was considered to be concentrated in the clean sand layer (5 cm), the gas-hydrate saturation of this layer was calculated to have been 16 percent of pore space. Therefore samples taken to examine porewater freshening can be best utilized when supporting information is available so that hypotheses concerning gas-hydrate nature and habitat can be tested.

Core NGHP-01-15A-11Y reflects the distribution of gas hydrate in Hole NGHP-01-15A in miniature. The only distinct thermal anomaly with low chlorinity was found in Core NGHP-01-15A-09X (the XCB core above Core NGHP-01-15A-11Y) in a sand layer, but many other sand layers in this hole did not appear to contain gas hydrate. Two sand layers within Core NGHP-01-15A-11Y were examined for the presence of gas hydrate; though the two layers were less than 50 cm apart, one showed a gas-hydrate saturation of 15–20 percent of pore space and one showed no gas-hydrate presence at all, based on chlorinity measurements and methane mass balance guided by nondestructive measurements. Lack of increased *P*-wave velocity in the gas-hydrate-rich sand layer was a mystery. Even more mysterious is the mechanism by which gas hydrate was distributed between these closely-spaced layers. One-dimensional, vertical models of gas-hydrate formation cannot explain such distribution. Lateral transport within some thin (5 cm) layers but not others could be possible, with the proximity of the seismically-imaged fault.

Core NGHP-01-15A-16Y contained no gas hydrate. Not only did it provide evidence that the sediment above the BSR was slightly undersaturated in methane, but it also provided a tie point for chlorinity measurements. The chlorinity measurement on Core NGHP-01-15A-16Y represented background chlorinity, and the similarity to surrounding chlorinities showed that there was little to no low-level disseminated gas hydrate lowering the apparent background chlorinity in the sediment column (see “Inorganic Geochemistry”).

Downhole Logging

Operations

Drilling operations in Hole NGHP-01-15A were completed when the last core was recovered from 1,137.9 mbrf (200 mbsf) at 0700 hr on July 14, 2006. The hole was conditioned with a 40 bbl mud sweep and a full wiper trip. After a second 20 bbl mud sweep, a go-devil was sent to open the lockable flapper valve above the bit, the hole was displaced with 60 bbl of Sepiolite, and the pipe was brought to logging depth of 1,002 mbrf (64 mbsf). At 1045 hr the wire line was spooled and the logging equipments were brought to the rig floor to prepare for logging.

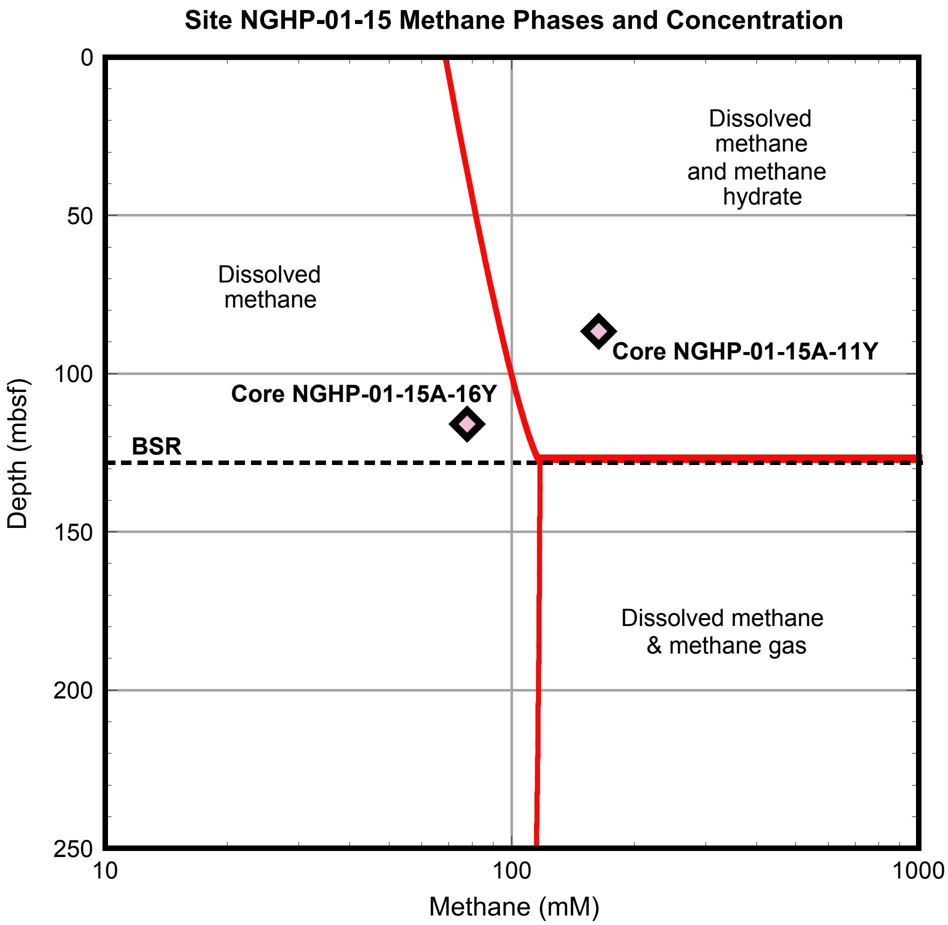

Figure 34. Methane phase diagram for Site NGHP-01-15, with total methane concentration measured from the three successful pressure cores at Site NGHP-01-15. The shipboard-calculated seafloor temperature (7.73 °C) and thermal gradient (39 °C/km) were taken from "Downhole Temperature Measurements" in "Physical Properties," the salinities were the average background salinity around the depths of the pressure cores (35 ppt; from table 4), and methane saturation was calculated according to Xu (2002, 2004).

Assembly of the triple combo string started at 1135 hr, the tool was complete at 1200 hr, and was run into hole (RIH) at 1220 hr after insertion of the source for the hostile litho-density sonde (see "Downhole Logging" in the "Methods" chapter). The tool string reached the bit at 1307 hr and was fully in open hole at 1313 hr with only limited sticking from the formation. There was no problem getting to the total depth of 1,140 mbrf where the up log started at 1330 hr. At 1342 hr the pipe was raised to 992 mbrf, in order to be able to log as much as possible through some hydrate-rich layers identified from the cores at ~70–75 mbsf. At 1353 hr, with the bottom of the tool string at 1028 mbrf, the caliper was closed and the WHC was turned off before entering the pipe. The string was completely inside the pipe at 1403 hr and the pass was concluded at 1415 hr when the gamma ray log identified the seafloor at 939 mbrf. The triple combo was back on the rig floor at 1450 hr, and rigged down at 1525 hr.

Assembly of the FMS/Sonic followed immediately. The tool string was complete at 1600 hr, RIH at 1610 hr and cleared the bit without problem at 1655 hr. The total depth of 1,140 mbrf was again reached without problem at 1710 hr, when the first pass started, with the DSI configured for the following acquisition modes: low frequency monopole, low frequency upper dipole, standard frequency lower dipole and stoneley mode. The pipe was raised to 992 mbrf at 1715 hr and the calipers were closed before trying to enter the pipe at 1733 hr, with the bottom of the string at 1,034 mbrf. As the entry proved difficult after a few attempts, we decided not to try any further on this first pass, for fear of not being able to exit again for a second pass, and the pass was concluded at 1745 hr, with the bottom of the tool at 1,024 mbrf. The tool was sent back down for a second pass, hoping to log the high resistivity interval immediately below the pipe at the end this pass. It reached one more time the bottom of the hole at 1758 hr, and the second pass started with the DSI configured for low frequency monopole and cross-dipole modes. At 1825 hr, the FMS calipers were closed at 1034 mbrf and the WHC was turned off to re-enter the pipe. Reentry proved difficult and it was necessary to lower and rotate the pipe by 180° to be able to get the top of the tool inside the pipe at 1832 hr. The second pass was concluded at 1835 hr, when the tool string was fully inside the pipe, after successfully recording some sharp velocity changes in the hydrate layer immediately below the drill bit. The tool string was back on the rig floor at 1930 hr, disassembled at 2015 hr, and the rig floor was ready to pull out of the hole at 2050 hr.

Logging Data Quality

Figure 35 shows the main logs recorded with the triple combo in Hole NGHP-01-15A. The hole size calculated from the HLDS caliper (see “Downhole Logging” in the “Methods” chapter) shows that the hole was irregular, with several washouts and a few ledges. However the tool never lost contact with the formation and most of the data should be only moderately affected by the irregular hole size. This is confirmed by the good agreement between the density log and the density measurements made on core samples shown in the same track. The only interval where log density values are occasionally lower than core data, a common indicator of poor log quality, is between ~100 and 120 mbsf, where several low-density excursions coincide with washouts. Surprisingly, one of the intervals with noticeable differences between log- and core-derived density is where the hole was the most regular and in gauge with the drill bit, between ~130 and 150 mbsf. Considering the good quality of the hole and the coincidence in this interval of higher resistivity and lower neutron porosity, as well as low core recovery, we consider that the density log is more reliable than the core data in this interval.

The density porosity was calculated from the density log and from the grain density measured on core samples, by using at each depth the grain density from the closest sample. Hence the good agreement between the density-porosity log and the porosity measurements from core samples is a direct consequence of the good agreement in the density data. The neutron porosity is consistently higher than the other porosity estimates because of the influence of mineral-bound water in these clay-dominated sediments.

The hole size calculated from the FMS caliper logs in figure 36 shows that the hole remained in good condition during the FMS/Sonic run, which is confirmed in the same figure by the strong amplitude and coherence of the monopole waveforms over most of the interval logged, despite uniformly low V_P values. However, the dipole waveforms show that between ~100 and 125 mbsf the shear velocity was too low for the flexural waves to be properly captured by the recording time window and further processing was required to derive reliable V_s logs in this interval.

Logging Units

The trends in the main logs displayed in figures 35 and 36 (particularly in the density, resistivity and velocity logs) allow the definition of three logging units with distinct characteristics:

Logging unit 1 (55–132 mbsf) is most clearly defined by the resistivity and the velocity logs, which show generally high values with significant variability above ~110 mbsf, and decrease gradually with depth below. Some of the highest resistivity values correspond to intervals were gas hydrate was identified with infrared images and recovered in the core (see below). With the caliper closed above 80 mbsf, density readings above this depth are not reliable. Below this depth, the density log decreases with depth, before increasing below 110 mbsf. The gamma ray log follows the same trend, suggesting that these changes are mostly due to lithology and the occurrence of sandy layers. Some of the lower density values might result from the larger hole size generally measured by the caliper in this unit.

The top of Logging unit 2 (132–200 mbsf) is defined by a sharp increase in density, velocity and resistivity at 132 mbsf. The V_P and the V_s log generally display higher values through this unit than in Logging unit 1, particularly between 132 and 145 mbsf. Below the initial increase at 132 mbsf, all the logs display higher values between 132 and 145 mbsf and decrease slightly with depth below. The changes in the main logs at 132 mbsf also coincide with an increase in gamma ray, which then decreases slightly with depth through the unit. This suggests that it is a lithological or structural boundary, whose depth is coincident with the predicted depth of the BSR (see “Background and Objectives”). The increase in density and velocity measured at this depth should generate a positive polarity reflector, opposite to the interpreted BSR (see “Background and Objectives”), and further synthetic seismogram modeling will be necessary to understand the actual nature of this reflector.

Gas-Hydrate and Free Gas Occurrence

As previously discussed (see “Downhole Logging” in the “Methods” chapter), the presence of gas hydrate is generally identified by increases in electrical resistivity and acoustic velocity that are not accompanied by a corresponding density increase. The relatively high resistivity values measured above 110 mbsf while density tends to decrease suggest that some gas hydrate is present above this depth. The highest resistivity values between ~175 and 179 mbsf correspond to a core (Core NGHP-01-15A-09X) where strong temperature anomalies were measured with the infrared camera and gas-hydrate samples were recovered (see “Physical Properties”)

To make a quantitative estimate of the amount of gas hydrate present, we followed the procedure described in “Downhole Logging” in the “Methods” chapter, to apply the Archie relationship to the resistivity and porosity logs recorded in Hole NGHP-01-15A. Because no LWD logs were recorded in this site, we used the wire-line resistivity logs to make this estimate. The procedure and the results are illustrated in figure 37. The pore fluid resistivity (R_w) was estimated from Fofonoff (1985) using a temperature profile derived from a linear fit of the *in situ* temperature measurements at Site NGHP-01-15 (7.73 °C at the seafloor; gradient of 39 °C/km, see “Physical Properties”) and a constant water salinity of 33 ppt, which is an average of the values measured on interstitial pore water samples in this hole. The estimated *m* curve was derived from R_w, the porosity (φ) and resistivity (R_t) logs ($m_{est} = -\log F/\log\varphi$, where $F = R_t/R_w$). As this relationship is defined for water-saturated sediments, the chosen value of $m = 2.1$ is given by

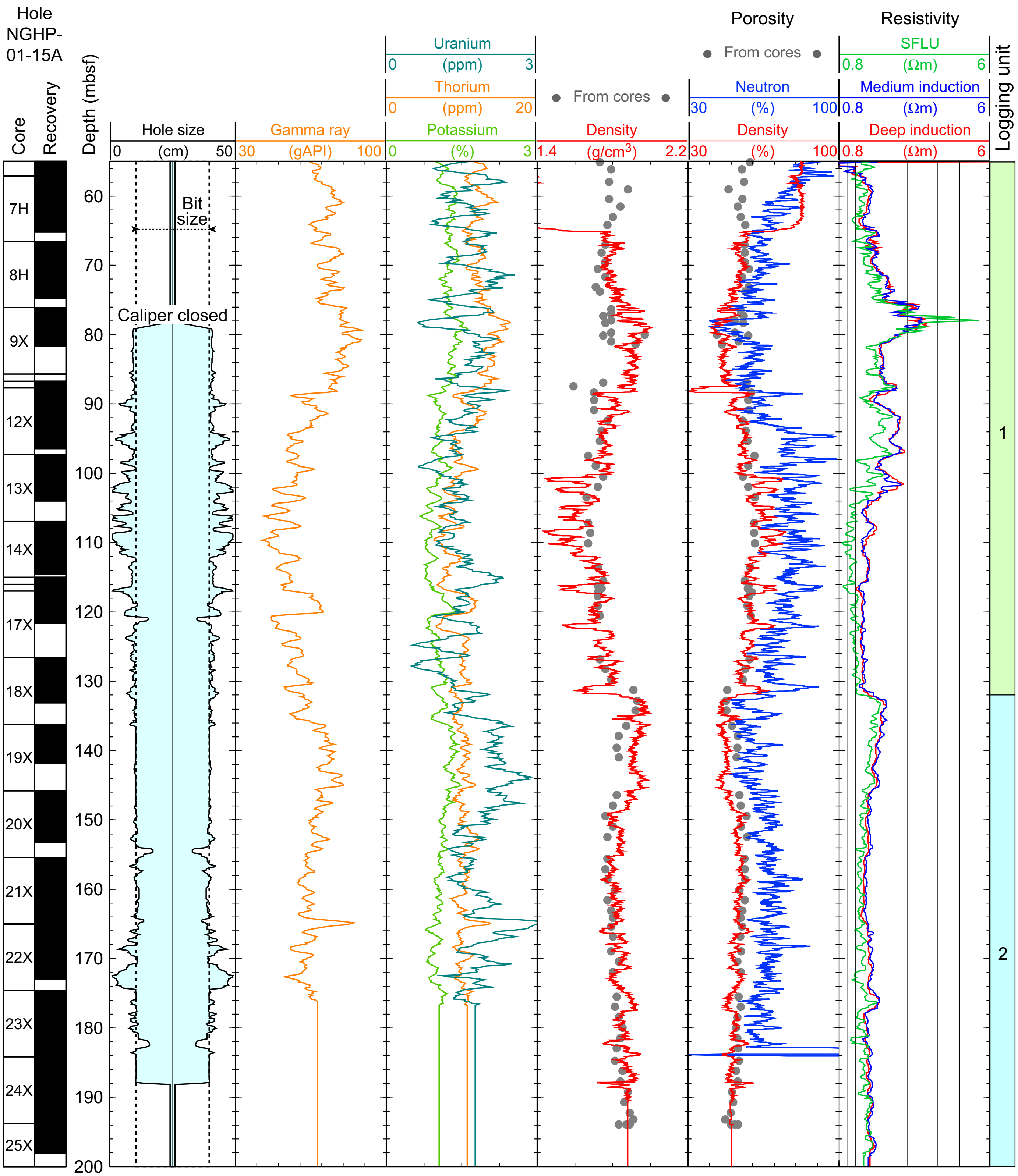

Figure 35. Summary of the wireline logs recorded in Hole NGHP-01-15A. The hole size is calculated from the Hostile Litho Density Sonde (HLDS) caliper. The density and porosity measurements made on core samples are shown for comparison. [SFLU, spherically focused unaveraged resistivity]

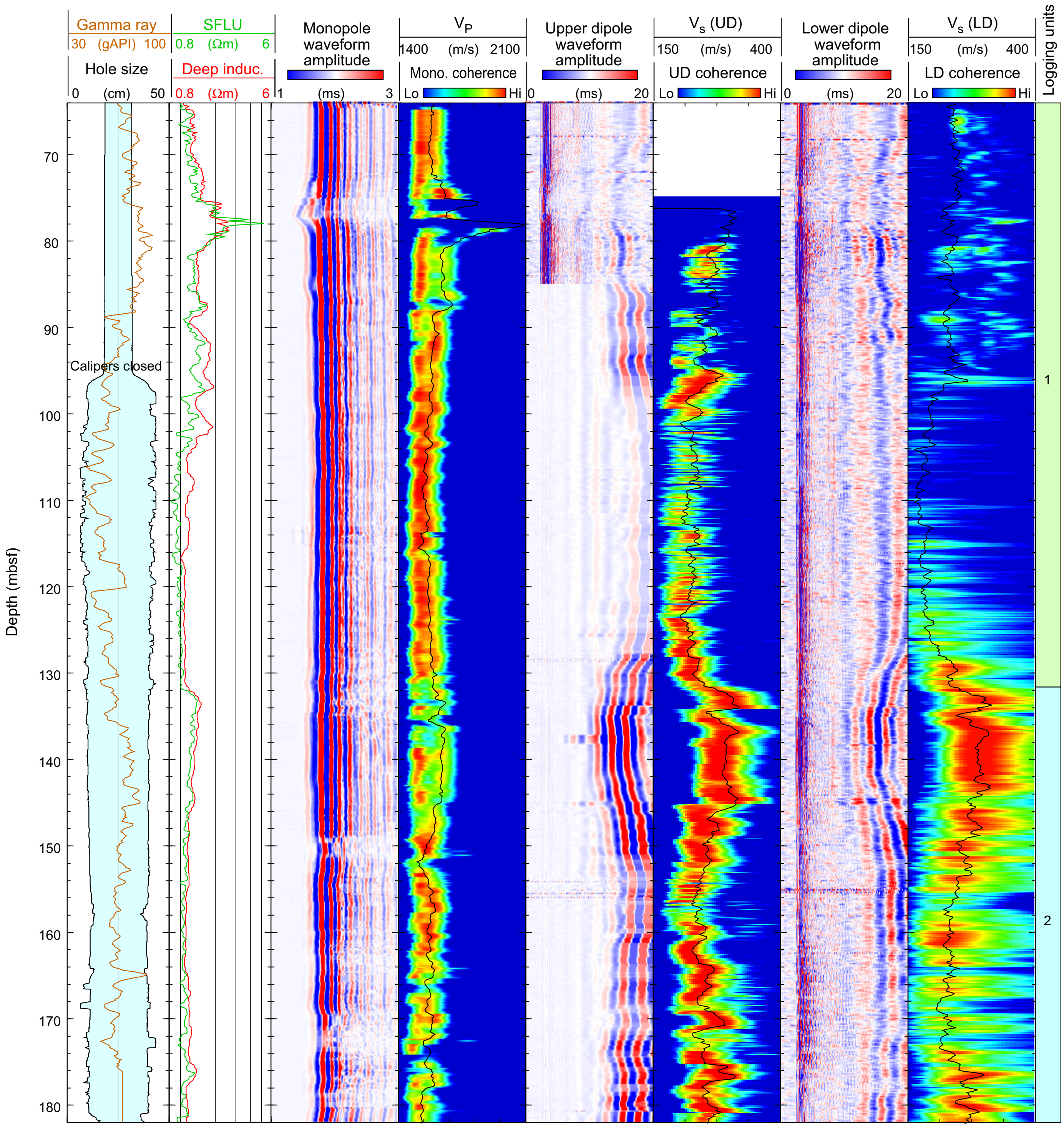

Figure 36. Sonic waveform amplitude and coherence data, and velocity logs measured by the DSI in Hole NGHP-01-15A. The hole size, calculated from the FMS calipers, and the gamma ray and resistivity logs are shown for quality control and correlation. [FMS, formation micro scanner; V_P, P-wave velocity; V_s, S-wave velocity; LD, Lower dipole; UD, Upper dipole]

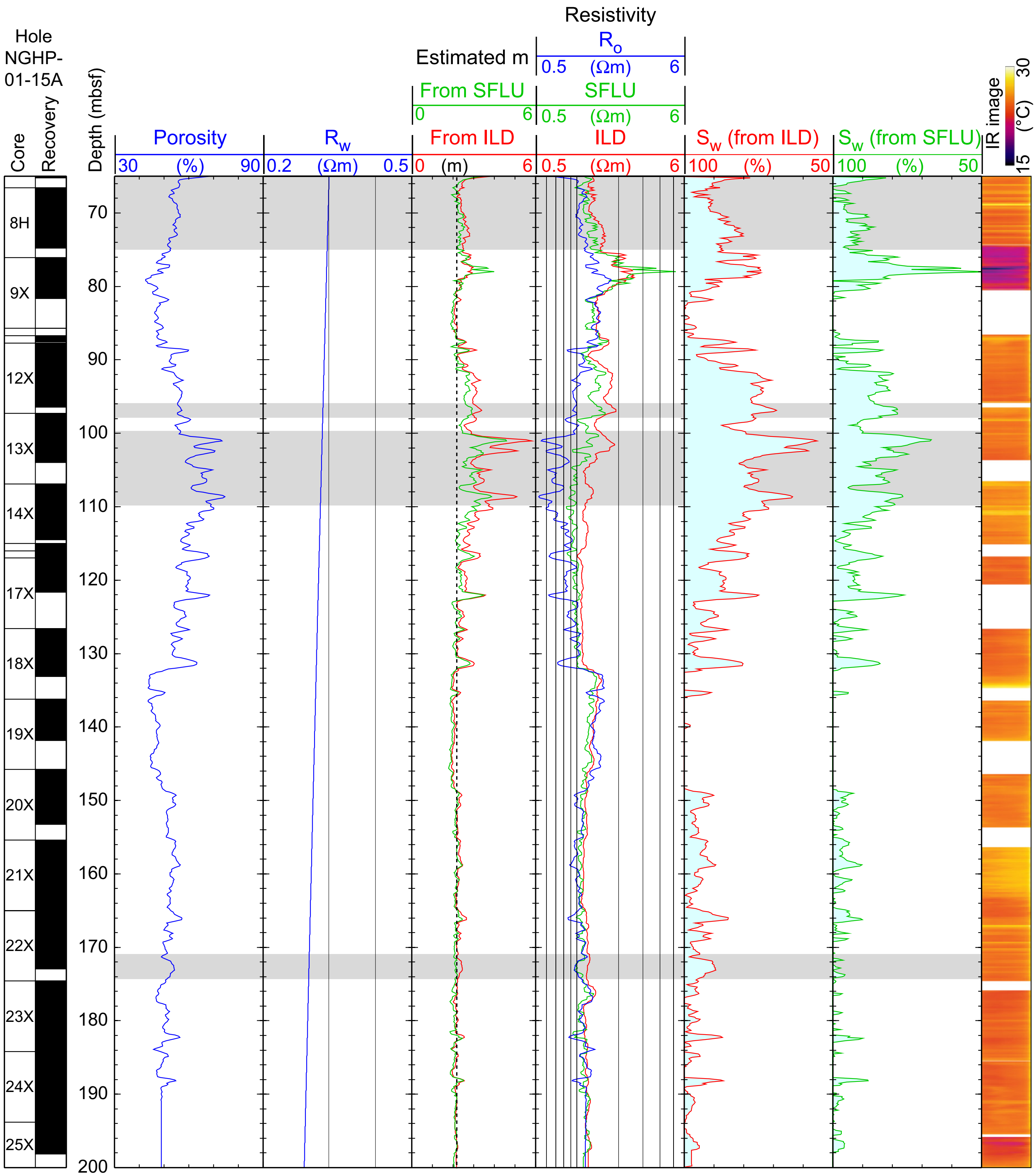

Figure 37. Water saturations from Archie's equation and wireline porosity and resistivity logs in Hole NGHP-01-15A. The gray area indicates degraded data quality. A summary of the infrared (IR) images recorded on the cores recovered from Hole NGHP-01-15A shows the intervals where cold anomalies identify the presence of gas hydrate. The areas in grey indicate intervals with unreliable density and porosity measurements due to bad hole conditions or closed caliper and where saturation values are likely overestimated. [R_w, Formation water resistivity; R_0, Computed formation resistivity for 100 percent water saturation; R_t, Measured resistivity; S_w, water saturation; SFLU, spherically focused unaveraged resistivity; ILD, deep induction resistivity log]

the baseline of this curve in the low-resistivity intervals where there is likely no gas hydrate below ~130 mbsf. Using the porosity log and Archie's equation ($R_0 = (a\ R_w)\ /f^n$), we derive the predicted resistivity of the water-saturated formation R_o. A qualitative influence of gas hydrate on the resistivity log is indicated by the difference between the R_0 and the measured resistivity R_t. The estimated water saturation, assumed to be the numerical complement of the hydrate saturation, is $S_w = (R_0/R_t)^{1/n}$, where n = 2 (Pearson and others, 1983). We used the density porosity and two resistivity measurements to derive the results shown in figure F37. The Spherically Focused unaveraged resistivity (SFLU) has the highest resolution, but the shallowest penetration, of the resistivity measurements made by the DIT tool and is more sensitive to drilling disturbances; the Deep Induction log (ILD) has the deepest penetration, but a lower vertical resolution. The combination of these two estimates provides a possible range of gas-hydrate distribution around Hole NGHP-01-15A.

The results indicate that gas hydrate could occupy as much as ~25 percent of the pore space in some intervals between ~90 and 110 mbsf, and locally almost 50 percent around 80 mbsf. Because of the irregular hole between 95 and 110 mbsf, the anomalously low density readings in this interval generate unreliably high porosity values, and the saturation values have to be considered with caution. The small accumulations below the bottom of the gas-hydrate stability zone, which if it coincides with the BSR is at ~130 mbsf should be free gas. Several intervals, underlined in grey in figure 37, had anomalously low density log values resulting in excessively high porosity and estimated gas-hydrate or free gas concentrations.

References Cited

Bjerrum, L., 1972, Embankments on soft ground: Proceedings of the ASCE Specialty Conference on Performance of Earth and Earth-Supported Structures, Purdue University, v. II, p. 1–54.

Davis, E.E., Hyndman, R.D., and Villinger, H., 1990, Rates of fluid expulsion across the northern Cascadia accretionary prism—Constraints from new heat flow and multichannel seismic reflection data: Journal of Geophysical Research, v. 95, p. 8869–8889.

Duan, Z., Møller, N., Greenberg, J., and Weare, J.H., 1992, The prediction of methane solubility in natural waters to high ionic strengths from 0° to 250 °C and from 0 to 1600 bar: Geochimica et Cosmochimica Acta, v. 56, p. 1451–1460.

Fofonoff, N.P., 1985, Physical properties of seawater: Journal of Geophysical Research, v. 90, no. C2, p. 3332–3342.

Holtz, R.D., and Kovacs, W.D., 1981, An introduction to geotechnical engineering: Englewood Cliffs, N.J., Prentice-Hall, Inc., 733 p.

Hunt, R.E., 1984, Geotechnical engineering investigation manual: New York, McGraw-Hill Book Company, 983 p.

Kvenvolden, K.A., and Lorenson, T.D., 2000, Methane and other hydrocarbon gases in sediment from the southeastern North American continental margin, *in* Paull, C.K., Matsumoto, R., Wallace, P.J., Black, N.R., Borowski,W.S.,Collett, T.S., Damuth, J.E., Dickens, G.R., Egeberg, P.K., Goodman,K., Hesse, R.F., Hiroki, Y., Holbrook, W.S., Hoskins, H., Ladd, J. ,Lodolo, E., Lorenson, T.D.,Musgrave, R.J., Naehr, T.H., Okada, H., Pierre, C., Ruppel, C.D., Satoh, M., Thiery, R., Watanabe, Y., Wehner, H., Winters, W.J.,and Wood, W.T., Gas hydrate sampling on the Blake ridge and Carolina rise; covering leg 164 of the cruises of the drilling vessel JOIDES Resolution, Halifax, Nova Scotia, to Miami, Florida, sites 991–997, 31 October–19 December 1995: Proceedings of the Ocean Drilling Program, Scientific Results, v. 164, p. 29–36.

Ladd, C.C., Foote, R., Ishihara, K., Schlosser, F., and Poulos, H.G., 1977, Stress-deformation and strength characteristics—State-of-the-art report: Proceedings of the Ninth International Conference on Soil Mechanics and Foundation Engineering, Tokyo, v. 2, p. 421–494.

Lambe, T. W. and Whitman, R.V., 1969, Soil mechanics: New York, John Wiley and Sons, 553 p.

Musgrave, R.J., Bangs, N.L., Larrasoana, J.C., Gracia, E., Hollamby, J., and Vega, M.E., 2006, Rise of the base of the gas hydrate zone since the last glacial recorded by rock magnetism: Geology, v. 34, no. 2, p. 117–120.

Novosel, I., Winters, W.J., Boldina, O.M., Labails, C., and Geli, L., 2007, Thermal conductivity of sediment recovered from the IMAGES VIII/PAGE 127 Gas Hydrate and Paleoclimate Cruise on the R/V Marion Dufresne in the Gulf of Mexico, 2–18 July 2002, *in* Winters, W.J., Lorenson, T.D., and Paull, C.K., eds., Initial report of the IMAGES VIII/PAGE 127 gas hydrate and paleoclimate cruise on the RV Marion Dufresne in the Gulf of Mexico, 2–18 July 2002: U.S. Geological Survey Open-File Report 2004–1358.

Pearson, C.F., Halleck, P.M., McGuire, P.L., Hermes, R., and Mathews, M., 1983, Natural gas hydrate deposits—A review of *in situ* properties: Journal of Physical Chemistry, v. 87 p. 4180–4185.

Sloan, E.D., 1998, Clathrate Hydrates of Natural Gases (2d ed.): New York (Marcel Dekker), 705 p.

Tréhu, A.M., Bohrmann, G., Rack, F.R., Torres, M.E., Delwiche, M.E., Dickens, G.R., Goldberg, D.S., Gracia, E., Guerin, G., Holland, M., Johnson, J.E., Lee, Y.J., Liu, C.S., Long, P.S., Milkov, A.V., Riedel, M., Schultheiss, P., Su, X., Teichert, B., Tomaru, H., Vanneste, M., Watanabe, M., and Weinberger, J.L.,, 2003, Proceedings of the Ocean Drilling Program, Initial Reports 204 [CD-ROM], 81 p.

Xu, W., 2002, Phase balance and dynamic equilibrium during formation and dissociation of methane gas hydrate: Proceedings of the 4th International Conference on Gas Hydrates, Yokohama, Japan, p. 195–200.

Xu, W., 2004, Modeling dynamic marine gas hydrate systems: American Mineralogist, v. 89 p. 1271–1279.